AN ABSTRACT OF THE DISSERTATION OF

Chang-Ho Choi for the degree of Doctor of Philosophy in Chemical Engineering presented on March 4, 2013.

Title: Synthesis of Colloidal Metal Oxide Nanocrystals and Nanostructured Surfaces Using a Continuous Flow Microreactor System and their Applications in Two-phase Boiling Heat Transfer

Abstract approved:

_____

Chih-hung Chang

Metal oxide nanocrystals have attracted significant interests due to their unique chemical, physical, and electrical properties which depend on their size and structure. In this study, a continuous flow microreactor system was employed to synthesize metal oxide nanocrystals in aqueous solution. Assembly of nanocrystals is considered one of the most promising approaches to design nano-, microstructures, and complex mesoscopic architectures. A variety of strategies to induce nanocrystal assembly have been reported, including directed assembly methods that apply external forces to fabricate assembled structures.

In this study ZnO nanocrystals were synthesized in an aqueous solution using a continuous flow microreactor. The growth mechanism and stability of ZnO nanocrystals were studied by varying the pH and flow conditions of the aqueous solution. It was found that convective fluid flow from Dean vortices in a winding microcapillary tube could be used for the assembly of ZnO nanocrystals. The ZnO

nanocrystal assemblies formed three-dimensional mesoporous structures of different shapes including a tactoid, a retangle and a sphere. The assembly results from a competing interaction between electrostatic forces caused by surface charge of nanocrystals and collision of nanocrystals associated with Dean vortices. The as synthesized colloidal ZnO nanocrystals or assembly were directly deposited onto a substrate to fabricate ZnO nanostructured surfaces. The rectangular assembly led to flower-like ZnO nanostructured films, while the spherical assembly resulted in amorphous ZnO thin film and vertical ZnO nanowire (NW) arrays. In contrast to the formation of flower structure or amorphous thin film, only colloidal ZnO nanocrystals were used as the building blocks for forming vertical ZnO NW arrays. This study demonstrates the versatility of the microreactor-assisted nanomaterial synthesis and deposition process for the production of nanostrucuturesres with various morphologies by tuning the physical parameters while using the same chemical precursors for the synthesis.

ZnO flower structure was coated on a microwick structure to improve the capillary flow. The coated microwick structure showed an enhanced capillary rise, which was attributed to the hydrophilic property and geometrical modification of ZnO nanostructure. Two-phase boiling heat transfer was performed using ZnO nanostructured surfaces. ZnO nanocoating altered the important characteristics including surface roughness and wettability. Hydrophilic nature of the ZnO nanocoating generally enhanced the boiling heat transfer performance, resulting in higher heat transfer coefficient (HTC), higher critical heat flux (CHF), and lower surface superheat comparing to the bare surface. Octahedral SnO and porous NiO

films, fabricated by a continuous flow microreactor system, were suggested as potential boiling surfaces for the high porosity and irregularity of their structures.

Synthesis of Colloidal Metal Oxide Nanocrystals and Nanostructured Surfaces Using a Continuous Flow Microreactor System and their Applications in Two-phase Boiling Heat Transfer

by
Chang-Ho Choi

A DISSERTATION

submitted to

Oregon State University

in partial fulfillment of
the requirement for the
degree of

Doctor of Philosophy

Presented March 4, 2013
Commencement June 2013

Doctor of Philosophy dissertation of Chang-Ho Choi presented on March 4, 2013

APPROVED:

Major Professor, representing Chemical Engineering

Head of the School of Chemical, Biological & Environmental Engineering

---

Dean of the Graduate School

I understand that my dissertation will become part of the permanent collection of Oregon State University libraries. My signature below authorizes release of my dissertation to any reader upon request.

Chang-Ho Choi, Author

ACKNOWLEDGEMENTS

First of all, I would like to praise the LORD who has given me enormous help to achieve such a great outcome. When I faced some problems in my research, the LORD has guided me in the right direction, and when I was in desperate situation, the LORD has drawn me out of the situation by offering me encouraged words and the promise. Beside my research achievement, I really appreciate the LORD who allows me to have everything around me including my wife and two kids. I cannot express all my thanks to the LORD with words and will keep praying to communicate with the Lord.

I would like to give special thanks to my advisor, Dr. Chih-hung Chang, for all his supports including financing and advices to develop my research. I have been motivated whenever I saw him going to the library carrying a big backpack. Sometimes I felt like he even study harder than me and more dedicated on my research, which made me embarrassed and awake from my laziness. I was also so impressive from him when he sincerely asked to pray for my project and my family. I have been so glad to have the advisor who has deep faith. In his faith, I believe the Lord bless him and his family.

I would like to thank my committee members, Dr. Brian K. Paul, Gregory S. Herman, Hailei Wang, and Frank Chaplen for their attention on scheduling my final oral exam. Especially Dr. Paul and Herman has served as the committee members since my master course. Through the program meeting and oral preliminary exam, they gave me helpful advices and directions that made my work more advanced.

I would like to thank to my former and current group members, Hyungdae Jin, Wei Wang, Yu-Wei Su, Seungyeol Han, Debra Gilbuena, Yong Li, Wei-Liang Yen, Mike Knapp, Peter Krider, Paul C. Ahrens, Paravee Vas-Umnuay, Kathy Han, Changquing Pan, Kijoong Kim, Yujuan He, and Zhong Wei. I have been happy to work with my group members and their support for my research. I would like to give special thank to Changquing for replacing nitrogen gas tank most of time. I also would like to give special thank to Yu-Wei Su to teach me TFT process, and thanks to his effort and time, I can achieve good TFT device performances.

I would like to thank to my Korean Presbyterian Church (KPC) members who have prayed for my family and shared sadness and happiness together. I would like to give special thanks to Young's Kitchen family members. They have provided our family the great support and love. I was so impressive from their kindness and love to harmonize Korean community in this city. I would like to give special thank to Shankar Krishnan (Intel), Don Higgins (PNNL), and Jair Lizarazo-Adarme (PNNL) for supporting my work and significant assistance on my research.

Lastly, I would like to give special thanks to my wife, Eunjoung Song, who has dedicated on my study and helped me focus on the study only. She is a great wife and great mother as well. I will try to pay her sacrifice and dedication back. My precious children, Sarah S. Choi and Jacob H. Choi, is the biggest present that the Lord gave me in my life. Seeing their smile and growth, I can relieve all of problems and stress. I wish that my family stays with the Lord and grows in the faith. I would like to thank to my parents and younger brother in Korea. Although we are now far from each other, they have always wished the bless for my family. I love them and pray for their salvation.

TABLE OF CONTENTS

Page

CHAPTER 1. Introduction..... 1

1.1. Synthesis of metal oxide nanocrystals in aqueous medium..... 1

1.1.1. Synthetic methodologies of metal oxide nanocrystals..... 2

1.1.2. Growth and dispersion behavior of metal oxide nanocrystals..... 6

1.2. Two-phase boiling heat transfer..... 13

1.2.1. Pool boiling curve..... 14

1.2.2. Models of nucleate boiling heat transfer..... 16

1.2.3. Techniques of boiling surface treatment..... 19

1.3. References..... 23

CHAPTER 2. Growth and Assembly of ZnO Nanocrystals in a Continuous Flow Microreactor..... 27

2.1. Introduction..... 28

2.2. Experimetnal..... 29

2.2.1. Synthesis of ZnO nanocrystals in a continuous flow microreactor..... 29

2.2.2. ZnO nanocrystal characterization..... 31

2.3. Results and Discussion..... 31

2.3.1. pH effect on growth and stability of ZnO nanocrystals..... 31

2.3.2. Effect of external forces of convective flow on ZnO nanocrystal assembly..... 35

2.3.3. Dispersion behaviors of ZnO assembly in some solvents..... 46

2.4. Conclusons..... 48

2.5. References..... 48

TABLE OF CONTENTS (Continued)

Page

CHAPTER 3. Controlled Solution Synthesis of ZnO Nanostructured Surfaces Using a Continuous Flow Microreactor..... 53

3.1. Introduction..... 53

3.2. Experimental..... 55

3.2.1. Fabrication of ZnO nanostructured surfaces..... 55

3.2.2. Characterization of ZnO nanocrystals and nanostructured surfaces..... 57

3.3. Results and Discussion..... 57

3.3.1. Formation of ZnO assembly in a continuous flow microreactor..... 57

3.3.2. Effects of solution flow rates on morphology of ZnO nanostructured surfaces..... 62

3.3.3. Growth study of ZnO flower structure..... 67

3.4. Conclusions..... 75

3.5. References..... 76

CHAPTER 4. Controlled Growth of Vertical ZnO Nanowire Arrays Using a Continuous Flow Microreactor.....78

4.1. Introduction..... 79

4.2. Experimental..... 80

4.2.1. Fabrication of ZnO seed layer and NW arrays..... 80

4.2.2. Characterization of colloidal ZnO nanocrystals, seed layer, and NW arrays..... 82

4.3. Results and Discussion..... 83

4.4. Conclusions..... 90

4.5. References..... 91

CHAPTER 5. Capillary Rise of Nanostructured Microwicks..... 93

TABLE OF CONTENTS (Continued)

Page

5.1. Introduction..... 93

5.2. Experiemtnal..... 96

5.2.1. Deposition of flower ZnO nanostructure on the microwick structure.. 96

5.2.2. Capillary rise measurement-height measurement & mass gain approach..... 99

5.3. Results and Discussion..... 100

5.3.1. Synthesis of flower ZnO nanostructure in a continuous flow microreactor..... 100

5.3.2. Capillary rise of the coated wick structure..... 101

5.4. Conclusions..... 109

5.5. References..... 110

CHAPTER 6. Two-phase Boiling Heat Exchanger Using Metal Oxide Nanostructured Surfaces..... 113

6.1. Introduction..... 114

6.2. Experimental..... 116

6.2.1. Preparation of nanostructured boiling surfaces..... 116

6.2.2. Pool boiling facility..... 117

6.2.3. Characterization of boiling surfaces..... 119

6.3. Results and Discussions..... 120

6.3.1. Characteristic results of boiling surfaces..... 120

6.3.2. Boiling heat transfer performance..... 124

6.3.3. Promising nanostructured boiling surfaces..... 133

6.4. Conclusions..... 136

TABLE OF CONTENTS (Continued)

Page

6.5. References..... 137

CHAPTER 7 Conclusions and Future Directions..... 139

7.1. Conclusions..... 139

7.2. Future Directions..... 140

7.2.1. Continuous flow microreactor system..... 140

7.2.2. Two-phase boiling heat exchanger..... 141

LIST OF FIGURES

Figures Page

Figure 1.1. Mechanism of metal oxide formation via microemulsion technique..... 5

Figure 1.2. Speciation diagram of zinc precursors with respect to solution pH..... 7

Figure 1.3. Scheme of DLVO theory for ZnO nanocrystals formed (a) near PZC and (b) far from PZC..... 11

Figure 1.4. Scheme of temporal concentration change during nucleation and growth of nanocrystals..... 12

Figure 1.5. Typical pool boiling curve..... 16

Figure 2.1. Scheme of the continuous flow microreactor system..... 30

Figure 2.2. HRTEM images of ZnO nanocrystals formed at pH=13: (a) dispersed nanocrystals and (b) typical primary ZnO nanocrsytal with FFT image..... 33

Figure 2.3. X-ray diffraction patterns of ZnO nanocrystals prepared at pH=9.5... 34

Figure 2.4. Low resolution (a) and high resolution (b) TEM images of ZnO nanocrystals formed at pH=9.5 (inset shows the FFT analysis)..... 35

Figure 2.5. Temperature of the solution as a function of the length of tube and volumetric flow rates..... 36

Figure 2.6. Hydrodynamic study of the helical reactor: (a) helical reactor geometry and contour of the axial velocity component in the reactor at $\theta=\pi/2$, (b) velocity profile with respect to the Dean numbers in the reactor at $\theta=\pi/2$..... 38

Figure 2.7. HRTEM images of ZnO nanocrystals synthesized at Dean number=36: (a) low magnification and (b) aggregated ZnO nanocrystal..... 39

Figure 2.8. TEM image of three-dimensional mesoporous tactoids formed by ZnO nanocrystals and corresponding EDX spectrum..... 40

Figure 2.9. HRTEM images of ZnO nanocrystal assembly formed at Dean number=78: (a) a single tactoid, (b) edge area of the structure, and (c) central area of the structure with a FFT image..... 42

Figure 2.10. HRTEM images of ZnO nanocrystals aggregated at Dean number=150..... 44

Figure 2.11. Schematic diagram of the ZnO nanocrystal assemblies..... 45

LIST OF FIGURES (Continued)

Figure Page

Figure 2.12. UV-visible spectroscopy of the ZnO assembly coated on glass..... 46

Figure 2.13. Morphologies of ZnO nanoparticles precipitated from (a) no assembly, (b) tactoid structure, and (c) spherical structure..... 47

Figure 3.1. Scheme of the continuous flow microreactor system for the synthesis and deposition of ZnO nanostructured surfaces..... 56

Figure 3.2. Speciation diagram of Zn precursors with respect to solution pH..... 58

Figure 3.3. Assembly of colloidal ZnO nanocrystals synthesized at flow rate (a) 14. mL/min and (b) 28.1 mL/min..... 60

Figure 3.4. Flower ZnO nanostructured surface prepared in 14.7 mL/min flow rate..... 63

Figure 3.5. XRD data of ZnO flower structure..... 64

Figure 3.6. Amorphous ZnO thin film prepared in 28.1 mL/min flow rate: (a) SEM image with AFM (inset) and (b) HRTEM image with FFT (inset)..... 65

Figure 3.7. Optical band gap of the amorphous ZnO thin film..... 65

Figure 3.8. ZnO flower structure grown by the batch process..... 67

Figure 3.9. SEM images of the flower structure prepared at various deposition temperature: (a) 50 ℃, (b) 100 ℃, (c) 150 ℃, (d) 200 ℃, and (e) 250 ℃ (scale bar = 1μm)..... 69

Figure 3.10. XRD data of the flower structures prepared at various process conditions: (a), (b), (c), and (d) corresponding to the sample no. 4, 5, 10, and 13 respectively..... 70

Figure 3.11. Low magnification SEM images of the flower structure grown at various deposition temperature: (a) 50 ℃, (b) 100 ℃, (c) 150 ℃, (d) 200 ℃, and (e) 250 ℃ (scale bar = 50 μm)..... 71

Figure 3.12. HRTEM and FFT image (inset) of a typical flower structure..... 71

Figure 3.13. SEM images of flower structure grown in (a) 500 rpm, (b) 1000 rpm, (c) 1500 rpm, (d) 2000 rpm, and (e) 0 rpm..... 73

Figure 3.14. Low resolution SEM images of the flower structure grown in (a) 500 rpm, (b) 1000 rpm, (c) 1500 rpm, (d) 2000 rpm, and (e) 0 rpm..... 74

LIST OF FIGURES (Continued)

Figure Page

Figure 3.15. SEM images of the flower structure: (a), (b), and (c) corresponding to sample no. 11, 12, and 13 respectively (scale bar = 1 μm)..... 75

Figure 4.1. Scheme of the continuous flow microreactor system for the growth of vertical ZnO NW arrays..... 82

Figure 4.2. HRTEM images of colloiodal ZnO nanocrystals synthesized at solution flow rate of 6.8 mL/min: (a) low magnification and (b) a typical colloidal ZnO nanocrystal..... 85

Figure 4.3. HRTEM images of the seed layer and ZnO NW: (a) interface between the seed layer and polycrystal ZnO layer, (b) amorphous ZnO seed layer, (c) polycrystal ZnO layer, and (d) ZnO NW..... 87

Figure 4.4. Characterization of vertical ZnO NW arrays: (a) top-down view of SEM image and (b) corresponding XRD data (*substrate)..... 87

Figure 4.5. SEM images of ZnO NW arrays prepared in various growth conditions..... 89

Figure 4.6. Cross sectional views of ZnO NW arrays grown in various deposition period : (a) 1 min., (b) 5 min., (c) 10 min., and (d) 20 min..... 90

Figure 4.7. Estimated growth rate of ZnO NW arrays..... 91

Figure 5.1. Scheme of dual-mode microwick structure..... 96

Figure 5.2. Scheme of the continuous flow microreactor system with flow cell... 99

Figure 5.3. SEM images of flower ZnO nanostructure and photograph of the coated wick structure..... 102

Figure 5.4. Comparison of experimental wicking results with analytical models..... 103

Figure 5.5. Mass gain approach of the coated wick structure in EtOH; (1) wetting regime, (2) wicking regime, (3) de-wetting regime, and (4) evaporation regime..... 106

Figure 5.6. Capillary rise by mass gain approach: (a) comparison of all tested single-mode wick structure, (b) capillary rate at initial wicking, (b) closer look of step-rise wicking rise..... 109

LIST OF FIGURES (Continued)

Figure Page

Figure 6.1. Pool boiling facility: (a) photograph of the boiling facility and (b) illustration of the instrumented test heater assembly..... 120

Figure 6.2. Characterization of bare stainless steel substrate: (a) SEM image, (b) contact angle measurement, and (c) average surface roughness..... 121

Figure 6.3. Characterization of the flower structure: (a) SEM image, (b) average surface roughness, and (c) XRD pattern (* presents stainless steel substrate)..... 123

Figure 6.4. Characterization of the pyramidal structure: (a) SEM image, (b) average surface roughness, (c) contact angle measurement, and (d) XRD pattern (* presents stainless steel substrate)..... 124

Figure 6.5. Characterization of irregular NRs structure: (a) SEM image and (b) XRD pattern (* presents stainless steel substrate)..... 125

Figure 6.6. Characterization of aligned NRs structure (low aspect ratio): (a) SEM image, (b) cross-sectional image, (c) contact angle measurement, and (d) XRD pattern (* presents stainless steel substrate)..... 126

Figure 6.7. Comparisons of the experimental boiling results with empirical correlations..... 127

Figure 6.8. Pool boiling performances of the nanostructured boiling surfaces: (a) boiling curves and (b) HTC..... 128

Figure 6.9. Onset of bubble nucleation..... 129

Figure 6.10. Wettability state of liquid drop: (a) Wenzel's state and (b) Cassie-Baxter state..... 131

Figure 6.11. Bubble growing on hydrophilic surface..... 132

Figure 6.12. Bubble growing on hydrophobic surface..... 133

Figure 6.13. SEM image of the flower structure after boiling performance..... 134

Figure 6.14. Speciation diagram of Sn precursors as a function of solution pH.. 136

Figure 6.15. SEM image of SnO nanostructured surface..... 137

Figure 6.16. SEM image of porous NiO film..... 138

LIST OF FIGURES (Continued)

Figure Page

Figure 7.1. Scheme of the proposed optimal boiling surface: (a) side view and (b) plain view..... 145

LIST OF TABLES

Table Page

Table 1.1. PZC values of various metal oxides..... 9

Table 1.2. Values of C_{sf} in the Rohsenow model for different fluid-surface combinations..... 17

Table 1.3. Summary of boilig heat transfer performances using nanostructured boiling surfaces..... 22

Table 3.1. Summary of procee conditions for the flower structure..... 68

Table 5.1. Geometrical factors of the microwick structure..... 96

Table 5.2. Physical properties of EtOH used for the capillary rise study..... 107

Table 6.1. Summary of the system parameters for fabrication of nanostructured surfaces..... 117

Table 6.2. Summary of characterization of the boiling surfaces..... 123

NOMENCLATURE

Symbol	
q''	Heat flux
h_{lv}	Latent heat of vaporization per unit mass
g	Gravitational acceleration
Pr_l	Liquid Prandtl number
P_l	Liquid saturated pressure
T_w	Surface temperature
T_{sat}	Liquid saturated temperature
R	Pore radius
k	Permeability
h	Location of meniscus
t	Time
d	Film thickness
m_e	Mass flow due to evaporation
θ	Contact angle
σ	Interficial tension
μ	Dynamic viscosity
Φ	Porosity
Ω	Inclined angle

Chapter 1. Introduction

1.1. Synthesis of metal oxide nanocrystals in aqueous medium

Metal oxides have been widely studied in various areas of chemistry, physics and material science for their unique optical, electrical, and magnetic properties. For instance, SiO_2 is one of the most widely used materials due to its optical transparency, and its good electrical and thermal insulation properties [1]. Ferromagnetic iron oxides have been used for data storage and transmission. Ferroelectric or dielectric oxides of perovskite structure have found important applications in electronic devices [2]. Size of metal oxide crystals plays an important role in determining their properties, thus significant efforts have been devoted to size-controlled synthesis strategies [3, 4]. As size decreases towards nanometer scale, the ratio of surface to volume increases. This size effect leads to unique characteristics of metal oxide which is not present in corresponding bulk material. In addition, the chemical and physical properties of metal oxide are significantly affected by defects and unsaturated coordination sites on the surface.

A variety of synthetic methods have been developed. The synthetic approaches can be gruped into two major categories according to their growth phase. Gas-solid transformation techniques are used to form metal oxide nanocrystals including chemical vapor deposition (CVD) and physical vapor deposition (PVD). Advantage of this approach is its ability to obtain high purity nanocrystals. However, these processes normally operate in vacuum condition which requires higher facility cost and limits its accessibility for the large area

deposition [5]. Alternative to gas-solid transformation is solution-based process. The main advantage of the solution-based process over the gas-solid transformation technique is their versatility and lower-cost.

In this section, major solution-based synthetic technologies including precipitation method, sol-gel processing, microemulsion and solvothermal processing for the preparation of metal oxide nanocrystals will be introduced. Dispersion behavior of metal oxide nanocrsytals in solution plays an important role in controlling their size and shape. Stability of metal oxide nanocrystals in the solution, especially in the aqueous medium, will also be discussed in this section.

1.1.1. Synthetic methodologies of metal oxide nanocrystals

Precipitation method

One of the simplest methods for the preparation of metal oxide nanocrystals is precipitation. Metal oxide nanocrystals can be prepared by the combination of metal salt precursor, solvent, and reducing agent. Metal salt precursor is dissolved into water and forms aquo species. This aquo species turns into metal hydroxide through the hydrolysis reaction, and the reaction rate mainly depends on the pH value. Metal hydroxide is unstable, consequently experiences the condensation reaction, and form metal oxide nuclei after the removal of water molecule. Nuclei created by the condensation reaction experience further growth by a continuous supply of the precursors and reach a certain size that meet a thermodynamically stable condition. Interaction between nanocrystals determines dispersion behaviors of metal oxide nanocrystals, and a certain solution condition can cause the precipitation of nanocrystals. Due to the fast hydrolysis and condensation reaction

rate, it is difficult to control the particle size and to achieve monodispersed size distribution. However, control of electrostatic surface charge density of particles enables the possibility to tailor particle size and shape [6]. This process is very useful in terms of synthesizing composites of different metal oxide nanocrystals by the coprecipitation method. Precipitated metal oxide nanocrystals can be sintered at high temperature, which determines the crystalline phase of metal oxide. For example, zirconia (ZrO_2) exhibits the monoclinic phase at room temperature while transformed into tetragonal phase at 950 ℃ and cubic phase at 2200 ℃ [7].

Sol-gel process

The sol-gel process has also been used to prepare metal oxide nanocrystals [8, 9]. Principal of yielding nanocrystals is similar to the precipitation except for type of a precursor and solvent. Typically alkoxide metal precursors are dissolved in an alcohol. Selection of types of alcohols is important due to the alcohol interchange reaction [10]. The hydrolyzed metal precursor can bind with the organic compounds from alcoholic solvents, which interfere with the creation of metal oxide nanocrystals. Rates of the hydrolysis and condensation reactions determine the shape and size distribution of metal oxide nanocrystals. Depending on the process conditions, sols can be transformed to gels. Process of drying or a heat treatment also plays an important role in determining the properties of metal oxide nanocrystals, resulting in ultra fine powderd or bulk materials [11]. There are several advantages of the sol-gel process over conventional solution processes. Ultra fine metal oxide powders can be formed through the process because of

relatively easy control of the hydrolysis reaction. This process can be utilized for the scale-up production for industrial applications.

Microemulsion technique

A microemulsion technique creates isotropic micro or nano-reactor, referred to as the reaction vessel, formed by utilizing the hydrophilic and hydrophobic properties in water and oil phase respectively in the presence of a surfactant. The stably dispersed reaction vessel can be formed within a size range between 5 nm and 200 nm. Typically the solution consists of water phase, oil phase, and a surfactant having both polar heads and non-polar organic tails. When surfactants are dissolved in an oil-water mixture, they aggregate and form micelles which are stable thermodynamically and kinetically in the binary mixture. The micelles serve as micro or nano-reactors for the formation of metal oxide nanocrystals. Due to the homogeneous property of micelles, metal oxide nanocrystals synthesized in micelles exhibit uniform size distribution. Since the nucleation and growth of nanocrystals take place inside micelles, the rate of nucleation and growth are determined by collisions between micelles. A typical process to synthesize metal oxide nanocrystals using the microemulsion technique is described in Figure 1 [12]. Two separate microelemustions, containing metal salts in one emulsion and reducing agents in the other, are prepared. These two microemulsions are mixed together. During collisions between individual micelle, reactions such as reduction, nucleation, and growth occur. Growth of nanocrystals in micelles is limited by attachment of surfactant molecules on the nanocrystal surfaces, which depends on the thermodynamic condition. This technique is very useful in producing very

small particles with very good control over particle sizes while low production yield is being considered as the main disadvantage of this technique.

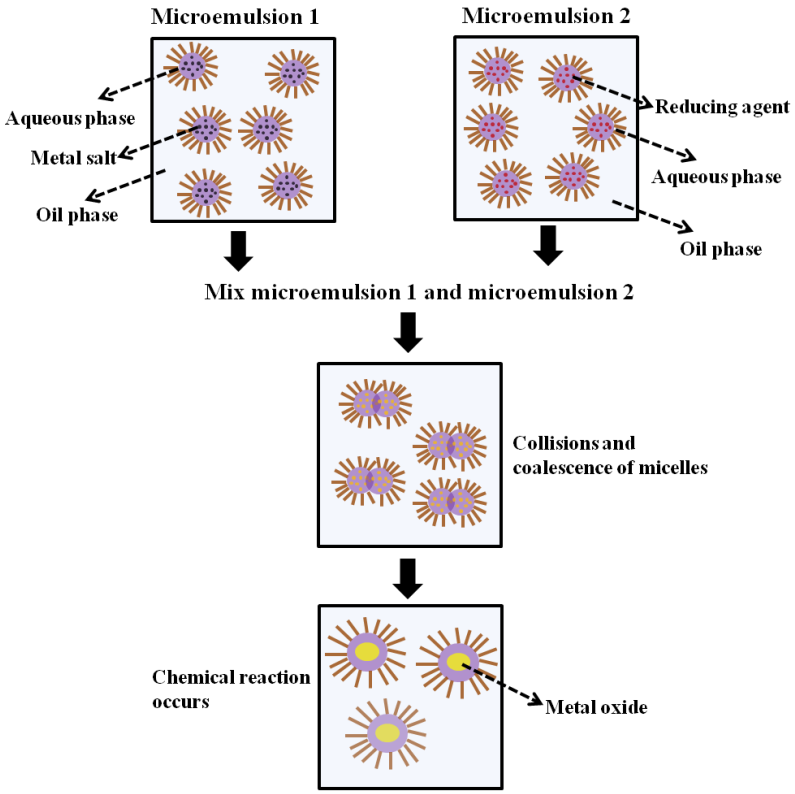

Figure 1.1. Mechanism of metal oxide formation via microemulsion technique.

Solvothermal technique

The solvothermal technique has been widely used to prepare metal oxide nanocrystals and semiconductor chalcogenides nanomaterials [13, 14]. Compared to the synthetic methods introduced above, high reaction temperature is required to decompose metal precursors and capping agents. Capping agents such as a long-chain amine and thiol are able to control the growth rate of metal oxide nanocrystals by adsorbing on nanocrystal surfaces, which prevents agglomeration between metal oxide nanocrystals. One of the widely used solvothermal techniques is hydrothermal synthesis. Typically an autoclave is used for the hydrothermal reaction. The advantage of the hydrothermal reaction is well described in the

literature [15]. Various metal oxide nancrystals with uniform size distribution and different morphologies have been prepared by the hydrothermal reaction.

1.1.2. Growth and dispersion behavior of metal oxide nanocrystals

Formation of metal oxide nuclei and subsequent growth of the nuclei in an aqueous medium depend on continuous hydrolysis and condensation reaction.. ZnO nanocrystal is used an an exemple for the discussion of metal oxide nanocrystal growth and dispersion behavior in an aqueous medium. In an aqueous medium, the pH value of solution plays a very important role in controlling the hydrolysis ratio of zinc precursors. The speciation diagram of zinc precursors is shown in Figure 2. The hydrolysis ratio increased with the increment of the pH value yielding zinc-aquo-hyroxo ions $[Zn(OH_2)_{4-n}(OH)_n]^{2-n}$. These zinc-aquo-hydroxo ions are the precursors for the initiation step of the nucleation of ZnO nanocrystals.

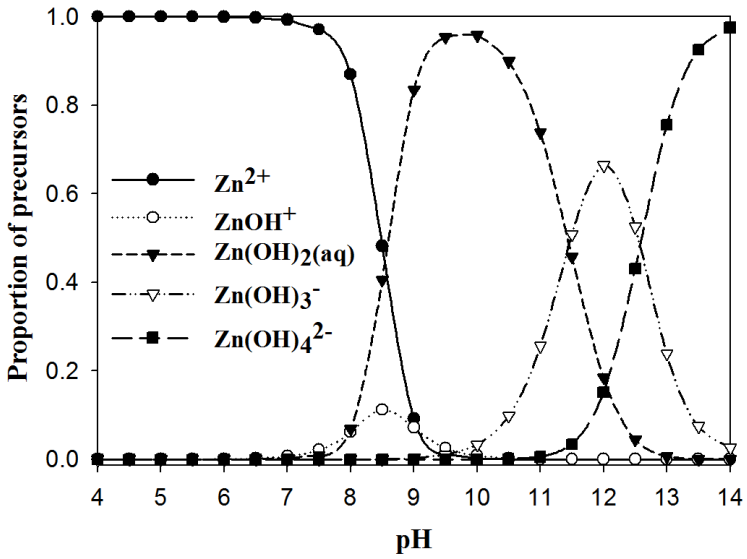

Figure 1.2. Speciation diagram of zinc precursors plots as a function of solution pH value.

Once sufficient amounts of the precursors are present in the aqueous medium, the condensation reaction begins to generate the ZnO nuclei. In the condensation reaction, hydroxide ligands bearing a negative partial charge were attracted by the Zn^{2+} cation bearing a positive charge. As a result of a covalent bond between Zn^{2+} cation and hydroxide ligand, a new complex ion that has an excessive coordination number is created. The complete coordination number is subsequently made by releasing H_2O from the newly formed complex ion along with hydrogen transfer. It was reported that partial charge of the metal cation and hydroxide ion should meet the criterion for the condensation reaction, $\delta(OH) < 0$ and $\delta(M) > +0.3$. The condensation reaction will be terminated if the hydroxide ligand of the precursor loses its nucleophilic property in the case of polycation ($\delta(OH) > 0$), or if in the case of polyanion a positive charge of the metal decrease ($\delta(M) < +0.3$). The precursors are bridged by OH ligands during the condensation reaction and initially form $Zn(OH)_2$ which may be unstable and spontaneously dehydrated by internal oxolation to create the hydrated oxide, $ZnO{\cdot}H_2O$. The brief description of the process from the initiation of condensation to formation of ZnO is shown as following:

$$O_2H\text{-}\underset{|}{Zn}\text{-}OH + O_2H\text{-}\underset{|}{Zn}\text{-}OH \xrightarrow{\text{Condensation}} O_2H\text{-}\underset{|}{Zn}\text{-}OH\text{-}\underset{|}{Zn}\text{-}OH$$

$$\xrightarrow{\text{H trasnferred}} O_2H\text{-}\underset{|}{Zn}\text{-}O\text{-}\underset{|}{Zn}\text{-}\overset{H}{\underset{|}{O}}H \xrightarrow{\text{Dehydration}} O_2H\text{-}\underset{|}{Zn}\text{-}O\text{-}\underset{|}{Zn}\text{-}$$

Another important aspect of pH value of solution on the nanocrystal formation is that it plays a critical role in determining the stability of the nanocrystal dispersion, which is significantly decisive on controlling the

aggregation of ZnO primary nanocrystals in the aqueous medium. The stability of ZnO nanocrystal dispersions is strongly related to the electrostatic interaction between nanocrystals. In order to keep ZnO nanocrystals dispersed homogeneously as the sol state, nanocrystals should repel each other preventing them from aggregation caused by the Van der Waals force. Based on the nucleation and growth mechanism of the ZnO nanocrystals evolved by the condensation reaction, surface of ZnO nanocrystals end with OH ligands. The existence of OH ligands occupying the coordination site at the crystal interface was proven by Raman spectroscopy of metal oxide. As the nanocrystals possessing OH ligands at the interface are presented in the aqueous medium, the surface charge of the nanocrystals is significantly affected by the pH value of solution. Point of zero charge (PZC) is an important parameter of the surface in that it defines the pH of the solution for which the surface charge of the particle becomes zero. The surface charge on the metal oxide is the result of acid-base equilibrium. If the pH is below the PZC of the nanocrystals, the surface carries a positive charge while for pH > PZC it bears a negative charge as shown below.

$$M\text{-}OH_2^{+} + OH^{-} \xleftrightarrow{pH < PZC} M\text{-}OH + H_2O \xleftrightarrow{pH > PZC} M\text{-}O^{-} + H_3O^{+}$$

Magnitude of the repulsion force between the nanocrystals depends on the surface charge and ionic strength of the solution. As the surface charge is large and ionic strength is low, the repulsion force is very strong and prevents permanent contact between nanocrystals. However, on the other hand, for low surface charge and high ionic strength the attractive force overwhelms the repulsive force and eventually

leads to the nanocrystal aggregation. PZC of ZnO measured by the potentiometric process was reported to range from pH 9 to 10. PZC values of other metal oxide nanocrystals in the aqueous media are presented in Table 1 [16].

Table 1. PZC values of various metal oxides

z	Oxide	PCN
2	MgO	12.5
	ZnO	9~10
3	α-Fe2O3	5.5~9
	α-Al2O3	6.5~10
4	TiO2	3.5~6.5
	SiO2	2~4
5	Sb2O5	0.5
6	WO3	0.4

Z: oxidation number of metal

For ZnO nanocrystals formed near the PZC value, the surface charge of ZnO nanocrystals is very small, which causes rapid aggregation and flocculation. When it comes to the ZnO nanocrystals formed in pH far from the PZC value, the double layer theory is adopted to explain the nanocrystal stability in the aqueous medium. When ZnO nanocrystals stay in the solution far from the PZC value, role of electrolyte becomes important since nanocrystals carry a large surface charge. According to the double layer theory, the surface potential associated with the surface charge is offset by the counterions (electrolytes) and water which are strongly bound on the surface by chemisorption or physisorption within the Stern layer. Beyond the Stern layer, a diffuse double layer exists and the counterions diffuse freely within this layer. As nanocrystals move in anaqueous medium, they also carry the counterions existing within the double layer. Since ZnO nanocrystals existing in the same media carry the same counterions within the double layer,

when they come close they will repel one another and sustain their dispersion stability. The schematic illustration of this characteristic is presented below.

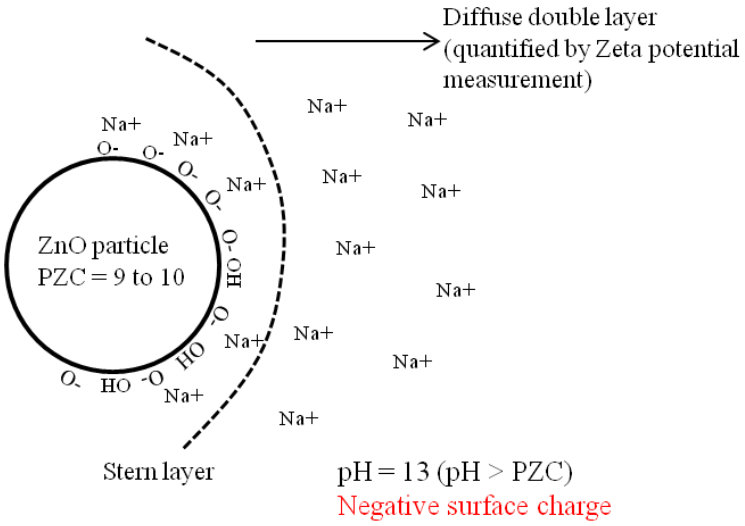

In addition to the surface charge, the concentration of counterions is very important in terms of determining the magnitude of repulsive force because the repulsive force is a function of the concentration of the counterions. It has been shown that the repulsive force increases with the addition of a small amount of counterions, however with large amounts of counterions the double layer will collapse and eliminate the repulsion force. Therefore, with the excess amount of the counterions, nanocrystals tend to aggregate or flocculate. The stability of dispersed nanocrystals and their tendency toward the aggregation is best described by the Derjaguin and Landau, Verwey and Overbeek (DLVO) theory [17]. The theory provides a tool that could be used to calculate the energy barrier needed to achieve the kinetic stability of the nanocrystal dispersion. The qualitative interaction energy of the ZnO nanocrystals calculated by the DLVO theory is shown in Figure 3. The energy barrier corresponding to state (b) indicates a kinetically unstable

state in which aggregation takes place. This energy state represents the ZnO nanocrystals synthesized near the PZC value. In state (a), the nanocrystals repel from one another maintaining an equilibrium distance between nanocrystals without flocculation, which represents the dispersion behavior of the ZnO nanocrystals prepared in a solution with its pH value far from the PZC value.

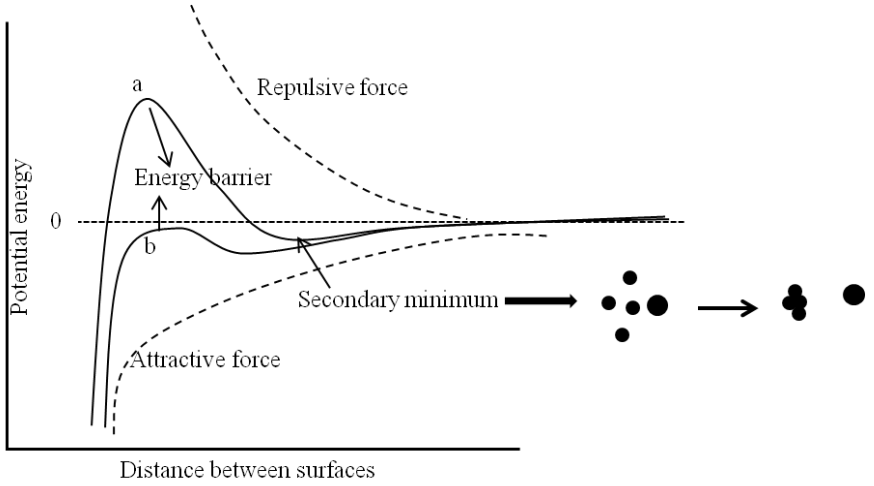

Figure 1.3. Scheme of DLVO theory for ZnO nanocrystals formed (a) near PZC and (b) far from PZC.

Nucleation of the ZnO nanocrystal is attributed to the condensation reaction of the precursors as described above. Growth of the nuclei is through the addition of the precursor on the existing ZnO nuclei and will be continued until the primary ZnO nanocrystals are generated. Uniform size distribution of ZnO nanocrystals is important in that size determines chemical and physical properties of nanocrystals. The conventional mechanism was suggested to explain the formation of monodispersed particles while synthesizing sulfur sols by the decomposition of sodium thiosulfate in acidic solution (Figure 1.4) [18].

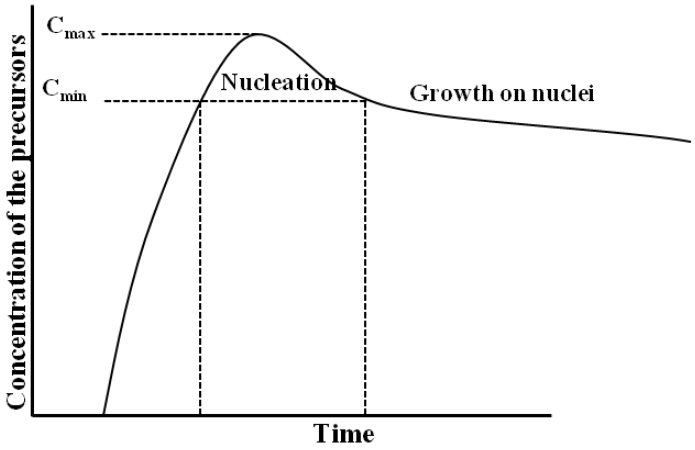

Figure 1.4. Scheme of temporal concentration change during nucleation and growth of nanocrystals.

When the concentration of the precursors is below C_{min}, the condensation reaction does not occur since the reaction rate is a function of the concentration of the precursors. However, once the sufficient precursors are present beyond C_{min}, the condensation rate dramatically increases and ZnO nuclei are explosively created throughout the solution. The formation of ZnO nuclei is diminished as the precursor concentration drops to C_{min} again. This phenomenon is generally observed because the rate of the precursor generation is significantly slower than that of the condensation reaction. In this condition, the phase of ZnO nucleation could be separated from the growth phase, and one burst of ZnO nucleation takes place. In other words, as the precursor concentration stays close to C_{min}, the precursors participate in growing on existing ZnO nuclei by the condensation reaction rather than being consumed to create new ZnO nuclei. Therefore, maintaining the precursor concentration close to C_{min} plays a significant role in obtaining monodispersed ZnO primary nanocrystals. The control of the precursor concentration is closely related to the control of the hydrolysis ratio of the Zinc

complex. Majtijevic also demonstrated that controlling the hydroxylation of metal is a critical point to obtain monodispersed metal oxides in his review [19].

1.2. Two-phase boiling heat transfer

Electronic system energy management and cooling for future advanced lasers, radars, and power electronics are gaining importance, resulting in a search for technologies and design techniques to dissipate ultra-high heat fluxes. There are two major types of cooling approaches including passive and active technique. The active technique involves external power equipment such as fans and evaporative air conditioner to accelerate the heat removal. Disadvantages of the active techniques include their complicated design and the space limit for the cooling facility. On the other hand, passive methods that do not require any external power input have been intensively researched in the past decades. The passive methods are compact and cost efficient. Among the various passive methods, two-phase cooling systems have been considered as one of the most promising approaches to dissipate large amount of heat flux because enormous amounts of heat can be transferred through the phase transition from liquid to vapor. Pool boiling has drawn significant interest due to its convenience and inexpensive experimental facility to implement. In this section, a typical pool boiling curve used to evaluate boiling performance will be introduced with an emphasis on the nucleate boiling regime. Associated with the latent heat of vaporization, the number of bubble nucleation sites plays a significant role in advancing heat transfer performance. Techniques of boiling surface treatment have been developed to increase the number of bubble nucleation sites. Especially

surface treatment adopting nanotechnology will be reviewed. Various empirical models have been proposed to predict boiling performance. Some models commonly applied for the prediction of boiling performance will also be presented.

1.2.1. Pool boiling curve

Pool boiling typically entails a surface submerged in an extensive pool under the stagnant condition with heat transfer driven by buoyancy force. The first systematic characteristic of boiling behavior was carried out when Nukiyama explored the boiling phenomena on a horizontal nichrome wire, demonstrating the different regimes of pool boiling performance using boiling curve [20]. A plot of heat flux versus wall superheat under a certain circumstance is shown in Figure 1.5. In an ambient condition, the liquid in the pool is saturated. If the surface temperature of the immersed body is controlled and slowly increased, a typical boiling curve can be obtained as displayed in Figure 5. At very low superheat levels, no bubble nucleation is created and heat is transferred from the surface to the liquid by natural convection. If the superheat is high enough to initiate bubble nucleation, a few bubbles could be formed at some cavities on the surface, which is called onset of nucleate boiling. In the isolated bubble regime, a few individual bubbles are created and depart from cavities on the surface. As more heat is supplied to the boiling surface, more cavities become active, and more bubble can be nucleated with high frequency. Once the spacing between isolated bubbles is so close and there is a rapid increase of bubble frequency, bubbles from adjacent cavities merge together and eventually form vapor slugs or vapor columns. With increasing surface superheat in the region of vapor slugs and columns, vapor

accumulates near the surface at some sites interfering with the inflow of the liquid into the surface, which eventually leads to dry out on some parts of the surface. Due to the fact that heat transfer coefficient in the vapor is significantly lower than the one in the liquid, the overall heat flux from the surface to liquid decrease. The reduction of heat flux results in a peak within the pool boiling heat-flux curve. . This peak is referred to as critical heat flux (CHF). If the superheat is increased beyond the critical heat flux condition, overall heat flux continues to be reduced. This regime is referred to as the transition boiling regime. In this regime, dry portions on the surface are unstable, showing significant fluctuation which results from the irregularity of surface rewetting. If the transition boiling is continued with increasing superheat, the regime could reach to the point referred to as the film boiling regime. Stable vapor film is formed in this regime and acts like an insulation blanket. Within the film boiling regime, the heat flux monotonically increases with the increase of superheat. This is due to the increasing conduction and convection heat transfer as the temperature gradient between the surface and the vapor film increases.

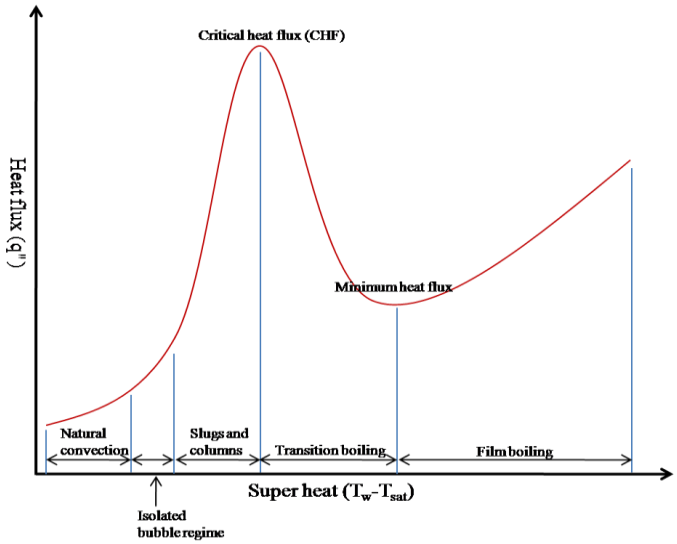

Figure 1.5. Typical pool boiling curve

1.2.2. Models of nucleation boiling heat transfer

Major characteristics of pool boiling curve are evaluated from CHF value and superheat. Therefore, various correlations to predict CHF value and analyze nucleate boiling regime have been proposed. The prediction of CHF is extremely difficult due to its challenge of evaluating accurate important parameters such as bubble departure diameter and bubble frequency. Some critical correlations for nucleate boiling regime and CHF prediction are introduced in this section.

Rohsenow's model

Rohsenow's model was proposed by Rohesnow in 1952 who assumed that single phase heat transfer correlation can be used to predict phase change heat transfer [21]. This reasoning is on the basis that the process of bubble nucleation is mainly attributed to the liquid agitation induced by bubble growth and bubble departure. The formulation of the model is

$$\frac{q''}{\mu_l h_{lv}}\left[\frac{\sigma}{g(\rho_l-\rho_v)}\right]^{1/2}=\left(\frac{1}{C_{sf}}\right)^{1/r}\mathrm{Pr}_l^{-s/r}\left[\frac{c_{pl}[T_w-T_{sat}(P_l)]}{h_{lv}}\right]^{1/r}$$

where value of r and s are recommended to 0.33 and 1.7 respectively. The value of s can be replaced to 1.0 when water is used as boiling fluid. Value of C_{sf} was tabulated empirically and dependent upon boiling fluid-boiling surface combination. The recommended Csf values are listed in Table 2 [22].

Table 2. Values of C_{sf} in the Rohsenow model for different fluid-surface combinations

Boiling fluid-surface combination	Csf
Water on Teflon pitted stainless steel	0.0058
Water on scored copper	0.0068
Water on ground and polished stainless steel	0.008
Water on emery polished copper	0.0128
Water on chemically etched stainless steel	0.0133
Water on mechanically polished stainless steel	0.0132
Water on emery polished, paraffin-treated copper	0.0147
Water on nickel (vertical tube)	0.006
Water on stainless steel (horizontal tube)	0.015
Water on copper (vertical tube)	0.013
n-Pentane on lapped copper	0.0049
n-Pentane on emery polished nickel	0.0127
n-Pentane on emery polished copper	0.0154
Carbon tetrachloride on emery polished copper	0.007
Carbon tetrachloride on copper	0.013
n-Butyl alcohol on copper (vertical tube)	0.003

Stephan and Abdelsalam model

This model was proposed based on dimensional analysis and optimal fits to empirical data [23]. Like the Rohsenow's model, different correlation with respect to fluid type was recommended. The model for water is

$$q^{"} = \{C_1[T_w - T_{sat}(P_l)]\}^{3.058}$$

Where value of C_1 depends on the system pressure.

Borishansky model

This correlation was proposed based on thermodynamic similitude [24]. The formulation of the correlation is

$$q^{"} = A^{3.33}[T_w - T_{sat}(P_l)]^{3.33}[F(P_r)]^{3.33}$$

$$A = 0.1011P_c^{0.69}$$

$$F(P)_r = 1.8P_r^{0.17} + 4P_r^{1.2} + 10P_r^{10}$$

$$P_r = P_l/P_c$$

Zuber's maximum heat flux correlation

With high heat flux bubbles created at the boiling surface merge together and form vapor columns. This correlation is based on the Helmholtz instability in which the vapor column departing from the boiling surface blocks fluid flow toward heated boiling surface [25]. This vapor column continuously interferes with the fluid refreshment on heated boiling surface, which leads to formation of a vapor blanket. In this condition, CHF takes place due to the extremely low heat transfer coefficient of the vapor blanket. The formulation of the correlation is

$$q''_{max,z} = 0.149\,\rho_v h_{lv}\left[\frac{\sigma(\rho_l-\rho_v)g}{\rho_v^2}\right]^{1/4}$$

The Zuber's original model was modified by Lienhard and Dhir who proposed replacement with values from 0.149 to 0.131 [26].

Kandlikar's maximum heat flux correlation

Kandlikar argued that the conventional CHF correlations based on hydrodynamic wave instability and considered the surface wettability and surface inclination. The correlation is related to the force balance between hydrodynamic pressure, surface tension and momentum force [27]. The hydrodynamic pressure and surface tension resist bubble spread in the lateral direction while the momentum force leads to the formation of bubble blanket. CHF condition occurs when the momentum force overwhelms the hydrodynamic pressure and surface tension. The formulation of the correlation is

$$\frac{q''_{max}}{q''_{max,z}} = \frac{1+\cos\theta}{2.096}\left[\frac{2}{\pi}+\frac{\pi}{4}(1+\cos\theta)\cos\Omega\right]^{1/2}$$

1.2.3. Techniques of boiling surface treatment

The surface modification techniques to increase the number of bubble nucleation sites has been developed, arising from mechanical surface treatments such as polishing technique and micro pinning technique. The technique now extends to the nano-scaled surface modification due to the recent advancement of nanotechnology. Nanofluids, suspensions of nanosized particles in the fluid, have

been intensively studied in terms of synthetic method, characterization, thermal conductivity, and two phase heat transfer performance. Researchers demonstrated that the nanostructured surfaces generated by nanoparticles in fluids are attributed to the enhanced heat transfer performance by increasing critical heat flux (CHF) and heat transfer coefficient (HTC). A state of art review related to nanofluids technique for boiling heat transfer is available in literature [28]. Beside to the nanofluid technique, nanostructured surfaces have been recently developed. For instance, *Yao et al.* fabricated Cu and Si nanowires with different height using electro chemical deposition method [29]. Nano-porous surface was also fabricated using anodizing technique [30]. It was reported that the Al_2O_3 nano-porous surface is capable of lowering the incipient wall superheat, improving the boiling heat transfer coefficient. The effect of carbon nanotube (CNT) arrays on pool boiling was investigated by some researchers [31, 32]. The CNT was found to be very effective in enhancing the pool boiling performance. Pool boiling with Cu micro-porous surfaces prepared by electrochemical deposition technique was performed, and CHF was improved with the reduction of boiling incipient superheat [33]. The enhancement of pool boiling performance with nanostructured surfaces can be explained with several important characteristics. Surface roughness generated by nanostructured surface reflects the potential that bubble could be nucleated on micro and nanosized cavities. The surface wettability could be increased with an increase of the surface roughness according to Wenzel's model, which is very significant effect on enhancing the boiling heat transfer performance [34]. In addition, capillarity of a fluid toward the bubble nucleation sites was emerged as a critical characteristic for an enhanced boiling heat transfer. The capability of

replenishing a fluid on the boiling site by the capillary force causes the delay of dry out on the boiling surface [35]. A summary of the previous boiling heat transfer investigation using nanostructured surfaces is exhibited in Table 3.

Table 3. Summary of previous boiling investigations using nanostructured boiling surfaces

Author	**Nanostructured surfaces**	**Fluid**	**CHF(W/cm^2)**	**HTC(nanosurface/bare)**
Xu et al. [36]	Foam	Acetone	80-140	2
Li et al. [37]	Mesh	DI water	175-360	20
Vemuri et al [38]	Nano porous media	FC-72	5	NA
Rainey et al [39]	Pin fin and microporous coating	FC-72	26.3-129.4	1.75
Oconnor et al. [40]	Micro porous media	FC-72	30	2.5
Arik et al. [41]	Micro porous coated silicon	FC-72	19.4-47	NA
Chen et al. [42]	Si & Cu NWs on Si substrate	DI water	435	20
Li et al. [43]	Cu NRs on Cu substrate	DI water	150-160	NA
Hendricks et al. [44]	ZnO flower surface on Al and Cu substrate	DI water	82.5	2.3
Ujereh et al. [32]	MWCNTs on Si and Cu substrate	FC-72	18.1 & 26	1.32 & 2.65
Li et al. [35]	Multiscale modulated porous structures	DI water	225-435	3
Betz et al. [45]	Heterogeneous (hydrophilic+hydrophobic) structures	DI water	90-190	2
Forrest et al. [46]	SiO_2 nanoparticle thin film coatings	DI water	158-173	2
Lu et al. [47]	Si NWs array on Si substrate	DI water	223	3
Yao et al. [29]	Cu NWs & SiNWs on Si substrate	DI water	80-134	NA
Kim et al. [48]	ZnO NRs SiO_2 substrate	DI water	112-232	1.7
Lee et al. [30]	Al_2O_3 nanoporous structure	DI water	9	1.2

1.3. References

[1] M. M. Moslehi, S. C. Shatas, and K. C. Saraswat, Appl. Phys. Lett. 47, 1353 (1985)

[2] G. Rupprecht and R. O. Bell, Phys. Rev. 135, A748-A752 (1964)

[3] K. Sue, M. Suzuki, K. Arai, T. Ohashi, H. Ura, K. Matsui, Y. Hakuta, H. Hayashi, M. Watanabe, and T. Hiaki, Green Chemistry 8, 634 (2006)

[4] J.-P. Jolivet, S. Cassaignon, C. Chaneac, D. Chiche, O. Durupthy, and D. Portehalt, Compets Rendus Chimie. 13, 40 (2010)

[5] J. A. Rodriguez and M. Fernandez-Garcia, Synthesis, Properties, and Applications of Oxide Nanomaterials, Wiley, 2007, 119-133

[6] J.-P. Jolivet, C. Froidefond, A. Pottier, C. Chaneac, S. Cassaignon, E. Tronc, and P. Euzen, J. Mat. Chem. 14, 3281 (2004)

[7] E. C., Subbarao, H. S., Miati, K. K., Srivastava, Phys Solidi. 21, 9 (1974)

[8] J. Zhang and L. GaO, J.Solid State Chem. 177, 1425 (2004)

[9] V. R. Palkar, NanoStructured Materials. 11, 369 (1999)

[10] L. V. Interrante, M. J. Hampden-Smith, Chemistry of Advanced Materials: An Overview, Wiley, 1998

[11] I. Ruth Mangani, C. W. Park, J. Kim, Electrochimica Acta. 52, 1451 (2006)

[12] I. Capek, Adv. Collid Interface Sci. 110, 49 (2004)

[13] M. J. Rosemary and T. Pradeep, J. Colloid Interface Sci. 268, 81 (2003)

[14] G.-D. Wei, Y. Deng, C.-W. Nan, Chem. Phys. Lett. 367, 521 (2003)

[15] Y. Sun, N. G. Ndifor-Angwafor, D. J. Riley, M. N. R. Ashfold, Chem. Phys. Lett. 431, 352 (2006)

[16] G. A. Parks, Chem. Rev. 65, 177 (1965)

[17] J. Theodoor and G. Overbeek, Adv. in Colloid Interface Sci. 16, 17 (1982)

[18] V. K. Lamer and R. H. Dinegar, J. Am. Chem. Soc. 72, 4847 (1950)

[19] E. Matijevic, Langmuir 2, 12 (1986)

[20] S. Nukiyama, J. Japan Soc. Mech. Eng. 37, 367 (1934)

[21] W. M. Rohsenow, Trans. ASME, 74, 969 (1952)

[22] R. I. Vachon, G. H. Nix, and G. E. Tanger, ASME J. Heat Transfer, 90, 239 (1968)

[23] K. Stephan and M. Abdelsalam, Int. J. Heat and Mass Transfer, 23, 73 (1980)

[24] V. M. Borishanaky, Problems of Heat Transfer and Hydraulics of Two-Phase Media, Pergamon Press, 16 (1969)

[25] N. Zuber, AEC Report AECU-4439, June (1959)

[26] J. H. Lienhard and V. K. Dhir, NASA CR-2270, July (1973)

[27] S. G. Kandlikar, J. Heat Transfer, 123, 1071 (2001)

[28] H. Kim, Nanoscale Research Lett. 6, 415 (2011)

[29] Z. Yao, Y. W. Lu, and S. G. Kandlikar, Int. J. Thermal Sci. 50, 2084 (2011)

[30] C. Y. Lee, M. M. H. Bhuiya, and K. J. Kim, Int. J. Heat and Mass Transfer, 53, 4274 (2010)

[31] S. Kim, H. D. Kim, H. Kim, H. S. Ahn, H. Jo, H. Kim, and J. Kim, Exp. Thermal and Fluid Sci. 34, 487 (2010)

[32] S. Ujerej, T. Fisher, and I. Mudawar, Int. J. Heat and Mass Transfer, 50, 4023 (2007)

[33] M. S. El-Genk and A. F. Ali, Int. J. Multiphase Flow, 36, 780 (2010)

[34] N. A. Patankar, Langmuir, 26, 8941 (2010)

[35] C. H. Li, T. Li, P. Hodgins, C. N. Hunter, A. A. Voevodin, J. G. Jones, and G. P. Peterson, Int. J. Heat and Mass Transfer, 54, 3146 (2011)

[36] J. Xu, X. Ji, W. Zhang, and G. Liu, Int. J. Multiphase Flow, 34, 1008 (2008)

[37] C. Li, and G. P. Peterson, J. Heat Transfer-Transactions of the ASME, 129, 1465 (2007)

[38] S. Vemuri and K. J. Kim, Int. Comm. in Heat and Mass Transfer, 32, 27 (2005)

[39] K. N. Rainey and S. M. You, J. Heat Transfer-Transactions of the ASME, 122, 509 (2000)

[40] J. P. Oconnor and S. M. You, J. Heat Transfer-Transactions of the ASME, 117, 387 (1995)

[41] M. Arik, A. Bar-Cohen, and S. M. You, Int. J. Heat and Mass Transfer, 50, 997 (2007)

[42] R. Chen, M.-C. Lu, V. Srinivasan, Z. Wang, H. H. Cho, and A. Majumdar, Nano Lett. 9, 548 (2009)

[43] C. Li, Z. Wang, P.-I. Wang, Y. Peles, N. Koratkar, and G. P. Peterson, Small, 4, 1084 (2008)

[44] T. J. Hendricks, S. Krishnan, C. Choi, C.-H. Chang, and B. Paul, Int. J. Heat and Mass Transfer, 53, 3357 (2010)

[45] A. R. Betz, J. X, H. Qiu, and D. Attinger, Appl. Phys. Lett. 97, 141909 (2010)

[46] E. Forrest, E. Williamson, J. Buongiomo, L.-W. Hu, M. Rubner, and R. Cohen, Int. J. Heat and Mass Transfer, 53, 58 (2010)

[47] M.-C. Lu, R. Chen, V. Srinivasan, V. P. Varey, and A. Majumdar, Int. J. Heat and Mass Transfer, 54, 5359 (2011)

[48] H.D. Kim and M. H. Kim, Appl. Phys. Lett. 91, 014104 (2007)

Chapter 2. Growth and Assembly of ZnO Nanocrystals in a Continuous Flow Microreactor

Changho Choi, Yu-Wei Su, and Chih-hung Chang

Crystal Engineering Commuication accepted manuscript

Assembly of nanocrystals is considered one of the most promising approaches to design nano-, microstructures, and complex mesoscopic architectures. A variety of strategies to induce nanocrystal assembly have been reported, including directed assembly methods that apply external forces to fabricate assembled structures. In this study ZnO nanocrystals were synthesized in an aqueous solution using a continuous flow microreactor. The growth mechanism and stability of ZnO nanocrystals were studied by varying the pH and flow conditions of the aqueous solution. It was found that convective fluid flow from Dean vortices in a winding microcapillary tube could be used for the assembly of ZnO nanocrystals. The ZnO nanocrystal assemblies formed three-dimensional mesoporous structures of different shapes including a tactoid and a sphere. The assembly results from a competing interaction between electrostatic forces caused by surface charge of nanocrystals and collision of nanocrystals associated with Dean vortices. Dispersion behaviours of the ZnO assembly in some solvents were also studied. MeOH, a strong precipitant, led to the precipitation of the ZnO assembly. This study shows that the external forces from convective fluid flow could be applied to fabricate assembly of functional metal oxides with complex architectures using a continuous flow microreactor.

2.1. Introduction

The physical and chemical properties of inorganic nanomaterials depend strongly on their size and morphologies [1]. Understandings of colloidal nanocrystal nucleation and growth and ability to tailor their size and morphologies are essential in nanotechnology. Significant effort and progress toward the understandings of nanocrystal growth mechanism and kinetics have been made [1-5]. These advances facilitate the preparation of well-defined nanocrystals with specific morphologies [6-13]. It is crucial to understand the key factors that govern the nanocrystal assembly in order to fabricate desired nano- and microstructures for targeted optical, electronic, and biological applications [14]. Self- assembly of unique structures consisting of various semiconductor and metal oxide nanocrystals has been demonstrated [15-29]. For instance, self-assembly driven by appropriately adjusting the evaporation rate of solvent or interaction between capping ligands adsorbed on surface of nanocrystals has been used to create two dimensional patterns of a single or several layers [30]. In other directed self-assembly processes, external force is applied to guide the nanobuilding blocks into assembled structures. For example, Israelachvili *et al*. applied various forces such as normal and shear forces to nanocrystals and investigated the effect of these forces on nanocrystal motion [31-34]. In addition, they have reported that external forces play an important role in achieving the desired assembly [35]. The external forces could be generated by compressive or shear stresses, gravity, magnetic or electric fields. Although various approaches have been reported for directed nanocrystal assembly, to the best of our knowledge, the effect of external

forces from convective fluid flow on nanocrystal assembly within a microchannel has not been addressed.

ZnO is an important transparent wide band gap semiconductor material that can be prepared by various solution-based processes. In this study, we synthesize ZnO nanocrystals with their diameters around 5nm using a continuous flow microreactor. The characteristics of the continuous flow microreactor are the following: (1) The microreactor facilitates the homogenous nucleation and growth of the nanocrystals by minimizing the pH and temperature gradient in the solution. (2) The system enables us to tailor nanocrystal growth process by simply controlling system parameters such as reaction temperature and flow rate, leading to faster and more efficient preparation of nanocrystals. (3) The continuous flow microreactor could be used to fabricate various nanostructured surfaces via direct delivering of nanocrystals on targeted substrates.[36-38] The processing parameters including solution pH and solution flow rate were varied to investigate their effects on the growth of ZnO nanocrystals. In particular, we investigated ZnO nanocrystal assemblies induced by external forces from convective fluid flow.

2.2. Experimental

2.2.1. Synthesis of ZnO nanocrystals in a continuous flow microreactor

The apparatus used to prepare ZnO nanocrystals consists of a microprocessor-controlled dispensing pump (Ismatec micropumps), 1.22 mm ID Tygon ST tubing (Upchurch Scientific), and a micro T-mixer (Upchurch scientific). The schematic diagram of the system is shown in Figure 2.1. $Zn(NO_3)_2 \cdot 6H_2O$ (Sigma Aldrich) and NaOH (Mallinckrodt Chemicals) were used as received

without further purification. An aqueous solution of 0.005 M $Zn(NO_3)_2 \cdot 6H_2O$ and the aqueous NaOH required to produce the desired pH were contained in two separate beakers. The solutions of reactants were pumped into the two Tygon tubes and were mixed through the micro-T-mixer. The reactant mixture was then passed through a helical structured reactor made by wrapping a 1.3m long Tygon tube around a cylinder. By immersing the reactor in an oil bath, the reaction temperature (70 ℃) was maintained throughout the growth process. ZnO nanocrystals generated inside the reactor were directly deposited on TEM grids (Ted Pella). Several approaches of collecting ZnO nanocrystals on TEM grids were tested to verify that the observed ZnO assembly under TEM is independent of TEM sample preparation method. We observed that evaporation of solvent did not change the assembly of ZnO nanocrystals. In this study, three different volume flow rates (6.8, 14.7, and 28.1 mL/min) were tested to investigate the effects of external forces from convective fluid flow on ZnO nanocrystal assembly.

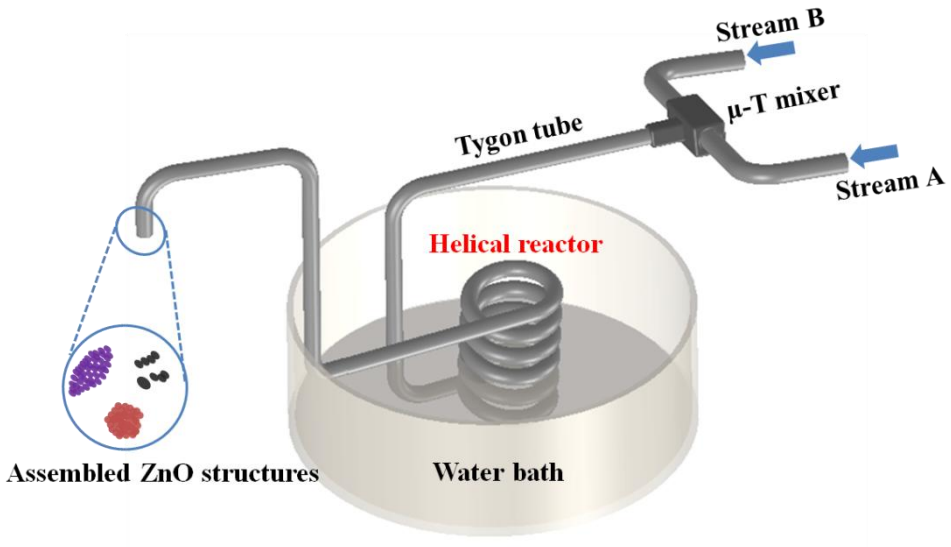

Figure 2.1. Scheme of the continuous flow microreactor system.

2.2.2. ZnO nanocrystal characterization

The size, shape and structure of ZnO nanocrystals and their assembly were analyzed using High Resolution Transmission Electron Microscopy (HRTEM) with a FEI Titan operated at 300kV. Selected Area Electron Diffraction (SAED) pattern was generated by Fast Fourier transformation (FFT) of the HRTEM image. X-ray diffraction (XRD) spectra of the nanocrystals were obtained using a D8 Discover (Bruker) with Cu *Kα* radiation (acceleration voltage: 40kv, flux: 40mA). UV-visible spectroscopy (Ocean Optics Inc.) was used to study the optical property of ZnO nanocrystals.

2.3. Results and Discussion

2.3.1. pH effect on growth and stability of ZnO nanocrystals

For an understanding of the ZnO nanocrystal nucleation and growth mechanism in the continuous flow system, the species distribution of zinc complex ions should be identified with respect to the solution pH. The speciation diagram of zinc complex ions is already described in the chapter 1.1 (Figure 1.2). constructed as shown in Figure 2 by using a Visual MINTEQ program [39]. The hydrolysis ratio is increased with an increase of pH value and yields zinc-aquo-hyroxo ions $[Zn(OH_2)_{4-n}(OH)_n]^{2-n}$, which are the precursors responsible for the nucleation of ZnO nanocrystals. Once sufficient amounts of the precursors are present in the aqueous medium, ZnO nuclei are formed via a condensation reaction. The subsequent condensation reaction continues by a combination of diffusion and reaction of the precursors, consequently leading to the creation of ZnO nanocrystals. The precursors are bridged by OH^- ligands, initially forming the

unstable $Zn(OH)_2$, which is then transformed into $ZnO \cdot H_2O$ by a spontaneous dehydration reaction. At pH=13, $[Zn(OH)_4]^{2-}$ and $Zn(OH)_3^-$ are the dominant precursors for the nucleation and growth of ZnO nanocrystals, according to the speciation diagram. A comprehensive study about the growth mechanism and growth habits of ZnO crystals with $Zn(OH)_4^{2-}$ as a precursor was reported by Li *et al.* [40]. When electrically charged precursors, $[Zn(OH)_4]^{2-}$ and $Zn(OH)_3^-$, form polyanions by the condensation reaction, the nanocrystal growth is limited due to the charge accumulation. It was reported that polyanions can form the solid phase of nanocrystals as far as they remain inert and stable in the aqueous medium [41].

The pH of the solution also plays a critical role in determining the stability of ZnO nanocrystal dispersion in the aqueous medium. In order to keep ZnO nanocrystals dispersed stably, the nanocrystals should repel each other to prevent close contact with one another. The repulsive force of the nanocrystals is originated from the surface charge of the nanocrystals. Since the surface of ZnO nanocrystals has OH^- ligands, the pH value of the solution determines the surface charge via acid-base equilibrium. The point of zero charge (PZC) of ZnO colloidal dispersion is reported to range between pH 9 and 10 [41]. For ZnO nanocrystals prepared at pH=13 (far from the PZC of ZnO), a negative surface charge is created resulting in a strong repulsive interaction between nanocrystals. Stable ZnO nanocrystal dispersions were obtained at pH=13 as a result of the electrostatic repulsion force between ZnO nanocrystals. Primary ZnO nanocrystals with an average diameter around 5 nm that are free of agglomeration can be seen in the TEM image in Figure 2.2a. The HRTEM image of a typical primary ZnO nanocrystal is presented

in Figure 2.2b. Based on the FFT analysis of the primary nanocrystal, the crystal planes are annotated in the HRTEM image.

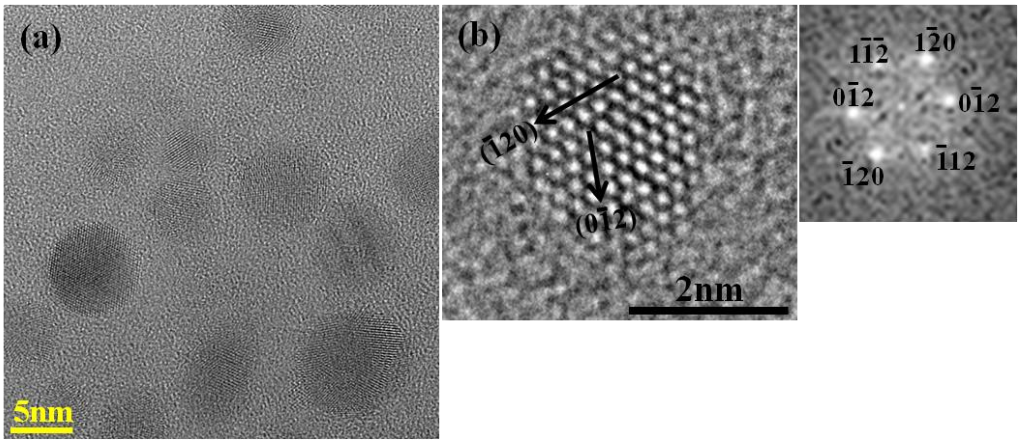

Figure 2.2. HRTEM images of ZnO nanocrystals formed at pH=13: (a) dispersed nanocrystals and (b) typical primary ZnO nanocrsytal with FFT image.

ZnO nanocrystal dispersion is stable for a long period of time. The long term stability of ZnO nanocrystal dispersion was verified by analysing HRTEM images of ZnO nanocrystals collected after the aging process had taken place for several months.

ZnO nanocrystals were also synthesized at pH=9.5, which corresponds to the PZC of ZnO nanocrystal dispersion, to see the pH effect on the ZnO growth. At pH=9.5, the dominant precursor for the ZnO formation is $Zn(OH)_2$ (aq). $Zn(OH)_2$ (aq), an electrically neutral ion, continues the condensation reaction until the ZnO crystal precipitates [41]. We observed this phenomenon visually during the synthesis of ZnO nanocrystals. Large white particles that can be recognized by the naked eye were precipitated immediately at pH= 9.5 while the solution containing ZnO nanocrystals synthesized at pH=13 is completely transparent. The collected powders were analysed by XRD after repeated washing by MeOH and DI water.

The XRD data exhibits the characteristic zinc oxide peaks without other secondary phases (Figure 2.3).

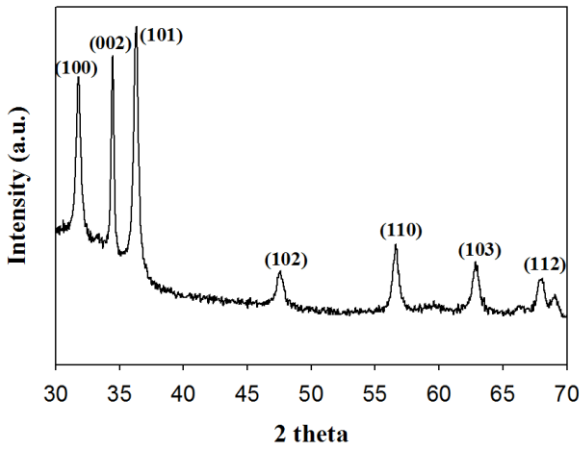

Figure 2.3. X-ray diffraction patterns of ZnO nanocrystals prepared at pH=9.5.

HRTEM images of the ZnO synthesized at pH=9.5 show a network of aggregated ZnO nanocrystals with an irregular morphology (Figure 2.4). The FFT analysis also confirms that the aggregated ZnO nanocrystals are polycrystalline. When pH value of the solution stays near the PZC of ZnO nanocrystal dispersion, the surface charge of the particle reduce to near neutral, resulting in weak repulsive interaction between the nanocrystals. Depletion of repulsive forces acting on the nanocrystal surfaces increases the rate of aggregation. In contrast, surface charge will decrease the rate of aggregation [4].

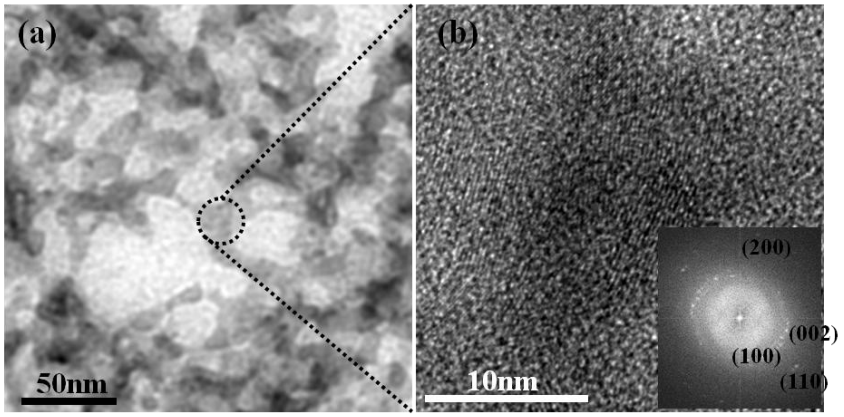

Figure 2.4. Low resolution (a) and high resolution (b) TEM images of ZnO nanocrystals formed at pH=9.5 (inset shows the FFT analysis).

2.3.2. Effect of external forces of convective flow on ZnO nanocrystal assembly

Effect of Dean vortices on the aggregation of ZnO nanocrystals was investigated by varying the volumetric flow rates using solution at a pH value of 9.5. All experiments resulted in network of ZnO nanocrystals with similar irregular shape. The influence of Dean vortices on the morphology of ZnO nanocrystal is not obvious at these experimental conditions. We then examined ZnO nanocrystal assembly by performing ZnO nanocrystal synthesis using solution at a pH value of 13 at three different flow rates (6.8, 14.7, and 28.1 [mL/min]). The temperature of the solution is calculated with respect to the volumetric flow rates and the length of the tube. The results are shown in Figure 2.5. Although the rate of temperature increase is different for the various flow rates, the outlet temperatures reaches the desired reaction temperature (70℃) regardless of the flow rates.

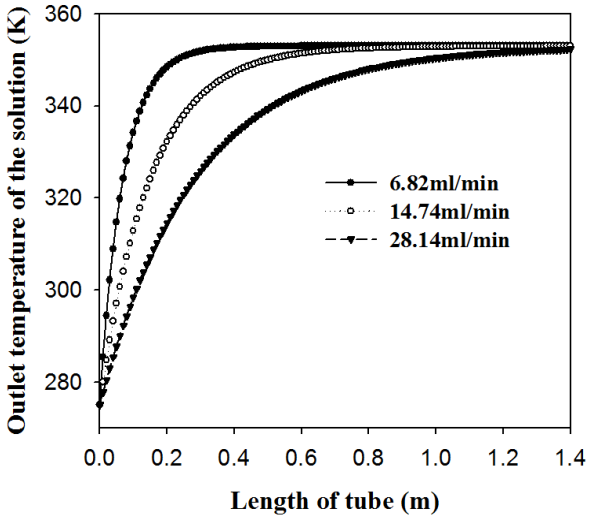

Figure 2.5. Temperature of the solution as a function of the length of tube and volumetric flow rates.

In order to understand the effect of fluid flow on the assembly of ZnO nanocrystals, hydrodynamics of the helical tubular reactor must be considered. It has been established in the literature that helical flow in curved micro channel would enhance the fluid mixing and heat transfer rate.[42, 43] The main feature of fluid dynamics inside a helical reactor is the generation of Dean vortices induced by the imbalance between viscous force and centrifugal force. The magnitude of Dean vortices could be characterized by the Dean number. Dean number, *K*, is determined by multiplying the Reynolds number by the geometry factor of the helical reactor.

$$K = \mathrm{Re}\sqrt{\frac{d}{R}}$$

Here, *d* denotes the hydraulic diameter and *R* denotes the mean radius of curvature of the channel. High Dean numbers will give rise to Dean vortices (two counter rotating vortices) across the cross-section of the curved tube due to the enhanced

centrifugal force. The three different flow rates used to explore the assembly of ZnO nanocrystals correspond to a Dean number value of 36, 78, 150, respectively in the order of low to high flow rates. The hydrodynamic study on the helical reactor with given Dean numbers is performed by using a COMSOL Multiphysics program. The simulation is developed for a steady, laminar, incompressible, and single phase flow of a Newtonian fluid with constant physical properties. The helical reactor geometry, the simulated contours of the axial velocity component, and velocity profile in the reactor are exhibited in Figure 2.6. Due to the symmetry of the cross-sectional area of the helical reactor, only half of the cross sectional contour image is displayed. The simulation results show the formation of Dean vortices with typical characteristics at all three flow rates [42, 43]. It is well known that in the occurrence of Dean vortices, the location of maximum velocity moves toward the outside wall of the tube. This trend is observed in the simulated contour images and the velocity profiles for all Dean numbers (Figure 2.6). The most relevant feature of Dean vortices to ZnO nanocrystal assembly is the enhanced mixing effect which increase the collision frequency between ZnO nanocrystals.

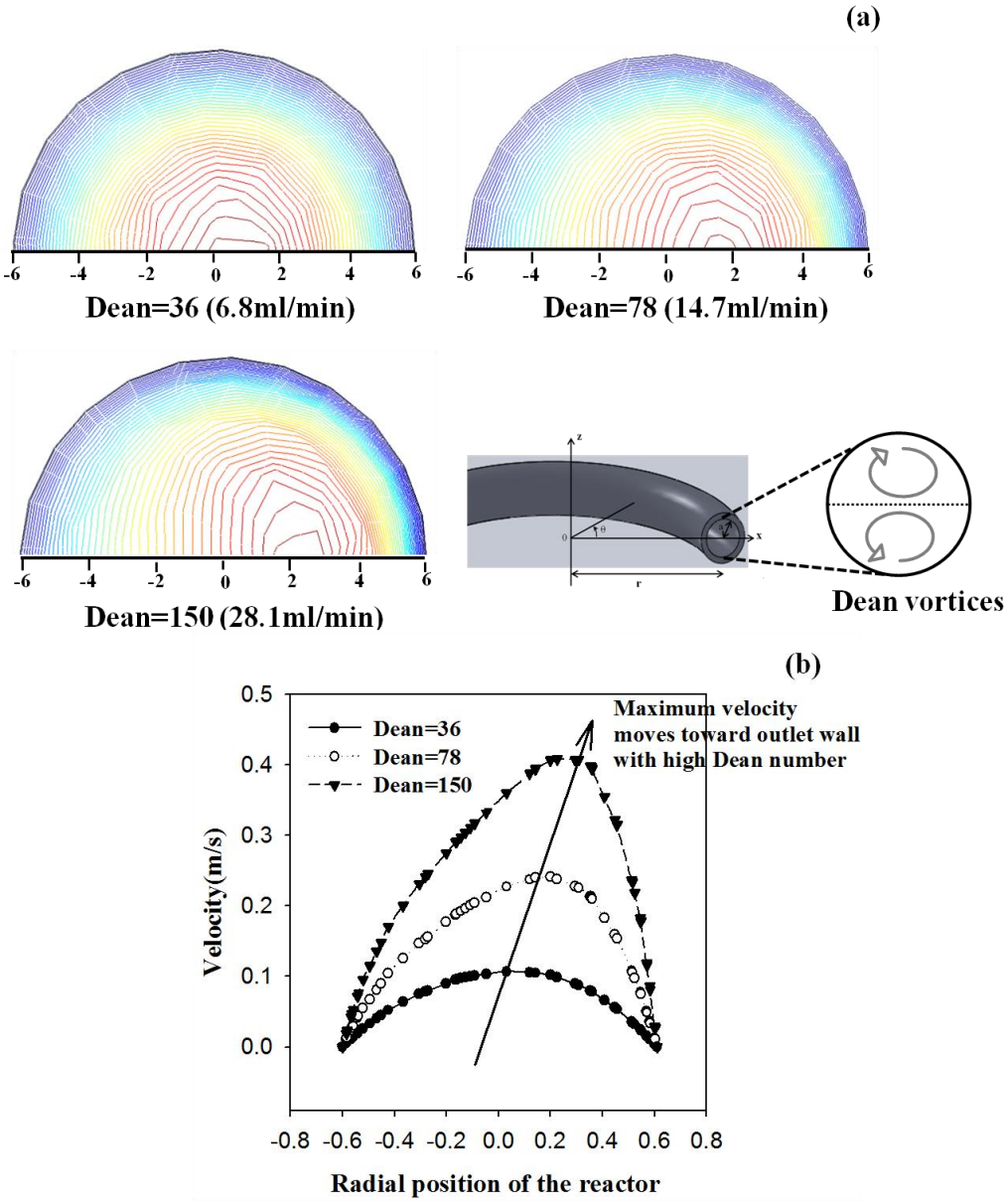

Figure 2.6. Hydrodynamic study of the helical reactor: (a) helical reactor geometry and contour of the axial velocity component in the reactor at $\theta=\pi/2$, (b) velocity profile with respect to the Dean numbers in the reactor at $\theta=\pi/2$.

Figure 2.7 exhibits the HRTEM image of ZnO nanocrystals formed at a Dean number of 36. At this Dean number, Dean vortices are relatively insignificant as confirmed by a minor shift of the maximum velocity toward the outside wall of the reactor (Figure 2.6). Figure 2.7a shows single ZnO nanocrystals along with

larger aggregates consisting of two or three primary nanocrystals. The larger aggregates are likely formed by an attachment mechanism. Primary ZnO nanocrytsals in Figure 2.7a are each labelled with a "P" while ZnO aggregates grown by the attachment mechanism are labeled with an "A". Figure 2.7b displays a closer look of one of the ZnO aggregates. Primary ZnO nanocrystal attached to one another without sharing the same crystallographic orientation. Oriented attachment is being investigated as one of the most important mechanisms in solution-based nanocrystal synthesis [4, 10, 12]. In the oriented attachment, nanocrystals having common crystallographic orientations combine together to form larger particles, followed by the elimination of the interface[11]. Defects of edge and screw misorientations can be formed during the oriented attachment growth, which is referred as imperfect oriented attachment mechanism. The characteristic of the imperfect oriented attachment mechanism is that primary nanocrystals coalesce, forming epitaxial assembly with defects of edge and screw dislocations [44]. HRTEM results indicate the ZnO aggregates formed under Dean vortices did not follow the oriented attachment mechanism.

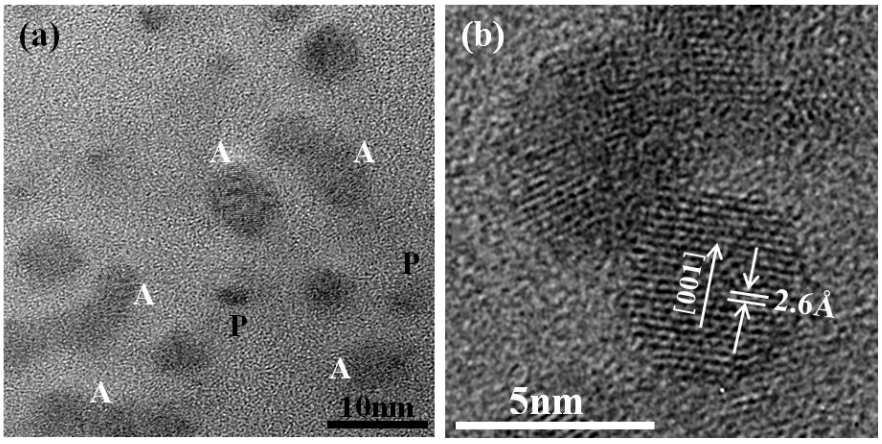

Figure 2.7. HRTEM images of ZnO nanocrystals synthesized at Dean number=36: (a) low magnification and (b) aggregated ZnO nanocrystal.

As Dean number increases to 78, the characteristics of Dean vortices becomes more significant, showing a pronounced shift of the maximum velocity toward the outside wall of the reactor (Figure 2.6). More assembly of ZnO nanocrystals took place, which was a result of enhanced mixing from Dean vortices (Figure 2.8). TEM image given in Figure 2.8 shows that ZnO nanocrystals assemble to form three dimensional tactoids with their length varying from 100 nm to several μm. The EDX spectrum reveals that the assembly consists of ZnO nanocrystals.

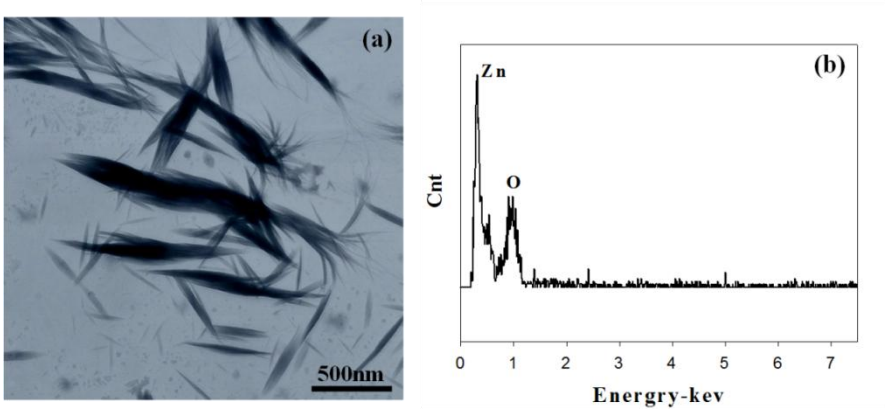

Figure 2.8. TEM image of three-dimensional mesoporous tactoids formed by ZnO nanocrystals and corresponding EDX spectrum.

In order to elucidate the assembly process and structure, HRTEM analyses of a typical tactoid structure were performed. Figure 2.9 shows a whole tactoid structure, edge area, and central area of the tactoid structure. In the edge area of the structure, some of ZnO nanocrystals form irregular structure (Figure 2.9b) while many primary nanocrystals still visible. These crystalline ZnO particles were surrounded by an amorphous matrix. It is speculated that amorphous ZnO was generated and participated in the aggregation process along with ZnO nanocrystals.

The formation of amorphous ZnO may be facilitated at higher Dean vortices which presumably retard the ordering of ZnO. HRTEM image of an aggregate of ZnO nanocrystals in the edge area is shown in Figure 2.9-1. It can be seen that three primary ZnO nanocrystals coalesce via the attachment growth mechanism. Primary ZnO nanocrystals can also be observed in the edge area of the tactoid structure, where lattice fringe of a typical nanocrystal along with its FFT is exhibited in Figure 2.9-2. In the central area of the tactoid structure, ZnO was aggregated by a cluster of primary ZnO nanocrystals and amorphous ZnO as well (Figure 2.9c). It seems that mesopores were created between the grouped clusters. In order to account for the formation of the tactoid structure in the continuous flow microreactor, the effect of the Dean vortices should be considered. At Dean number=78, fluid mixing effect is enhanced due to the adequate strength of the Dean vortices, which increases the collision frequency of the ZnO nanocrystals. The enhanced mixing led to the formation of larger aggregates. The repulsion forces between ZnO nanocrystals reduce the rate of aggregation. In the oriented attachment mechanism, the particles undergo continuous rotation and interaction to find perfect lattice match [45]. The external force exerted by the Dean vortices overcame the repulsive force, however prevented the relative rotation of the ZnO nanocrystals that could lead to the oriented attachment growth of nanocrystals.

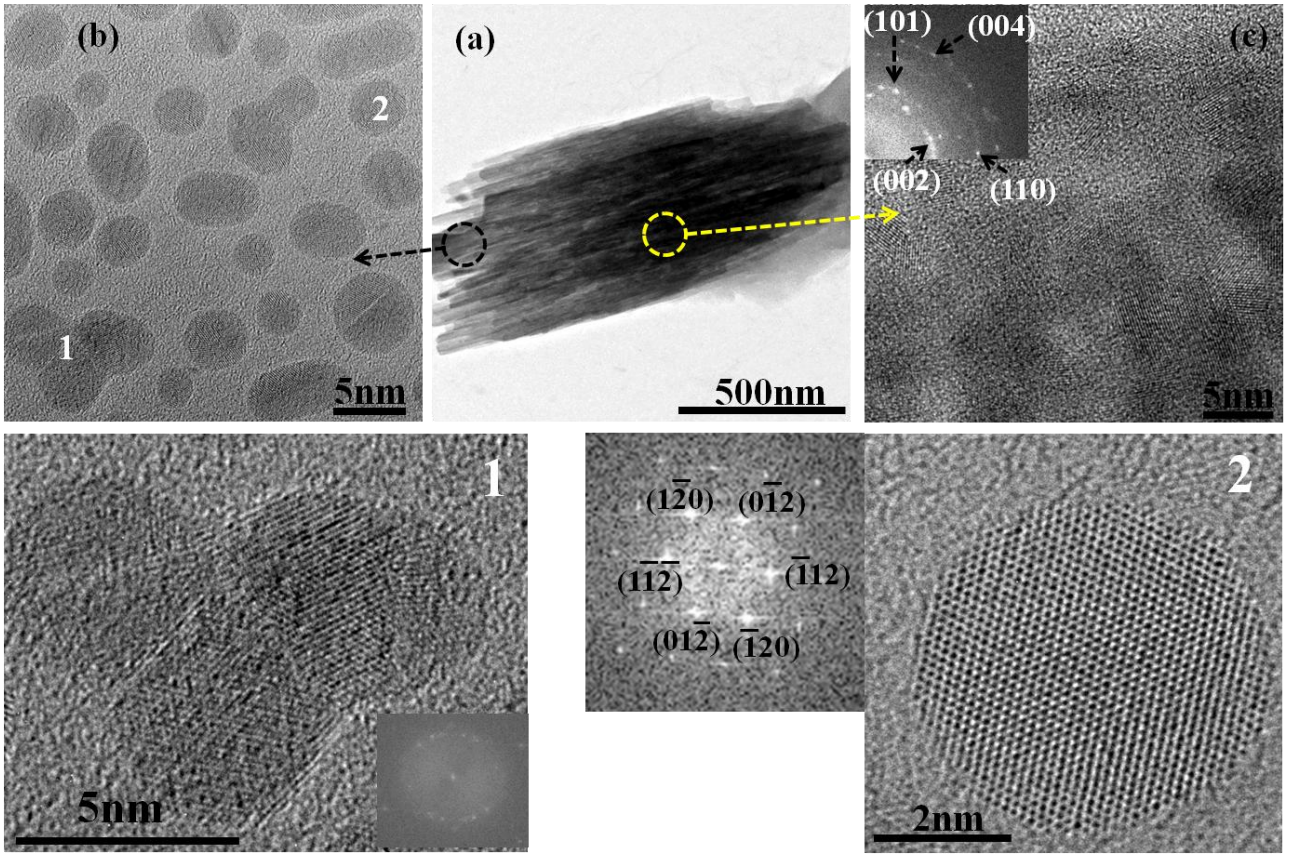

Figure 2.9. HRTEM images of ZnO nanocrystal assembly formed at Dean number=78: (a) a single tactoid, (b) edge area of the structure, (c) central area of the structure with a FFT image.

Dean vortices are stronger at the highest flow rate we tested (Dean number=150) where the maximum velocity apparently shift toward the outside wall of the reactor according to the velocity profile simulation of the reactor (Figure 2.6). At this Dean number, the microreactor yields ZnO nanocrystal assemblies with a spherical structure around 90 nm diameter size. For a more detailed analysis of the ZnO assembly structure, HRTEM images of a spherical ZnO assembly were taken (Figure 2.10b and c). The images in Figure 2.10 show that the spherical ZnO assembly is composed of a number of primary ZnO nanocrystals and amorphous ZnO aggregated randomly in an interlocking manner. At Dean number=150, the enhanced mixing driven by the external force provides the nanocrystals with sufficient energy and higher collision frequency that drove the formation of three dimensional mesoporous ZnO spheres.

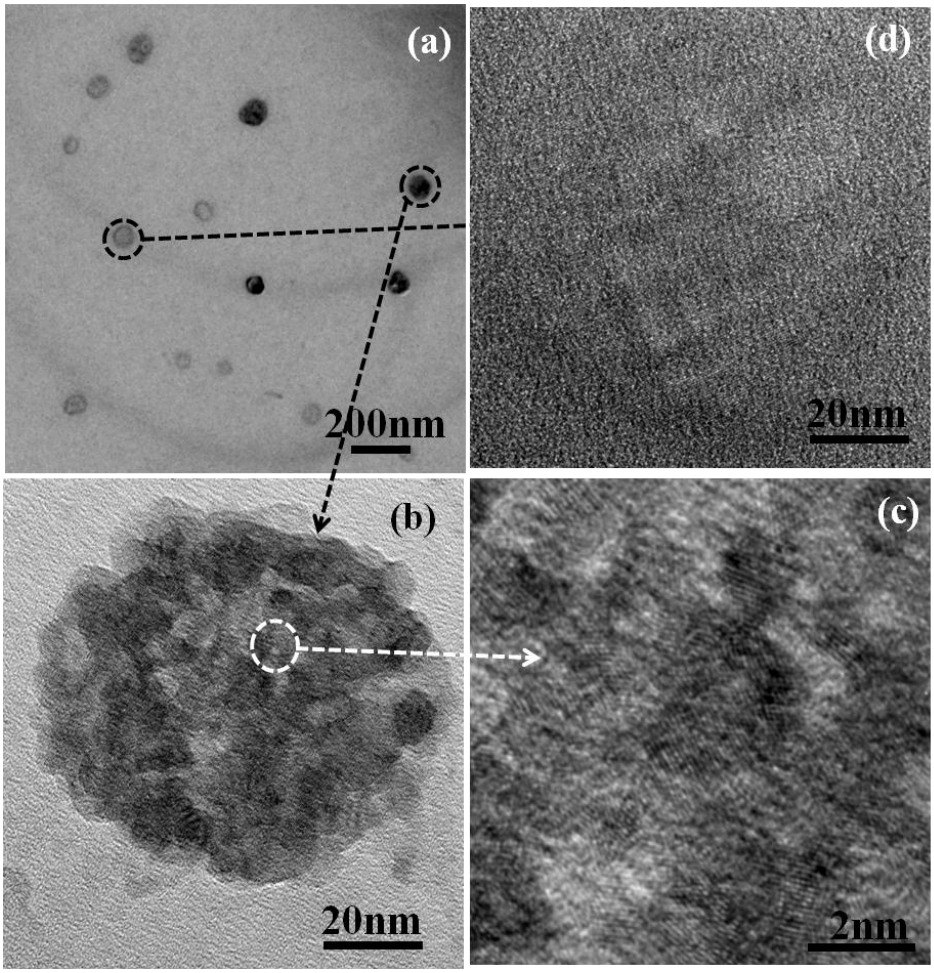

Figure 2.10. HRTEM images of ZnO nanocrystals aggregated at Dean number=150.

Although the hydrodynamic studies offer some clues to explain the formation of three dimensional mesoporous ZnO assemblies, some questions still remain: (1) What mechanism determines the shape of the assembled structure under the given external force? and (2) Why doesn't infinite agglomeration take place under high Dean vortices, yielding the various assembled structures such as the tactoid structure or the spherical structure? To answer these questions, *in-situ* studies with direct measurement tools should be performed. A schematic diagram is given in Figure 2.11 with an attempt to illustrate the impact of the Dean vortices on the ZnO nanocrystal assembly.

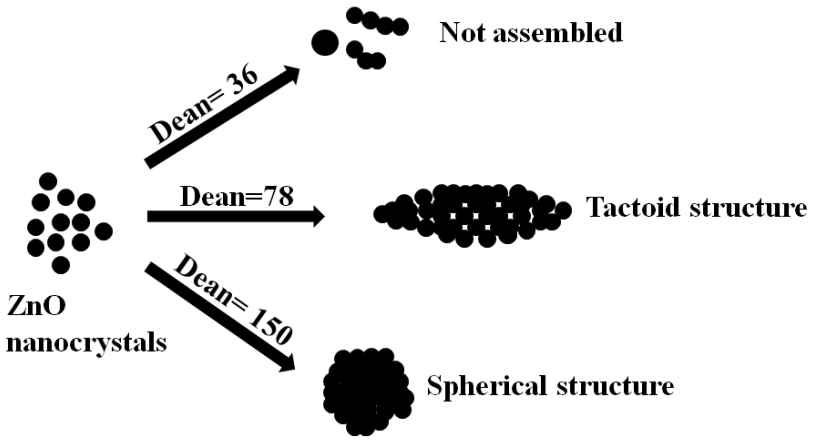

Figure 2.11. Schematic diagram of the ZnO nanocrystal assemblies.

Although some questions regarding to the exact mechanism behind the ZnO nanocrystal assembly still remain, this study demonstrates the capability of producing ZnO nanocrystals and assembling them into three-dimensional mesoporous structures continuously using Dean vortices within a microreactor.

Optical property of the ZnO assembly was studied by measuring its optical band gap. For the optical band gap measurement, each ZnO assembly was coated on a microscope glass slide. Figure 2.12 presents UV-visible spectrum of each ZnO assembly. Some methodologies have been proposed in estimating optical band gap of nanoparticles [46, 47]. In this study, Davis-Mott and Tauc models was employed to estimate optical band gap of the ZnO assembly coated on glass (inset in Figure 2.12). The optical band gap was estimated to 3.6 eV, 3.5eV, and 3.7 eV, which corresponds to no assembly, tactoid structure, and spherical structure, respectively.

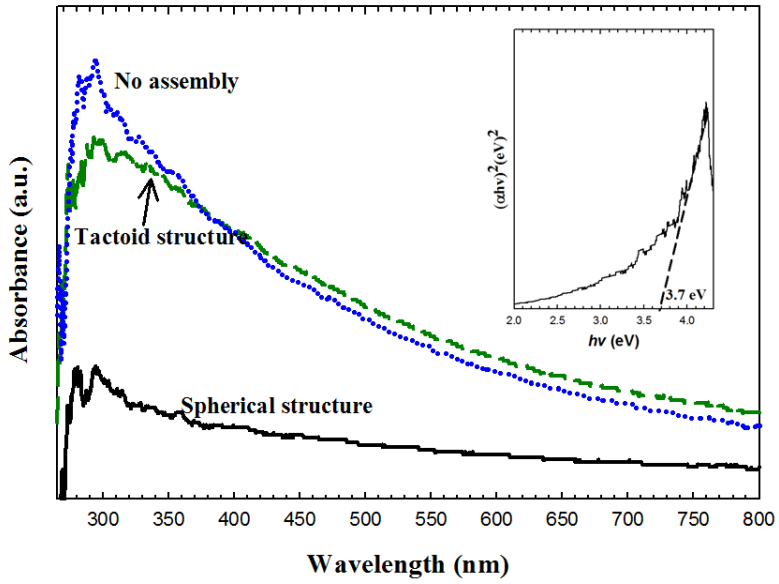

Figure 2.12. UV-visible spectroscopy of the ZnO assembly coated on glass.

2.3.3. Dispersion behaviours of the ZnO assembly in some solvents

The stable ZnO assembly in the aqueous media can be disturbed by adding some precipitants such as MeOH (ACS grade, 99.8 %) or EtOH (ACS grade, 99.8%). In order to study the dispersion behaviours of the ZnO assembly, sufficient amount of precipitants were added in the aqueous solution containing the stable ZnO assembly. It was found that MeOH is stronger precipitant than EtOH regardless of the types of the ZnO assembly. As MeOH was added, the solution became milky shortly, while it took longer time for EtOH. The amount of precipitated ZnO nanocrystals also depended on the type of the solvents, showing MeOH generated more precipitation of ZnO nanocrystals than EtOH. These results may be associated with the different polarity of the solvents. MeOH is known to have relatively higher polarity than EtOH. MeOH has a higher tendency to

surround the charged ZnO nanocrystals compared to EtOH, which leads to collapse of the double layer according to the double layer theory. Precipitated ZnO nanocrystals by MeOH were collected after purification process, and their morphologies were characterized by SEM (Figure 2.13).

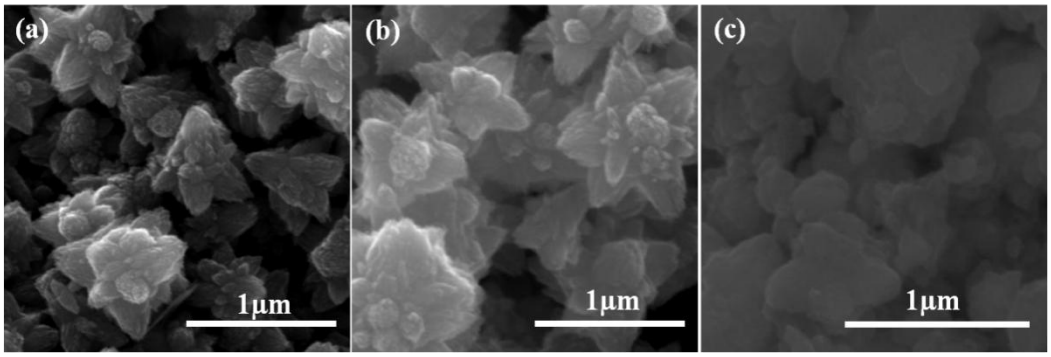

Figure 2.13. Morphologies of ZnO nanoparticles precipitated from (a) no assembly, (b) tactoid structure, and (c) spherical structure.

Typically flower like ZnO particles were formed during the precipitation of the ZnO assembly regardless of the structure of the ZnO nanoassembly. ZnO particles precipitated from the spherical ZnO assembly is slightly deviated from the typical flower like structure. The fact that adding MeOH did not change pH value of the solution indicates flower like ZnO particles were formed from the ZnO assembly not from new hydrolysis and condensation reaction of ZnO precursors. During the precipitation process, the Oswald ripening may govern behaviours of the ZnO assembly. Concentration of precipitated ZnO nanoparticles in MeOH was estimated. Yield of ZnO formation was also calculated based on the initial precursor concentration.

Assembly type	Conc. (mol)	Yield (%)
(a) Not assembled	**1×10^{-3}**	**40**
(b) Tactoid structure	**1.6×10^{-3}**	**64**
(c) Spherical structure	**1.57×10^{-3}**	**63**

2.4. Conclusion

Colloidal ZnO nanocrystals in aqueous solution were synthesized using a continuous flow microreactor. The pH value of the solution determines the stability of the ZnO nanocrystal dispersion. A white precipitate consisting of an irregular network of ZnO nanocrystals was obtained at pH=9.5. Stable ZnO nanocrystal dispersion with an average size around 5 nm could be obtained using a solution at pH=13. Convective fluid flow generated by Dean vortices in a winding microcapillary tube was used to assemble ZnO nanocrystals. Depending on the magnitude of Dean vortices, ZnO nanocrystals assemble into three-dimensional mesoporous structures with characteristic shape including a tactoid and a sphere. These assembled structures were precipitated out by adding MeOH or EtOH. Precipitated ZnO nanoparticles generally formed flower like ZnO structure during aging process. This study demonstrates the capability of producing ZnO nanocrystals and assembling them into three-dimensional mesoporous structures continuously using Dean vortices within a microreactor.

2.5. References

[1] Y. Yin and A. P. Alivisatos, Nature, 437, 664 (2005)

[2] C. B. Murray, D. J. Norris, and M. G. Bawendi, J. Am. Chem. Soc., 115, 8706 (1993)

[3] Y. W. Jun, J. S. Choi, and J. Cheon, Angewandte Chemie International Edition, 45, 3414 (2006)

[4] R. L. Penn, J. Phys. Chem. B, 108, 12707 (2004)

[5] J. Joo, S. G. Kwon, J. H. Yu, and T. Hyeon, Advanced Materials, 17, 1873 (2005)

[6] J. Tanori and M. P. Pileni, Langmuir, 13, 639 (1997)

[7] Y.-S. Fu, X.-W. Du, S. A. Kulinich, J.-S. Qiu, W.-J. Qin, R. Li, J. Sun, and J. Liu, Journal of the American Chemical Society, 129, 16029 (2007)

[8] H.-M. Xiong, Y. Xu, Q.-G. Ren, and Y.-Y. Xia, Journal of the American Chemical Society, 130, 7522 (2008)

[9] A. McLaren, T. Valdes-Solis, G. Li, and S. C. Tsang, Journal of the American Chemical Society, 131, 12540 (2009)

[10] Z. S. Hu, G. Oskam, R. L. Penn, N. Pesika, and P. C. Searson, Journal of Physical Chemistry B, 107, 3124 (2003)

[11] C. Pacholski, A. Kornowski, and H. Weller, Angewandte Chemie-International Edition, 41, 1188 (2002)

[12] F. Huang, H. Z. Zhang and J. F. Banfield, Nano Letters, 3, 373 (2003)

[13] J. S. Chen, T. Zhu, C. M. Li, and X. W. Lou, Angewandte Chemie-International Edition, 50, 650 (2011)

[14] A. N. Shipway, E. Katz, and I. Willner, Chemphyschem, 1, 18 (2000)

[15] M. Mo, J. C. Yu, L. Z. Zhang, and S. K. A. Li, Advanced Materials, 17, 756 (2005)

[16] B. A. Korgel and D. Fitzmaurice, Advanced Materials, 10, 661 (1998)

[17] J. H. Warner and R. D. Tilley, Advanced Materials, 17, 2997 (2005)

[18] E. Rabani, D. R. Reichman, P. L. Geissler, and L. E. Brus, Nature, 426, 271 (2003)

[19] E. V. Shevchenko, D. V. Talapin, A. L. Rogach, A. Kornowski, M. Haase, and H. Weller, Journal of the American Chemical Society, 124, 13958 (2002)

[20] M. Li, H. Schnablegger and S. Mann, Nature, 402, 393 (1999)

[21] B. Nikoobakht, Z. L. Wang, and M. A. El-Sayed, Journal of Physical Chemistry B, 104, 8635 (2000)

[22] B. R. Martin, D. J. Dermody, B. D. Reiss, M. M. Fang, L. A. Lyon, M. J. Natan, and T. E. Mallouk, Advanced Materials, 11, 1021 (1999)

[23] B. Liu and H. C. Zeng, Journal of the American Chemical Society, 127, 18262 (2005)

[24] J. J. Urban, D. V. Talapin, E. V. Shevchenko and C. B. Murray, Journal of the American Chemical Society, 128, 3248 (2006)

[25] A. Sukhanova, A. V. Baranov, T. S. Perova, J. H. M. Cohen, and I. Nabiev, Angewandte Chemie-International Edition, 45, 2048 (2006)

[26] T. P. Bigioni, X. M. Lin, T. T. Nguyen, E. I. Corwin, T. A. Witten, and H. M. Jaeger, Nature Materials, 5, 265 (2006)

[27] Y. Hu, T. Mei, J. Guo, and T. White, Inorganic Chemistry, 46,11031 (2007)

[28] B. A. Korgel, Nature Materials, 9, 701 (2010)

[29] M. P. Pileni, Accounts of Chemical Research, 40, 685 (2007)

[30] J. Xu, J. Xia and Z. Lin, Angewandte Chemie-International Edition, 46, 1860 (2007)

[31] M. Akbulut, N. Belman, Y. Golan, and J. Israelachvili, Advanced Materials, 18, 2589 (2006)

[32] M. Akbulut, A. R. G. Alig, Y. Min, N. Belman, M. Reynolds, Y. Golan, and J. Israelachvili, Langmuir, 23, 3961 (2007)

[33] D. Whang, S. Jin, Y. Wu, and C. M. Lieber, Nano Letters, 3, 1255 (2003)

[34] Y. Min, M. Akbulut, N. Belman, Y. Golan, J. Zasadzinski, and J. Israelachvili, Nano Letters, 8, 246 (2008)

[35] Y. Min, M. Akbulut, K. Kristiansen, Y. Golan, and J. Israelachvili, Nature Materials, 7, 527 (2008)

[36] T. J. Hendricks, S. Krishnan, C. Choi, C.-H. Chang and B. Paul, International Journal of Heat and Mass Transfer, 53, 3357 (2010)

[37] S. Y. Han, Y. J. Chang, D. H. Lee, S. O. Ryu, T. J. Lee, and C. H. Chang, Electrochemical and Solid State Letters, 10, K1 (2007)

[38] J. Y. Jung, N.-K. Park, S.-Y. Han, G. B. Han, T. J. Lee, S. O. Ryu, and C.-H. Chang, Current Applied Physics, 8, 720 (2008)

[39] G. P. Gallios and M. Vaclavikova, Environmental Chemistry Letters, 6, 235 (2008)

[40] W. J. Li, E. W. Shi, W. Z. Zhong, and Z. W. Yin, Journal of Crystal Growth, 203, 186 (1999)

[41] J.-P. Jolivet, Metal Oxide Chemistry and Synthesis from solution to solid state, John Wiley & Sons Ltd, Baffins Lane, Chichester, West Sussex, 2000

[42] S. Kim and S. J. Lee, Experiments in Fluids, 46, 255 (2009)

[43] F. Jiang, K. S. Drese, S. Hardt, M. Kupper, and F. Schonfeld, Aiche Journal, 50, 2297 (2004)

[44] R. L. Penn and J. F. Banfield, Science, 281, 969 (1998)

[45] D. Li, M. H. Nielsen, J. R. I. Lee, C. Frandsen, J. F. Banfield, and J. J. De Yoreo, Science, 336, 1014 (2012)

[46] S. T. Tan, B. J. Chen, X. W. Sun, W. J. Fan, H. S. Kwok, X. H. Zhang, and S. J. Chua, Journal of Applied Physics, 98, 013505 (2005)

[47] R. J. Tayade, P. K. Surolia, R. G. Kulkarni, and R. V. Jasra, Science and Technology of Advanced Materials, 8, 455 (2007)

Chapter 3. Controlled Solution Synthesis of ZnO Nanostructured Surfaces Using a Continuous Flow Microreactor

Changho Choi and Chih-hung Chang

Processed manuscript

In chapter 2, a continuous flow microreactor system was demonstrated to yield various assembled structures composed of stable colloidal ZnO nanocrystals. Morphology of assembled ZnO nanocrystals such as rectangular or large spherical structures was primarily determined by the flow rate of solution. The assembled ZnO structures were used as building blocks to prepare ZnO nanostructured surfaces by directly delivering the assembled structures towards substrates. It was found that the rectangular structures lead to flower like ZnO nanostructured surface while the spherical assembly results in amorphous ZnO thin film. Growth mechanism of the flower structure was investigated by varying process parameters such as reaction temperature, rotating speed of the substrates and deposition temperature. This study demonstrates the versatility of the continuous flow microreactor system in terms of fabricating various ZnO nanostructured surfaces by simply tuning the process parameters such as flow rate and substrate rotating speed.

3.1. Introduction

ZnO is a versatile material with many potential applications including light emitting diodes, field effect transistors, ultraviolet lasers, chemical sensors, and solar cells [1-5]. Since size and morphology of ZnO nanostructures play an

important role in determining physical properties, numerous efforts have been made to control the size and morphology. The conventional wet chemical approaches to synthesize ZnO nanocrystals typically include precipitation method, sol-gel processing, hydrothermal technique, and microemulsion processing. Advantages of the wet chemical approaches over the dry methods include lower capital cost, lower processing temperature, and easier scale-up. In the wet chemical approaches, solution conditions such as pH value, reaction temperature, and concentration of precursor can be varied led to synthesize various ZnO with different morphologies such as rod-like, prism, and flower like structures [6-8]. These beautiful structures were generally obtained under the hydrothermal conditions which normally require long reaction time period and high reaction temperature. The evolution of the structures is a result of the dissolution-crystallization mechanism during the aging process.

Microreactor-assisted nanomaterial synthesis and deposition process allow for the continuous synthesis and assembly of colloidal nanocrystals. This process offers several unique characteristics over the conventional wet chemical approaches. (1) The microreactor facilitate the homogenous nucleation of nanocrystals by creating an uniform and fast mixing of reactant while minimize pH and temperature gradient in the solution. (2) It enables the growth process of nanocrystals to be tailored by controlling system parameters such as reaction temperature and flow rate of the solution, leading to faster and more efficient preparation of nanocrystals4. (3) Lastly it enables the fabrication of nanofilms via direct delivery of colloidal nanocrystals and reactive molecules on targeted substrates.

In this chapter, we fabricated ZnO nanostructured surfaces using reactive molecules, colloidal ZnO nanocrystals and their assemblies as building blocks. The substrates were sitting on top of a temperature-controlled rotating disk. . By adjusting flow rate of solution, ZnO nanostructured surface with various morphologies were obtained, yielding flower structure or amorphous thin film. Growth of the flower structure was studied in more details to elucidate its growth mechanism. This study demonstrates that assembly of colloidal ZnO nanocrytals can be practically applied for the preparation of ZnO nanostructured surfaces. These nanostructured surfaces are being used in various applications including two-phase heat exchangers and thin film transistors.

3.2. Experimental

3.2.1. Fabrication of ZnO nanostructured surfaces

The facility to prepare ZnO nanocrystals consists of a microprocessor controlled dispensing pump (Ismatec), Tygon tubing (1.22 mm ID, Upchurch Scientific), and a micro T-mixer (Upchurch scientific). Zinc acetate ($Zn(CH_3COO)_2 \cdot 6H_2O$, Sigma Aldrich), ammonium acetate (CH_3COONH_4, Mallinckrodt Chemicals), and sodium hydroxide (NaOH, Mallinckrodt Chemicals) were used as received without further purification. Schematic diagram of the system is shown in Figure 3.1. Stream A (0.005 M $Zn(CH_3COO)_2 \cdot 6H_2O$ and 0.25 M CH_3COONH_4 solution) and stream B (NaOH for desired solution pH) were dissolved in water and initially pumped into the Tygon tubing. A micro-T mixer allowed homogeneous mixing of the reactants. Then, the mixture of the reactants passed through a helical reactor made by wrapping 1.3 m long Tygon tubing

around a cylinder. By immersing the reactor in an oil bath, the reaction temperature (70 ℃) was maintained throughout the growth process. Two different volume flow rates (14.7 and 28.1 mL/min) were adopted to obtain a certain assembled structure. The assembly of colloidal ZnO nanocrystals grown in the helical reactor was directly deposited on the SiO_2 substrate. The SiO_2 substrate was cleaned by using acetone, methanol, and deionized water followed by the drying using nitrogen gas. The substrate was then sonicated in 1 M NaOH solution before the deposition process. The substrate was placed on a rotating-disk equipped with an electrical heater to control the deposition temperature. Rotating speed was varied from 0 to 2000 rpm to study its influence on the formation of the nanostructured surface. The deposition temperature was also changed from room temperature to 200℃.

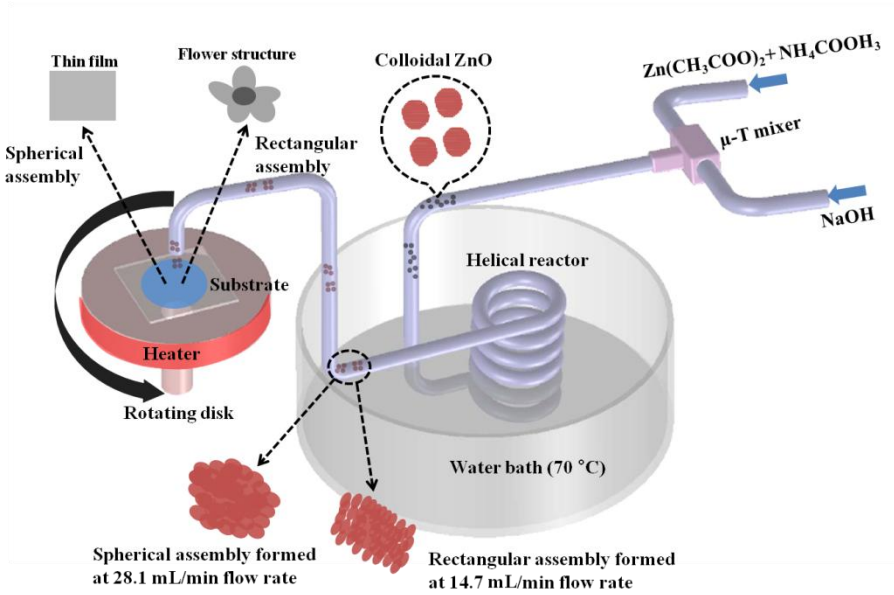

Figure 3.1. Scheme of the continuous flow microreactor system for the synthesis and deposition of ZnO nanostructured surfaces.

3.2.2. Characterization of ZnO nanocrystals and nanostructured surfaces

Size and morphology of ZnO nanocrystals were analyzed using high resolution transmission electron microscopy (HRTEM) and fast fourier transform (FFT) analysis. HRTEM images were taken by using a FEI Titan operated at 300 kV. For the HRTEM analysis, ZnO nanocrystals generated inside the reactor were directly delivered on a carbon coated copper grid (300 mesh, Tedpella). Several approaches of collecting ZnO nanocrystals on grids were tested to verify that the observed ZnO assembly under TEM is independent of TEM sample preparation method. We observed that evaporation of solvent did not affect the observed assemblies of ZnO nanocrystals. Morphologies of the nanostructured surfaces were examined by scanning electron microscopy (SEM, Quanta 600 FEG). Atomic force microscopy (AFM, Veeco) was applied to examine topography of the nanostructured surfaces. X-ray diffraction (XRD) was used to identify the crystallinity of the nanostructured surfaces. XRD data were obtained by using D8 Discover (Bruker) with a Cu *Kα* radiation (acceleration voltage: 40 kv, flux: 40 mA).

3.3. Results and Discussion

3.3.1. Formation of ZnO nanocrystal assembly in the continuous flow microreactor system

The speciation diagram of zinc precursors as a function of the solution pH was constructed and shown in Figure 3.2 by using a Visual Minteq software. Acidity of the solution was measured to be around pH=12.5. At pH=12.5, $Zn(OH)_3^-$ is the dominant precursor for the nucleation and growth of ZnO. The

growth mechanism and stability of colloidal ZnO nanocrystals in the continuous flow microreactor technique were described in our previous chapter.

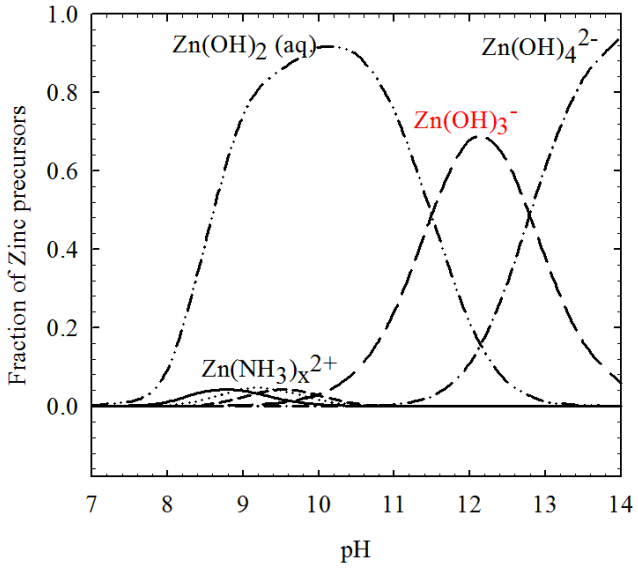

Figure 3.2. Speciation diagram of Zn precursors with respect to solution pH.

Figure 3.3 reveals ZnO nanocrystal assemblies formed at various solution flow rate. As observed in our previous work, colloidal ZnO nanocrystals coalesce with one another, leading to the assembled structures with a rectangular or spherical shape. The structure of the assembly depends on the magnitude of solution flow rate. The driving force to cause the assembly is a result of the competing interaction between Dean vortices and electrostatic forces. Dean vortices were created in the helical reactor due to the imbalance of centrifugal forces and viscous forces [10]. The characteristic of Dean vortices is the enhancement of solution mixing, which promotes the coalescence of colloidal ZnO nanocrystals. The magnitude of Dean vortices increases with an increase of solution flow rate [9]. The rectangular structures in Figure 3.3a possess various

length and width. The structure consists of a number of ZnO nanocrystals with random aggregation and shows polycrystalline as confirmed by a closer view of the structure and the FFT image. At a flow rate of 14.7 mL/min, the effect of Dean vortices is significant and competes with electrostatic forces (Dean vortices cause more coalescences between colloidal ZnO nanocrystals while electrostatic forces generate repulsive forces between colloidal nanocrystals). This competing interaction results in the formation of the rectangular ZnO assembly. At a higher flow rate (flow rate=28.1 mL/min), Dean vortices are more significant and dominate the electrostatic forces. Such strong Dean vortices prefer to create the spherical assembly. Likewise, the spherical structure is composed of colloidal ZnO nanocrystals with a surrounding amorphous ZnO matrix. This phenomenon is consistent with our earlier observations [9].

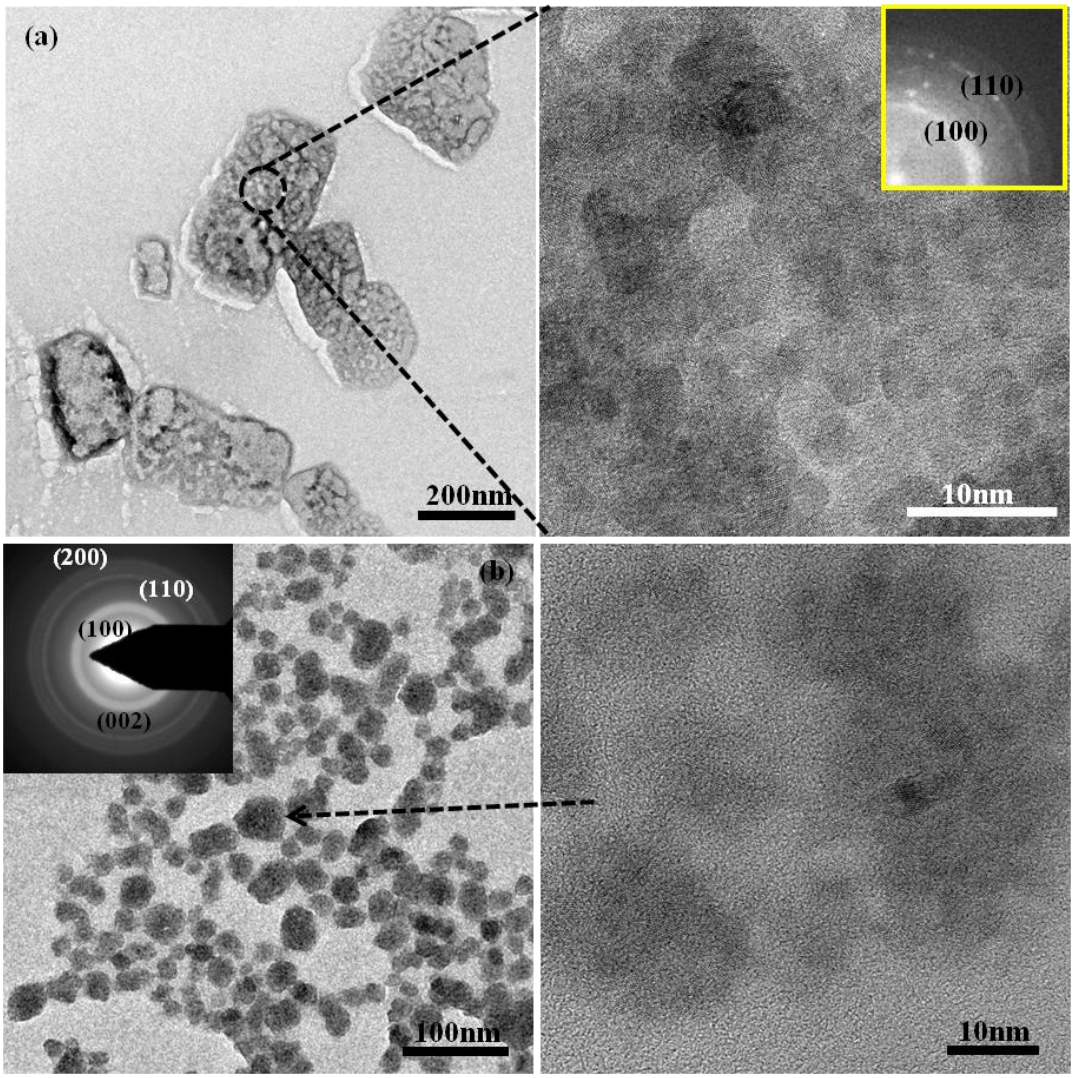

Figure 3.3. Assembly of colloidal ZnO nanocrystals synthesized at a flow rate of (a) 14. mL/min and (b) 28.1 mL/min.

We used ammonia as a complex agent to create colloidal ZnO nanocrystals. Although $Zn(NH_3)_x^{2+}$ precursors do not contribute to the formation of colloidal ZnO nanocrystals according to the speciation diagram, the role of ammonia on the ZnO nanocrystal assembly need to be considered. Adsorption of ammonia on ZnO nanocrystals has been intensively investigated due to the fact that ammonia plays an important role in controlling shape of ZnO nanocrystals. It was reported that ammonia selectively adsorb on ZnO crystal face [11-13]. Ammonia molecule, a

strong Lewis base, adsorbs preferentially at metal ion sites through the σ-type interaction between the N-localized 3a1 molecular orbital and the unoccupied orbitals on the metal ions [13]. A recent study using ATR-FTIR spectrum confirmed the role of ammonia adsorption on shape control of ZnO crystal. It was found that ammonia adsorbs much more strongly to the (100) surface than the (001) surface. However, ammonia molecule reversibly adsorbed on the surface and could be rinsed off [11]. In our study, we attempted to detect ammonia molecule bounded on the surface of colloidal ZnO nanocrystals by using FT-IR, TGA, DSC, and Mass Spectroscopy. However, none of these analytical techniques gave the evidence of ammonia present on the surface. We believe that ammonia molecule adsorbed on the surface was washed off during the purification process for the characterization. Because ammonia molecule selectively adsorbs on particular crystal face, the adsorption may affect the assembly of colloidal ZnO nanocrystals. The rectangular assembly differs from the tactoid structure formed in the absence of ammonia at the same flow rate (14.7 mL/min) [9]. We suspect this is due to the influence of the adsorption of ammonia on the ZnO nanocrystal surface. The effect of ammonia adsorption on the assembly is not pronounced at the solution flow rate of 28.1 mL/min since the spherical structure was also obtained in the absence of ammonia. This may result from the strong impact of Dean vortices in which Dean vortices overwhelm other influences.

3.3.2. Effects of solution flow rates on morphology of ZnO nanostructured surfaces

We fabricated ZnO nanostructured surfaces by directly delivering the ZnO nanocrystal assembly on the SiO_2 substrate secured on a rotating disk. Note the role of ammonia ligands in the adherence of the assembled ZnO structures on the substrate. In the absence of the ammonia ligands, the nanostructured surfaces were unable to be fabricated. Ammonia adsorbed on the surface of ZnO nanocrystals may play a role in binding ZnO assembly on the substrate covered with OH^- which is created by the substrate treatment with 1 M NaOH. Figure 3.4. exhibits flower ZnO nanostructured surface deposited on the substrate for 3 min. deposition period. Typical size of the flower is approximately 1.5 μm, and size of the flower is relatively uniform with dispersed deposition pattern. The shape of the flower structure is distinct from those reported in the literature. Most of flower ZnO structures grown in conventional methods such as precipitation or hydrothermal reaction were formed via fourlings having four acicular spines combined at a common base [14]. On the other hand, the flower structure formed through the continuous flow microreactor system seems to be prepared in the way that many petals piled up to form the flower structure. This difference indicates that the flower structure by the continuous microreactor system was formed via a different growth mechanism from what was commonly observed in the literature [8, 15]. The rectangular ZnO assembly synthesized in the continuous microreactor system served as the building blocks for formation of the flower structure or at least contribute to the formation of the seed layer on which subsequent growth of the flower structure occurred with the molecular precursors, $Zn(OH)_3^-$.

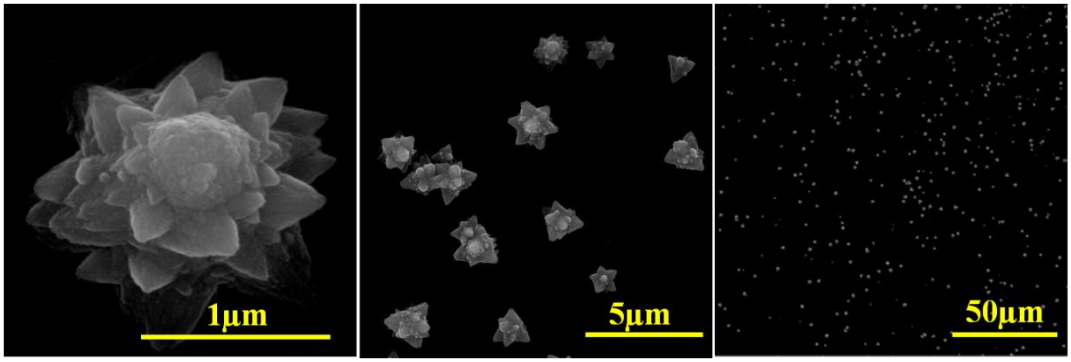

Figure 3.4. Flower ZnO nanostructured surface prepared in 14.7 mL/min flow rate.

XRD pattern of the flower structure is shown in Figure 3.5. Although the peak intensity of ZnO flower structure is low, three peaks matched well with the standard wurtzite structure (JCPDS Card No. 36-1451). The low intensity may be associated with the growth mechanism of the flower structure in which the rectangular assembly randomly aggregated was continuously served as the building unit for growth of the flower structure. ZnO flower structures reported in literature usually experienced the Oswald ripening (OR) during the aging process. In the OR mechanism, flower structures were grown by attachment of molecular precursors, which leads to a higher crystallinity of ZnO flower structures.

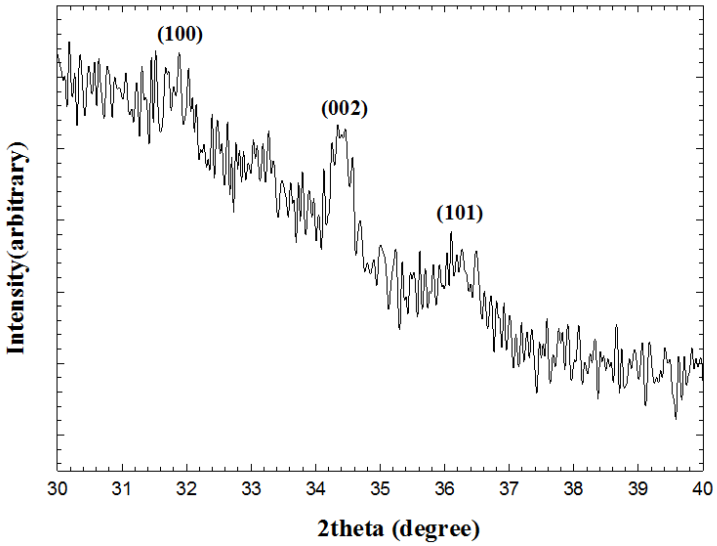

Figure 3.5. XRD pattern of ZnO flower structure.

We deposited the spherical assembly generated from the flow rate of 28.1 mL/min to compare the morphology of the nanostructured surface prepared by using a flow rate of 14.7 mL/min. Except for the flow rate of solution, other process parameters were kept identical. Morphology of the nanostructured surface prepared using the spherical assembly is examined by SEM, HRTEM, and AFM (Figure 3.6). In contrary to the ZnO flower structure, the high flow rate gave rise to a smooth surface according to the AFM analysis. HRTEM image of the ZnO thin film shows that the ZnO layer with 15 nm thick can be obtained for 3 min deposition period. Thickness of the thin layer can be controlled by varying the deposition period. The ZnO layer has an amorphous phase according to the FFT image and the XRD data.

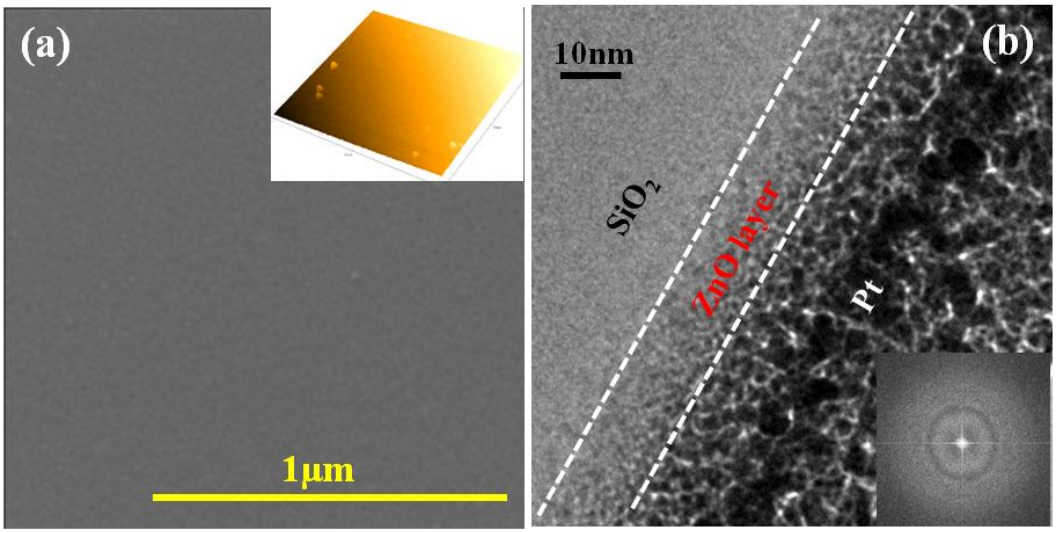

Figure 3.6. Amorphous ZnO thin film prepared in 28.1 mL/min flow rate: (a) SEM image with AFM (inset) and (b) HRTEM image with FFT (inset).

Optical band gap of the thin film, measured after 500 ℃ thermal treatment, is about 3.3 eV. (Figure 3.7).

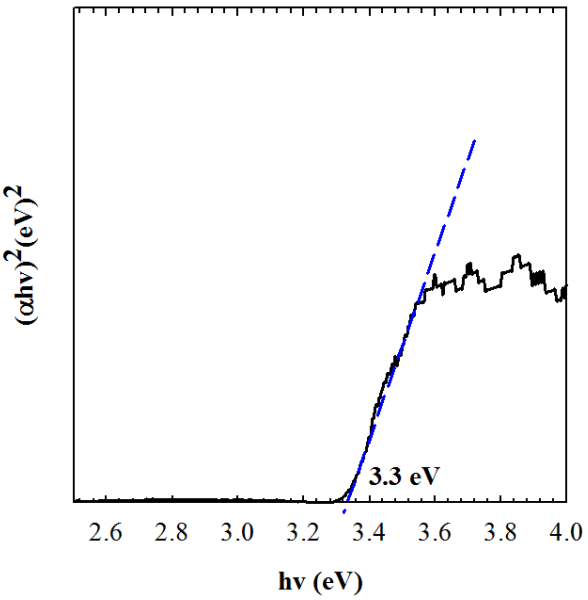

Figure 3.7. Optical band gap of the amorphous ZnO thin film after 500^{o}C thermal treatment.

Figure 3.1. illustrates the process of the continuous flow microreactor system dictating from the synthesis of colloidal ZnO assembly to the fabrication of nanostructured surfaces. ZnO nuclei or colloidal ZnO nanocrsytal were formed after mixing of reactants. These colloidal ZnO nanocrystals were assembled to rectangular or spherical structure, depending on the magnitude of solution flow rate when nanocrystals flowed in the helical reactor. ZnO assembly was deposited onto the substrate and served as building blocks for the fabrication of ZnO nanostructured surfaces. The rectangular assembly led to flower ZnO nanostructured surface while ZnO thin film was fabricated from the solution containing spherical assembly. A conventional batch process for the preparation of ZnO surface was also performed to compare ZnO morphology from the batch process with those prepared by the continuous flow microreactor system. For the ZnO growth using a conventional batch process, 0.005 M zinc acetate ($Zn(CH_3COO)_2 \cdot 6H_2O$, Sigma Aldrich), 0.25 M ammonium acetate (CH_3COONH_4, Mallinckrodt Chemicals), and 0.1 M sodium hydroxide (NaOH, Mallinckrodt Chemicals) were mixed and placed in a teflon reactor supplied from a autoclave. A bare SiO_2 substrate used for the continuous flow microreactor system was placed in the teflon reactor. The autoclave was placed for 2hrs in an oven heated to 70 ℃. After the growth completion, ZnO nanostructure on the substrate was cleaned using D.I. water, but all nanostructured were washed off. ZnO powders were taken for the SEM analysis. Heterogeneous growth did not take place in the batch process, but instead homogeneous growth occurred and precipitated. The batch process only produced flower structure with a broader size distribution and did not present thin film formation (Figure 3.8).

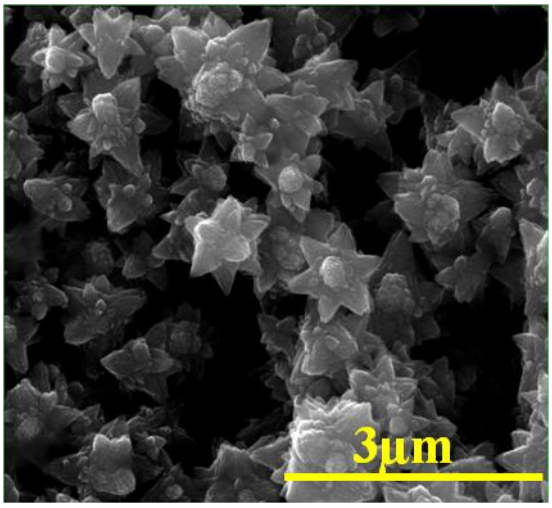

Figure 3.8. ZnO flower structure grown by the batch process.

3.3.3. Growth study of ZnO flower structure

There are several process parameters that affect the growth of the flower structure, including revolutions per minute (RPM) of the rotating disk, deposition period, and deposition temperature. In order to study the formation of the flower structure onto the substrate using the rectangular assembly, each process condition was varied while fixing other parameters. A summary of all process conditions for the preparation of the flower surface is given in Table 3.1.

Table 3.1. Summary of process conditions for the flower structure

Sample No.(#)	Flow rate(ml/min)	Reaction temperature (°C)	Deposition temperature (°C)	RPM	Deposition period(min)
1	14.7	70	50	1500	3
2	14.7	70	100	1500	3
3	14.7	70	150	1500	3
4	14.7	70	200	1500	3
5	14.7	70	250	1500	3
6	14.7	70	200	500	3
7	14.7	70	200	1000	3
8	14.7	70	200	1500	3
9	14.7	70	200	2000	3
10	14.7	70	200	0	3
11	14.7	Room temperature	50	0	3
12	14.7	Room temperature	100	0	3
13	14.7	Room temperature	200	0	3

Figure 3.9 shows single ZnO flower structure prepared at various deposition temperatures. As the deposition temperatures increases, the size of ZnO flower structure becomes larger having more petals. The flower structure deposited at 50 ℃ is about 1 µm and became almost double to 2 µm at 250 ℃ deposition temperature. As mentioned in the previous section, the rectangular assembly provides building blocks for the growth of the flower structure, being served as seed layer. Molecular Zn precursors then adsorbed on the seed layer for the subsequent growth of the flower structure. Both the assembly and molecular precursors are more prone to form the flower structure at high deposition temperature due to sufficient thermal energy required for binding them onto the substrate [16].

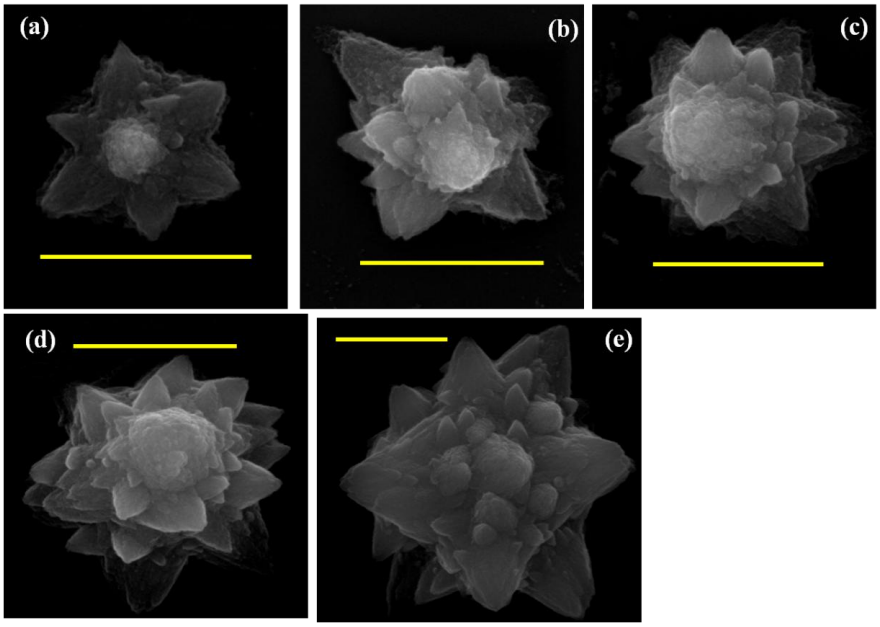

Figure 3.9. SEM images of the flower structure prepared at various deposition temperature: (a) 50 ℃, (b) 100 ℃, (c) 150 ℃, (d) 200 ℃, and (e) 250 ℃ (scale bar = 1µm).

XRD data in Figure 3.10 (a, b) indicate that crystallinity of the structures is improved with the increase of deposition temperature although the overall crystallinity is still low.

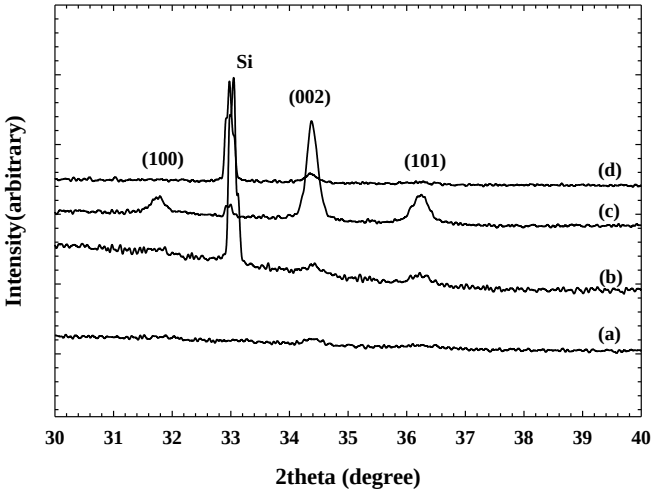

Figure 3.10. XRD patterns of the flower structures prepared at various process conditions: (a), (b), (c), and (d) corresponding to the sample no. 4, 5, 10, and 13, respectively.

Effect of the deposition temperature on density of the structure seems to be insignificant according to the SEM images in Figure 3.11. The number of the flower structure seems to be similar regardless of the deposition temperature.

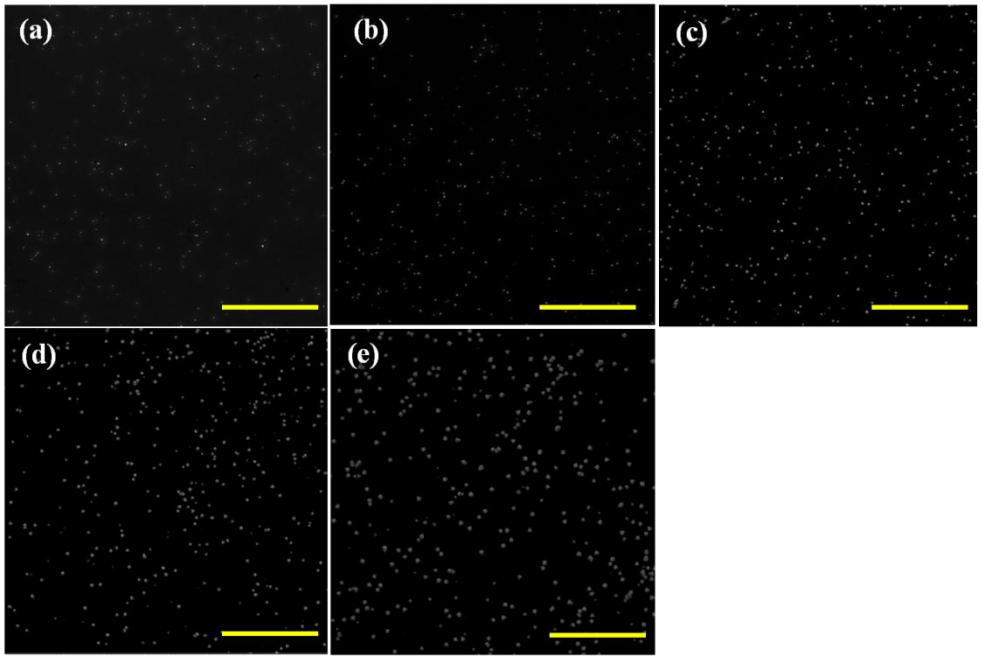

Figure 3.11. Low magnification SEM images of the flower structure grown at various deposition temperature: (a) 50 ℃, (b) 100 ℃, (c) 150 ℃, (d) 200 ℃, and (e) 250 ℃ (scale bar = 50 μm).

HRTEM image of a typical flower structure is shown in Figure 3.12. The structure is a single crystal phase according to the lattice fringe and FFT image (inset).

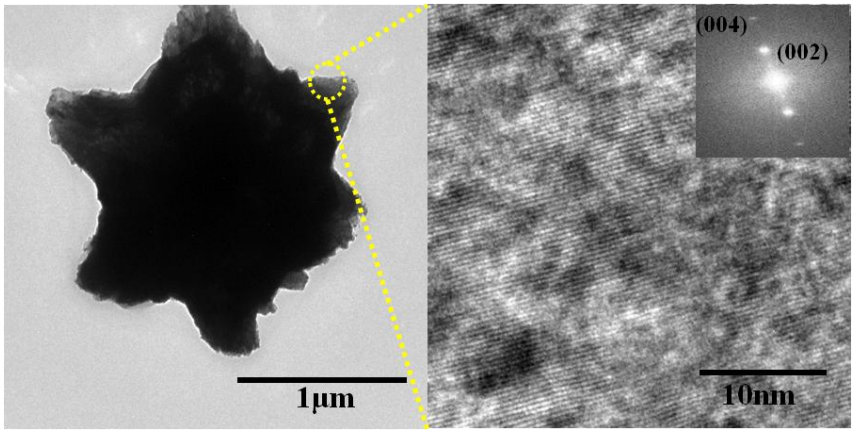

Figure 3.12. HRTEM and FFT image (inset) of a typical flower structure.

The effect of the rotating speed was studied by changing the rpm of the rotating disk. The effect of the rotating speed appears to be insignificant in terms of the morphology of flower (Figure 3.13). The size and morphology of the flower-like structure are very similar regardless of the magnitude of the rotating speed. However, the number of the flower structure increased as the rpm decreased (Figure 3. 14). The XRD intensity also increase at lower rotating speed (Figure 3.10 c). The densest structure was obtained at 0 rpm condition. The absence of the rpm may help the flower structure grow denser by the heterogeneous reaction. A thermodynamic expression regarding the nucleation of nanocrystals was proposed as follow

$$\Delta G_T = -n\Delta\mu + 4\pi r^2\sigma$$

where ΔG_T, n, $\Delta\mu$, r, σ denotes the free energy difference between solution and nucleus status, the number of molecule to form a nucleus, chemical potential difference, radius of a nucleus, and interface energy between nucleus and solution respectively. It has been generally known that the heterogeneous reaction is more favorable compared to the homogeneous reaction in the presence of substrate due to the lower interface energy (σ) [17]. Kinetic study on nucleation of nanocrystals was also performed and expressed as follow

$$J = J_0 \exp\left(\frac{-\Delta G_N}{kT}\right)$$

where J, J_0, ΔG_N, k, T denotes the number of nuclei, the frequency of collisions between precursor molecules, nucleation activation energy difference, Boltzmann constant, and reaction temperature respectively. The number of nuclei is as a function of reaction temperature. As the reaction temperature increases, more

nuclei are created, leading to larger flower structure at high deposition temperature (Figure 3.9).

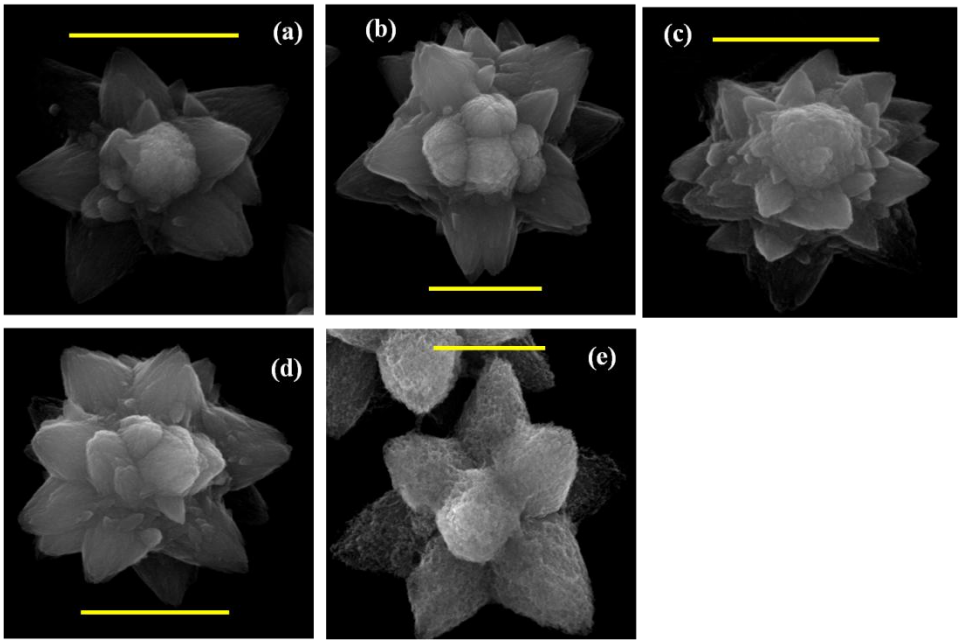

Figure 3.13. SEM images of flower structure grown in (a) 500 rpm, (b) 1000 rpm, (c) 1500 rpm, (d) 2000 rpm, and (e) 0 rpm.

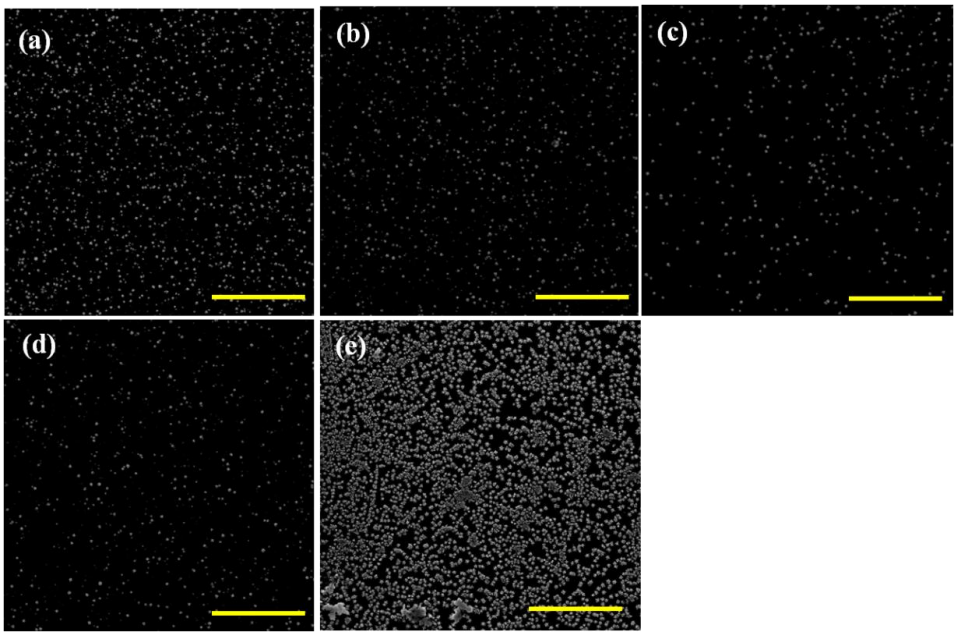

Figure 3.14. Low resolution SEM images of the flower structure grown in (a) 500 rpm, (b) 1000 rpm, (c) 1500 rpm, (d) 2000 rpm, and (e) 0 rpm.

For further growth study of the flower structure, we adopted various process conditions while giving no rotation. Figure 3.15 (a-c) displays the flower structure prepared in the absence of the rectangular assembly. It was found that colloidal ZnO nanocrystals do not form at room temperature reaction condition due to the low hydrolysis ratio of the Zn precursors in which supersaturation condition does not occur. In the absence of colloidal ZnO nanocrystals, the molecular precursors were available for the growth of the flower structure. The effect of the deposition temperature is pronounced since size and density of the flower structure are increased with an increased deposition temperature. The room temperature deposition condition did not provide the rectangular assembly, the seed layer, in which heterogeneous growth took place in limited sites. However, as the deposition temperature increased, more nuclei and nucleation sites were created, making dense and large flower structure. However, as described in the previous section, the shape of the flower structure grown in the absence of the rectangular assembly is obviously different from one prepared in the presence of the assembly. XRD data of flower structure grown in free of the assembly is also shown in Figure 3.10 d.

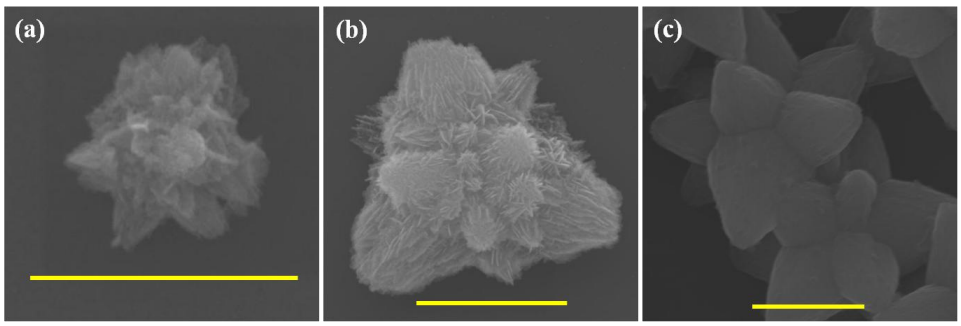

Figure 3.15. SEM images of the flower structure: (a), (b), and (c) corresponding to sample no. 11, 12, and 13 respectively (scale bar = 1 µm).

3.4. Conclusion

We have demonstrated that colloidal ZnO assembly formed in the microreactor can be used as building blocks for the fabrication of the ZnO nanostructured surfaces. Two different types of the ZnO assemblies were prepared by changing the solution flow rate. These ZnO assemblies were directly deposited on the substrate to prepare the nanostructured surfaces. The structure of the assembly determined the morphology of the nanostructured surfaces, forming the flower structure or amorphous thin film. The deposition conditions were varied to study the effect of process parameters on the growth of the flower structure. It was hypothesized that ZnO assembly acts as the seed layer for the subsequent growth of the flower structure. Heterogeneous growth on the seed layer continuously occurred for the growth of the flower structure. This study shows the unique characteristic of the continuous flow microreactor system in terms of fabricating various nanostructure morphologies by simply tuning the flow rate of solution. Furthermore, various colloidal metal oxide nanocrystals can be formed in the continuous flow microreactor system and used as the building blocks for the preparation of nanostructured surfaces which can be applied to various research areas.

3.5. References

[1] J. Bao, M. A. Zimmler, F. Capasso, X. Wang, and Z. F. Ren, Nano Letters, 6, 1719 (2006)

[2] B. Sun and H. Sirringhaus, Nano Letters, 5, 2408 (2005)

[3] S. Hirano, N. Takeuchi, S. Shimada, K. Masuya, K. Ibe, H. Tsunakawa, and M. Kuwabara, Journal of Applied Physics, 98, 094305 (2005)..

[4] J. H. Xiang, P. X. Zhu, Y. Masuda, M. Okuya, S. Kaneko, and K. Koumoto, Journal of Nanoscience and Nanotechnology, 6, 1797 (2006)

[5] A. Umar, M. M. Rahman, S. H. Kim and Y.-B. Hahn, Chemical Communications, 2008, 166 (2008)

[6] B. Weintraub, Z. Zhou, Y. Li and Y. Deng, Nanoscale, 2, 1573 (2010)

[7] J. Zhang, L. D. Sun, J. L. Yin, H. L. Su, C. S. Liao, and C. H. Yan, Chemistry of Materials, 14, 4172 (2002)

[8] Y. Zhang and J. Mu, Nanotechnology, 18, 075606 (2007)

[9] C. Choi and C.-h. Chang, Crystal Engineering Communication, accepted manuscript (2013)

[10] S. Kim and S. J. Lee, Experiments in Fluids, 46, 255 (2009)

[11] N. J. Nicholas, G. V. Franks, and W. A. Ducker, Langmuir, 28, 7189 (2012)

[12] J. Y. Lin, P. M. Jones, M. D. Lowery, R. R. Gay, S. L. Cohen, and E. I. Solomon, Inorganic Chemistry, 31, 686 (1992)

[13] K. Ozawa, T. Hasegawa, K. Edamoto, K. Takahashi, and M. Kamada, Journal of Physical Chemistry B, 106, 9380 (2002)

[14] R. A. McBride, J. M. Kelly, and D. E. McCormack, Journal of Materials Chemistry, 13, 1196 (2003)

[15] R. Wahab, S. G. Ansari, Y. S. Kim, H. K. Seo, G. S. Kim, G. Khang, and H.-S. Shin, Materials Research Bulletin, 42, 1640 (2007)

[16] D. L. Schulz, M. Pehnt, D. H. Rose, E. Urgiles, A. F. Cahill, D. W. Niles, K. M. Jones, R. J. Ellingson, C. J. Curtis, and D. S. Ginley, Chemistry of Materials, 9, 889 (1997)

[17] J.-P. Jolivet, Metal Oxide Chemistry and Synthesis from solution to solid state, John Wiley & Sons Ltd, Baffins Lane, Chichester, West Sussex, 2000

Chapter 4. Controlled Growth of Vertical ZnO Nanowire Arrays Using a Continuous Flow Microreactor

Changho Choi and Chih-hung Chang

Processed manuscript

Various synthetic approaches for growing ZnO nanowires (NWs) have been proposed due to wide applications of ZnO NWs. A hydrothermal process was considered one of most efficient approaches to prepare vertical ZnO NW arrays. In this study, we reported a novel synthetic route for the growth of vertical ZnO NW arrays. The continuous flow microreactor system was employed to grow vertical ZnO NW arrays. Colloidal ZnO nanocrystal assembly synthesized in the continuous flow microreactor system were used for the formation of ZnO seed layer. ZnO NW arrays were also prepared by using the continuous flow microreactor system as well. Various characterization methods were performed to study the growth mechanism of vertical ZnO NW arrays. System parameters were varied to tune the aspect ratios of vertical ZnO NW arrays. The growth rate of ZnO NW arrays was estimated based on the height variation of ZnO NW arrays with respect to the deposition time. A growth rate of 88 mL/min was achieved via this route. This deposition rate is the highest value compared with those reported previously in the literature. This result demonstrates the efficiency of the continuous flow microreactor systm in terms of fabricating vertical ZnO NW arrays.

4.1. Introduction

One-dimensional ZnO nanostructure has gained significant attraction due to its possible quantum confinement effect [1]. Potential applications of ZnO nanowires (NWs) include light-emitting diodes, lasers, field effect transistors, chemical sensors, and solar cells [2-6]. Various approaches have been reported for the growth of ZnO NWs in solution. Among these approaches, the hydrothermal process has been widely used due to its good energy efficiency and the ease of implementation [7].

In most case of the hydrothermal synthesis of ZnO NWs, hexamine ($C_6H_{12}N_4$) was employed to control the growth rate of ZnO NWs as a pH buffer through thermal decomposition [8]. ZnO has a hexagonal unit cell with six nonpolar (10-10) prismatic planes, polar oxygen (000-1), and polar zinc basal plane (0001). A recent investigation reported that hexamine selectively attaches on the nonpolar prismatic planes, acting as a chelating agent. This chelating effect inhibits growth of the nonpolar planes and causes a preferential growth along the [0001] direction, resulting in the formation of ZnO NW [9]. Another approach to control the aspect ratios of ZnO NWs in the hydrothermal reaction is associated with the control of growth parameters such as reaction temperature, concentration of precursors, and pH value of solution. It was also reported that additives are also efficient in controlling the aspect ratios of ZnO NWs [10].

ZnO seed layer is required to obtain vertical ZnO NW arrays, and effects of the seed layer on the growth of ZnO NW arrays have been intensively investigated. Various approaches to prepare ZnO seed layers have been reported [11-13].

We have synthesized colloidal ZnO nanocrystals and their assembly in the aqueous medium using the continuous flow microreactor system. The characteristics of the continuous flow microreactor system were described in the previous chapters. The growth mechanism and stability of colloidal ZnO nanocrystals in the system were studied [14]. The fabrication of nanostrucutred surfaces using assembly of colloidal ZnO nanocrystals was also demonstrated in the previous chapter. In this chapter, we reported a successful preparationof vertical ZnO NW arrays on the SiO_2 substrate using the continuous flow microreactor system. We found several advantages of using the continuous flow microreactor system over the batch hydrothermal process in terms of the preparation of vertical ZnO NW arrays. (1) The aspect ratios of ZnO NWs can be easily controlled by varying deposition period in the absence of hexamine. (2) ZnO NWs can be grown very rapidly with very high growth rates. (3) ZnO seed layer can be prepared using the continuous flow microreactor system without changing chemical precursors. (4) The growth of ZnO NW arrays is not affected by the consumption of precursors since the precursors are continuously supplied for the growth of ZnO NW arrays. (5) The continuous flow microreactor system is capable of growing vertical ZnO NW array on large substrate. Herein, we study the growth mechanism of vertical ZnO NW array on the SiO_2 substrate and tune the aspect ratios of vertical ZnO NW arrays by changing growth parameters.

4.2. Experimental

4.2.1. Fabrication of ZnO seed layer and NW array

The continuous flow microreactor system to prepare ZnO NW arrays and the seed layer consists of a peristaltic pump (Ismatec), Tygon tubing (1.22 mm ID, Upchurch Scientific), and a micro-T-mixer (0.5 mm, Upchurch scientific). Zinc acetate ($Zn(CH_3COO)_2 \cdot 6H_2O$, Sigma Aldrich), ammonium acetate (CH_3COONH_4, Mallinckrodt Chemicals), and sodium hydroxide (NaOH, Mallinckrodt Chemicals) were used as received without further purification. A schematic diagram of the system is shown in Figure 4.1. Stream A (0.005 M $Zn(NO_3)_2 \cdot 6H_2O$ and 0.25 M CH_3COONH_4 solution) and stream B (NaOH for desired solution pH) were dissolved in water and initially pumped into the Tygon tubing. A micro-T-mixer allowed the homogeneous mixing of the reactants. Then, the mixture of the reactants passed through a helical reactor made by wrapping 1.3 m long Tygon tubing around a cylinder. By immersing the reactor in an oil bath, the reaction temperature (70 ℃) was maintained throughout the growth process. Colloidal ZnO nanocrystals were formed in the reactor and deposited onto the SiO_2 substrate. The SiO_2 substrate was vigorously cleaned by using acetone, methanol, and deionized water followed by the drying with nitrogen gas. The substrate was then sonicated in 1 M NaOH solution before the deposition process. For the uniform seed layer formation, we employed a rotating disk equipped with an electrical heater to fcontrol the deposition temperature. Flow rate of the solution for the seed layer formation was about 28.1 mL/min. The deposition temperature was maintained at 200 ℃ throughout the formation of the seed layer. For the ZnO NW array formation, we replaced the rotating disk with a heating block and directly deliver colloidal ZnO nanocrystals onto the ZnO seed layer. The heating block was also equipped with electrical heaters for the control of deposition temperature. Flow

rate of the solution for the growth of ZnO NW arrays was about 6.8 mL/min. The deposition temperature was maintained at 200 ℃ throughout the growth of ZnO NW arrays.

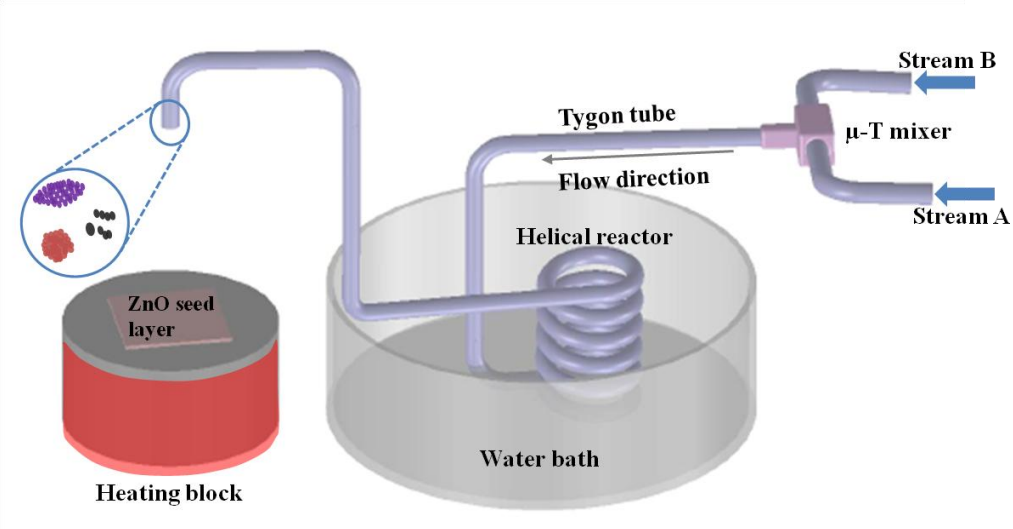

Figure 4.1. Scheme of the continuous flow microreactor system for the growth of vertical ZnO NW arrays.

4.2.2. Characterization of colloidal ZnO nanocrysals, seed layer, and NW arrays

Size and morphology of colloidal ZnO nanocrystals synthesized by the continuous flow microreactor system were analyzed using high resolution transmission electron microscopy (HRTEM) and fast fourier transform (FFT) analysis. HRTEM images were taken by using a FEI Titan operated at 300 kV. For the HRTEM analysis, colloidal ZnO nanocrystals were directly delivered on carbon coated copper grid (300 mesh, Tedpella). Focus ion beam (FIB) was employed to prepare TEM smaples of ZnO seed layer and ZnO NW arrays for HRTEM and FFT analysis. Morphology of the ZnO seed layer and ZnO NW arrays were examined

through scanning electron microscop (SEM, Quanta 600 FEG). Topography of the ZnO seed layer was examined by atomic force microscopy (AFM, Veeco). X-ray diffraction (XRD) was used to determine crystallinity of the seed layer and growth orientation of ZnO NW arrays. XRD data was obtained by using D8 Discover (Bruker) with a Cu Kα radiation (acceleration voltage: 40kv, flux: 40mA).

4.3. Results and Discussion

The basic process to create colloidal ZnO nanocrsytals for the growth of ZnO NW arrays was already described in the previous chapter. ZnO seed layer and NW arrays could be prepared by changing the process parameters. For the preparation of the ZnO seed layer, the process used to create the ZnO amorphous thin film was adopted (Chapter 3.3.2). It has been generally known that ZnO seed layer plays an important role in determining the aspect ratios of ZnO NW arrays. Effects of thickness and grain size of ZnO seed layer have been investigated and found to influence the diameter and length of ZnO NWs [12, 15-17]. ZnO seed layer generally consists of ZnO crystals having dominant (002) crystal plane. ZnO NW arrays are epitaxially grown onto ZnO nuclei of crystal seed layers. In our process, however, the as-deposited ZnO seed layer having amorphous phase was used as the template for the growth of ZnO NW arrays without further post-treatment.

For the growth of vertical ZnO NW arrays on the amorphous ZnO seed layer, we replaced the rotating disk with a stagnant heating block to avoid the rotation. It was found that effects of the angular momentum on the growth of ZnO NW arrays are quite significant. Vertical ZnO NW arrays can be fabricated only in

the absence of rotation. Pyramidal structure was prepared under the influence of the rotation. This result indicates that rotation can influence the growth of ZnO NWs. Further study is required to better understand the formation of the pyramidal structure under the effect of rotation. Flow rate of the solution was also adjusted to prepare vertical ZnO NW arrays. Figure 4.2 exhibits colloidal ZnO nanocrystals synthesized at a flow rate of 6.8 mL/min. In contrary to those synthesized at a flow rate of 28.1 mL/min (Figure 3.6), Colloidal ZnO nanocrsytals, building blocks of ZnO NW arrays, did not aggregate to form larger clusters. This is related to the interaction between Dean vortices and electrostatic forces. At a low flow rate, the Dean vortices is relatively insignificant so the electrostatic force dominates. Colloidal ZnO nanocrystals in the solution are stable without forming random aggregation under high electrostatic forces. Colloidal ZnO nanocrystals show a spherical shape that is around 5 nm in diameter. The typical colloidal ZnO nanocrystal was characterized using HRTEM and found to be single crystal. These colloidal ZnO nanocrystals were continuously delivered onto the amorphous ZnO seed layer and attributed to the formation of vertical ZnO NW arrays.

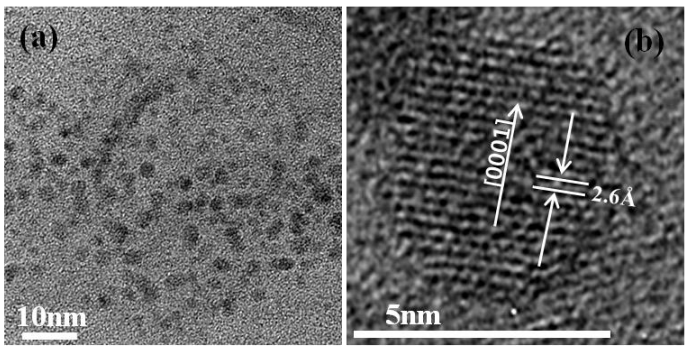

Figure 4.2. HRTEM images of colloiodal ZnO nanocrystals synthesized at solution flow rate of 6.8 mL/min: (a) low magnification and (b) a typical colloidal ZnO nanocrystal.

In order to study the growth mechanism of ZnO NW arrays on the amorphous ZnO seed layer, FIB was employed to prepare samples, which allows for the observation of interface between the seed layer and ZnO NW arrays through the HRTEM. Figure 2.3 displays schematic diagram of vertical ZnO NW grown on the amorphous ZnO seed layer and HRTEM images of distinct regime of ZnO NW arrays. We found that ZnO NW arrays can be divided into three different regimes in terms of the crystallinity. An interface can be clearly observed in Figure 2.3a, separating two layers, the amorphous ZnO seed layer and polycrystal ZnO layer. The ZnO seed layer was closely examined through the HRTEM and FFT images and confirmed to have the amorphous ZnO phase as previously described (Figure 2.3b). Figure 2.3c indicates that polycrystalline ZnO was formed on the amorphous ZnO seed layer prior to forming ZnO NW array. The formation of polycrystalline ZnO layer is attributed to colloidal ZnO nanocrystals prepared in the continuous flow microreactor system. ZnO NW arrays then begin to grow on polycrystalline ZnO layer showing single crystal nature according to HRTEM and FFT images (Figure 2.3d). It was found the amorphous ZnO seed layer is necessary to prepare vertical ZnO NW arrays although ZnO NWs do not directly grow on the amorphous ZnO seed layer. In the absence of the amorphous seed layer, only flower-like structure could be formed on the substrate. The growth of ZnO NW arrays on the crystalline ZnO layer verifies the epitaxial growth of vertical ZnO NW arrays. We attempted to grow ZnO NW arrays on the amorphous seed layer using colloidal ZnO nanocrystals prepared in high flow rates of the solution (14.7 mL/min). ZnO NW array did not form in the high solution flow rate where colloidal ZnO nanocrystals aggregated forming rectangular assembly. This result

indicates that proper flow rate of the solution should be applied in order to avoid the random aggregation of colloidal ZnO nanocrystals for the growth of ZnO NW arrays. For the summary of ZnO NW array formation, single colloidal ZnO nanocrystals should be delivered on the amorphous ZnO seed layer to form polycrystal ZnO layer, and then ZnO NW arrays grow on the polycrystal ZnO layer through the subsequent bonding of single colloidal ZnO nanocrystal.

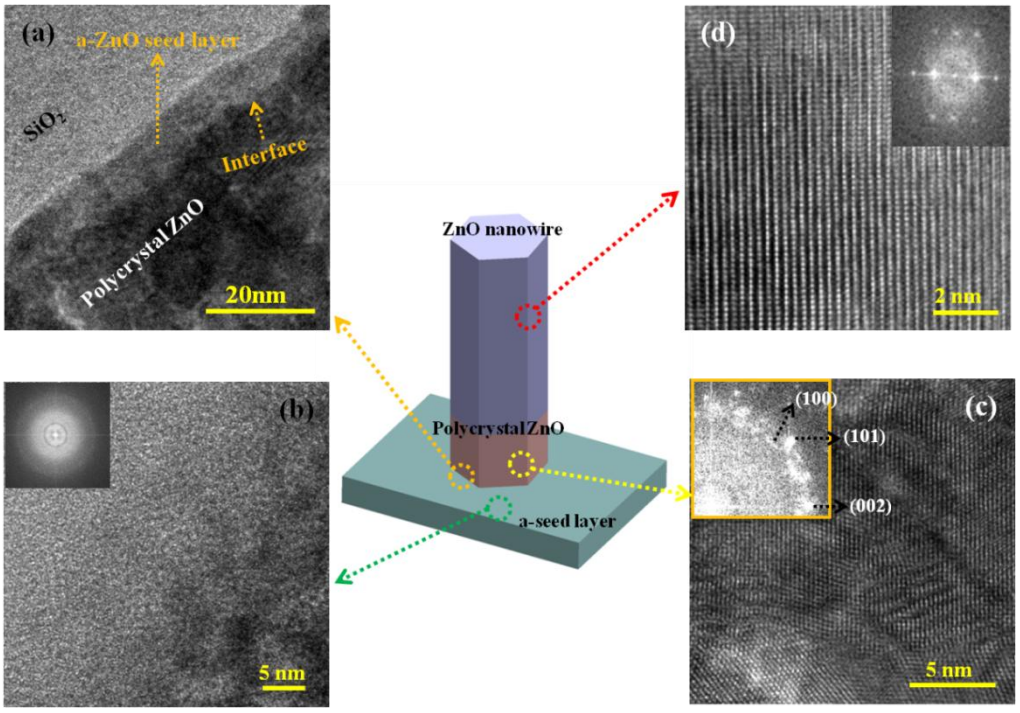

Figure 4.3. HRTEM images of the seed layer and ZnO NW: (a) interface between the seed layer and polycrystal ZnO layer, (b) amorphous ZnO seed layer, (c) polycrystal ZnO layer, and (d) ZnO NW.

SEM image and the corresponding XRD data of vertical ZnO NW arrays are shown in Figure 4.4. Pure ZnO NWs were grown vertically on the SiO_2 substrate, exhibiting very strong peak of (002) plane compared to other planes.

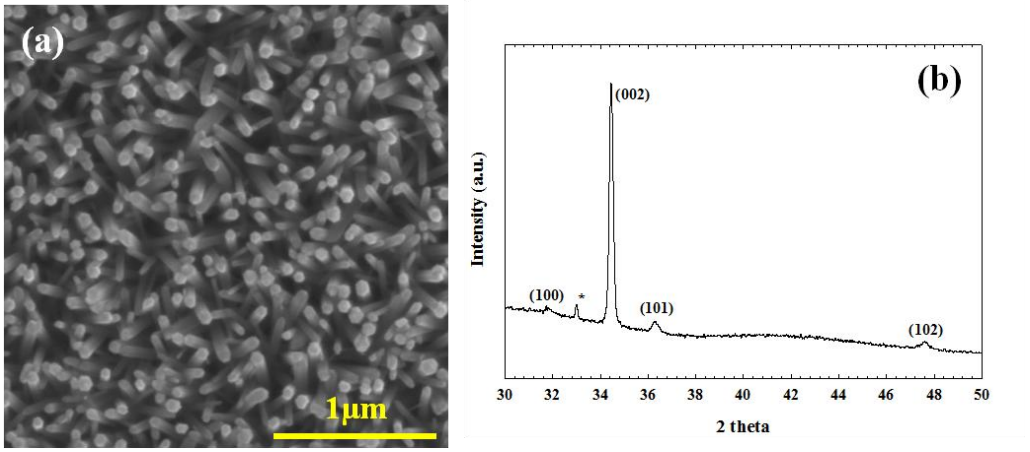

Figure 4.4. Characterization of vertical ZnO NW arrays: (a) top-down view of SEM image and (b) corresponding XRD data (*substrate).

Deposition period for the growth of vertical ZnO NW arrays and thickness of the amorphous ZnO seed layer were varied to study their effects on the formation of vertical ZnO NW arrays. Various deposition periods ranging from 20 sec. to 5min. were employed to control the thickness of the amorphous ZnO seed layer. The dimension of ZnO NW arrays was also tuned by changing ZnO NW deposition period. Figure 4.5 displays SEM images of single ZnO NW prepared at various growth conditions. Regardless of growth conditions, ZnO NW shows hexagonal feature. It was found that the aspect ratios of ZnO NW are more affected by ZnO NW deposition period than thickness of the amorphous ZnO seed layer. The diameter of ZnO NWs does not increase significantly with the increased thickness of the amorphous ZnO seed layer. On the other hand, the diameter of ZnO NWs increased significantly with the increase of ZnO NW deposition period. As the deposition period was changed from 1 min. to 20 min., the diameter of ZnO NWs increased from about 50 nm to 120 nm. This result indicates the role of the amorphous ZnO seed layer in the formation of vertical ZnO NW arrays. The role

of the amorphous ZnO seed is confined to bring out the polycrystal ZnO layer, incapable of controlling the aspect ratios of ZnO NW arrays. This trend is somewhat contrary to the results of previous studies accomplished by other researchers. However, they used crystal ZnO seed layer and demonstrated the importance of crystal ZnO seed in adjusting the aspect ratios of ZnO NW arrays, whereas herein the amorphous ZnO seed layer was applied to the growth of our ZnO NW arrays [12, 16].

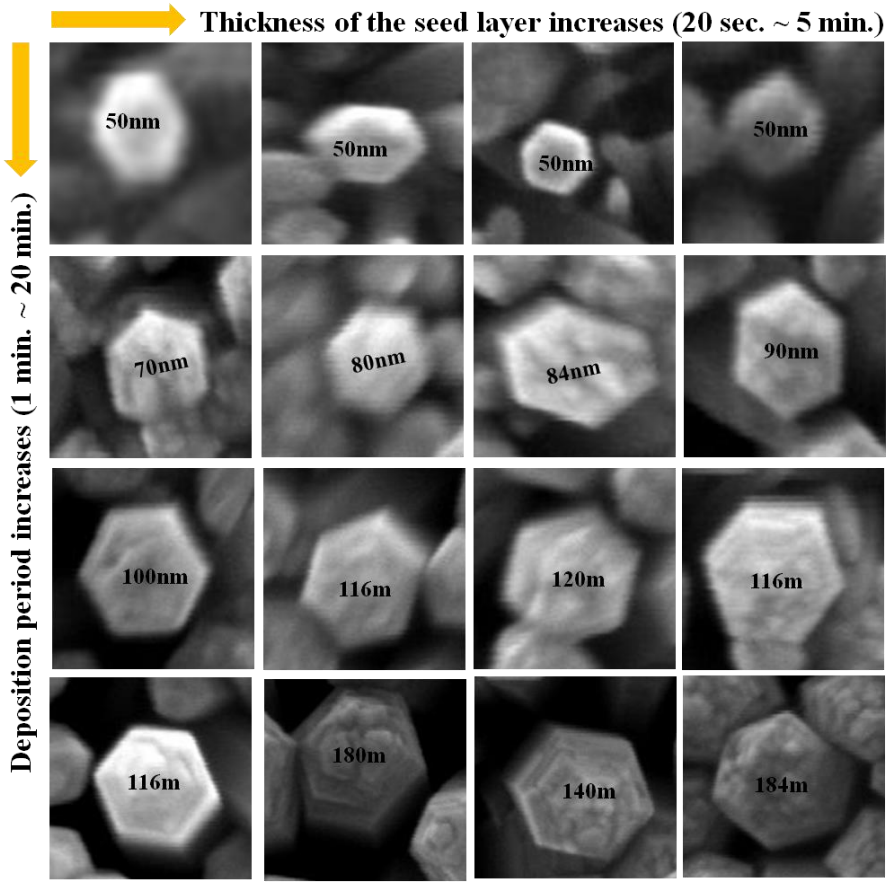

Figure 4.5. SEM images of ZnO NW arrays prepared in various growth conditions.

We may be able to propose the growth mechanism of ZnO NW arrays from the fact that the ZnO NW deposition period plays a significant role in controlling the diameter of ZnO NW. ZnO NWs with small diameter grew independently at the initial deposition step and fused together as the growth of ZnO NWs proceeded, resulting in larger diameter [18]. The SEM analysis supports the growth mechanism of ZnO NWs in that the density of ZnO NWs decreased with the increase of the deposition period. Height of ZnO NW arrays can be adjusted by varying the ZnO NW deposition period. Various heights of ZnO NW arrays are exhibited in Figure 4.6. ZnO NWs grew taller with an increase of the deposition period. The height of ZnO NW arrays is fairly uniform over the entire area of the substrate.

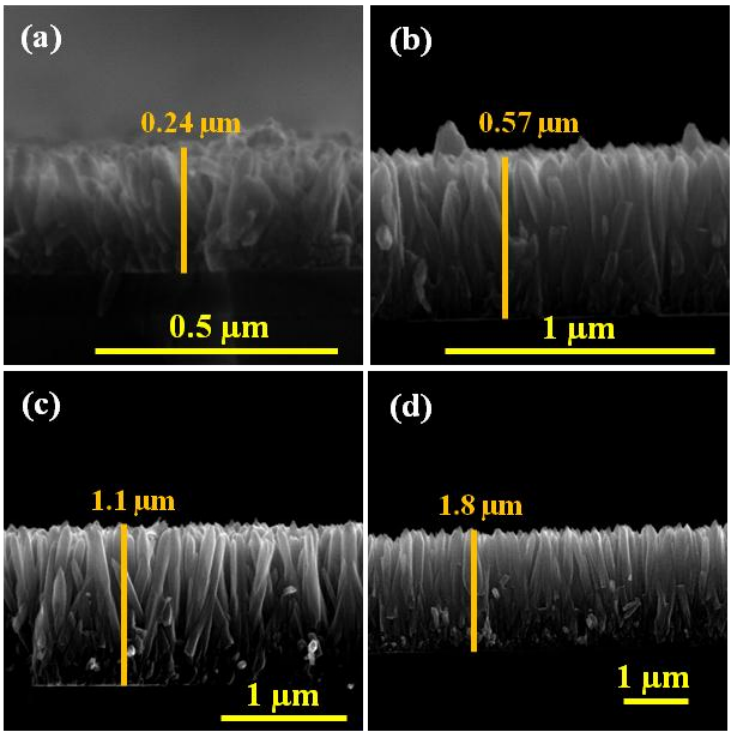

Figure 4.6. Cross sectional views of ZnO NW arrays grown in various deposition period : (a) 1 min., (b) 5 min., (c) 10 min., and (d) 20 min.

We prepared ZnO NW arrays at 4 different deposition periods to estimate the growth rate of ZnO NW arrays. The growth rate of ZnO NW was found to be about 88 nm/ min. and almost linearly increased with respect to the deposition period (Figure 4.7). To the best of our knowledge, this is the highest reported growth rate of ZnO NW array comparing to previously reported ZnO NW growth rates [12, 15, 19].

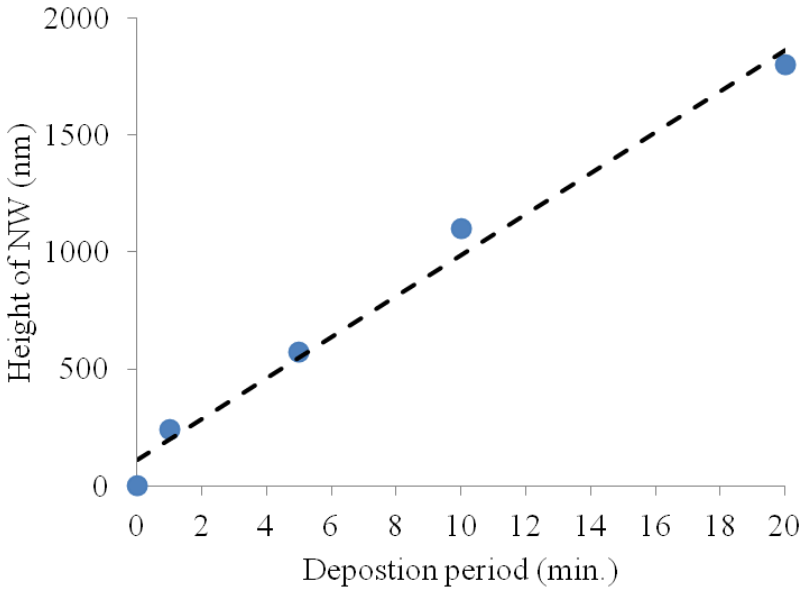

Figure 4.7. Estimated growth rate of ZnO NW arrays.

4.4. Conclusions

Vertical ZnO NW arrays were grown on the SiO_2 substrate by using the continuous flow microreactor system. Amorphous phase ZnO assembly were synthesized in the system and directly deposited onto the substrate as seed layer for the growth of vertical ZnO NW arrays. Colloidal ZnO nanocrystals, also prepared in the system, were deposited onto the amorphous ZnO seed layer for the growth of vertical ZnO NW arrays. Prior to the formation of ZnO NW arrays, polycrystal

ZnO layer was formed on the amorphous ZnO seed layer and promote the epitaxial growth of ZnO NW arrays. The growth parameters were varied to investigate their effects on the growth of ZnO NWs. The ZnO NW deposition period significantly affect the aspect ratios of ZnO NW arrays. Growth rate was estimated based on the height variation of ZnO NW arrays as a function of the deposition period. This study clearly shows the advantages of the continuous flow microreactor system in terms of fabricating vertical ZnO NW arrays.

4.5. References

[1] A. P. Alivisatos, Journal of Physical Chemistry, 100, 13226 (1996)

[2] Y. R. Ryu, T. S. Lee, J. A. Lubguban, H. W. White, B. J. Kim, Y. S. Park, and C. J. Youn, Applied Physics Letters, 88, 241108 (2006)

[3] M. H. Huang, S. Mao, H. Feick, H. Q. Yan, Y. Y. Wu, H. Kind, E. Weber, R. Russo, and P. D. Yang, Science, 292, 1897 (2001)

[4] Q. Wan, Q. H. Li, Y. J. Chen, T. H. Wang, X. L. He, J. P. Li, and C. L. Lin, Applied Physics Letters, 84, 3654 (2004)

[5] J. Goldberger, D. J. Sirbuly, M. Law, and P. Yang, Journal of Physical Chemistry B, 109, 9 (2005)

[6] M. Law, L. E. Greene, J. C. Johnson, R. Saykally, and P. D. Yang, Nature Materials, 4, 455 (2005)

[7] L. Vayssieres, Advanced Materials, 15, 464 (2003)

[8] K. Govender, D. S. Boyle, P. B. Kenway, and P. O'Brien, Journal of Materials Chemistry, 14, 2575 (2004)

[9] A. Sugunan, H. C. Warad, M. Boman, and J. Dutta, Journal of Sol-Gel Science and Technology, 39, 49 (2006)

[10] L. E. Greene, B. D. Yuhas, M. Law, D. Zitoun, and P. Yang, Inorganic Chemistry, 45, 7535 (2006)

[11] Y. Tak and K. J. Yong, Journal of Physical Chemistry B, 109, 19263 (2005)

[12] J. Song and S. Lim, Journal of Physical Chemistry C, 111, 596 (2007)

[13] L. E. Greene, M. Law, D. H. Tan, M. Montano, J. Goldberger, G. Somorjai and, P. D. Yang, Nano Letters, 5, 1231 (2005)

[14] C. Choi and C.-h. Chang, Crystal Engineering Communication, accepted manuscript (2013)

[15] L. E. Greene, M. Law, J. Goldberger, F. Kim, J. C. Johnson, Y. F. Zhang, R. J. Saykally and, P. D. Yang, Angewandte Chemie-International Edition, 42, 3031 (2003)

[16] L.-W. Ji, S.-M. Peng, J.-S. Wu, W.-S. Shih, C.-Z. Wu, and I. T. Tang, Journal of Physics and Chemistry of Solids, 70, 1359 (2009)

[17] W.-Y. Wu, C.-C. Yeh, and J.-M. Ting, Journal of the American Ceramic Society, 92, 2718 (2009)

[18] Q. C. Li, V. Kumar, Y. Li, H. T. Zhang, T. J. Marks, and R. P. H. Chang, Chemistry of Materials, 17, 1001 (2005)

[19] R. B. Peterson, C. L. Fields, and B. A. Gregg, Langmuir, 20, 5114 (2004)

. Chapter 5. Capillary Rise of Nanostrucutred Microwicks

Changho Choi, Shankar Krishnan, Ward TeGrotenhuis, and Chih-hung Chang

Processed manuscript

Flower ZnO nanostructures were successfully deposited on microwick structures which are specially designed to augment boiling heat transfer performance. A continuous flow microreactor system was employed with a flow cell to deposit the nanostructures on large microwicks (4.3cm X 10.7cm). Capillary rise experiments, height measurement and weight gain method, were performed using water and ethanol (EtOH) as the working liquids to characterize wicking dynamics on the coated and "bare" microwicks. Four analytical models of wicking dynamic were compared with the wicking rise experimental data of nanostructured ZnO coated microwick structure. It was found that the gravity plays an important role in wicking rise of the coated wick structure. Capillary rise that was determined by the mass gain approach revealed that the ZnO nanostructures enhance the capillarity rise regardless of the type of working liquid. The coated microwick structure show the most efficient capillary rise when EtOH was used as the working liquid. Wiggles of capillary rise were observed from the mass gain data when water was used the working liquid.

5.1. Introduction

Capillarity is the ability of liquids to propel through "small gaps" without the assistance of external forces. It has attracted much interest in various fields such as

oil recovery, dying of textile fabrics, and ink printing [1-4]. The phenomena of capillarity have been investigated in both fundamental science and industrial practice [5-8]. Since, capillarity concerns the interface that equilibrates the surface energy with gravitational force, it has been used to determine the radius of pores via capillary rise measurements. The Lucas-Washburn equation, formulated from Poiseuille's equation, has been introduced to study the penetration of liquid into porous structures [9]. This approach has been considered as a basic instrument for the prediction of the liquid mobility into porous materials [10]. Recently, a rising number of criticisms regarding the feasibility of the Lucas-Washburn equation have been proposed in particular for irregular porous media [11-13]. New analytical and numerical models have been developed to account for capillary rise phenomena and widely applied in models ranging from simple porous structure to complicated structures such as multi-scale porous media [14-16].

It is known that processing gases and liquids together in microchannels having at least one dimension <1 mm has unique advantages for rapid heat and mass transfer. One approach for managing the two phases is to use porous structures as wicks within microchannels to segregate the liquid phase from the gas phase. At Pacific Northwest National Laboratory (PNNL), gas-liquid processing is accomplished by providing a gas flow path and a separate flow for the liquid phase through the wick under an induced pressure gradient [17]. These microwick technologies enable a variety of unit operations including phase change, heat exchange, phase separation, partial condensation, absorption, desorption, and distillation [18-20]. New wicking structures are being developed at PNNL that are capable of wicking liquid and accommodating vapor flow in the same space [21].

These structures are referred as ‘dual-mode’ wicks because they display multiple time scales and length scales in wicking fluids (shown in Figure 5.1). These porous structures enable the wicking evaporators that display boiling heat transfer enhancement [22]. The interwoven liquid and vapor paths in dual-mode wicks facilitate phase segregation and suppress or delay dry out of heated surfaces. Experimental results are presented showing heat transfer coefficients exceeding 20,000 W/m^2K. Other characteristics demonstrated in [22] include reduced pressure fluctuations, and lower superheat requirements when compared to plain channels.

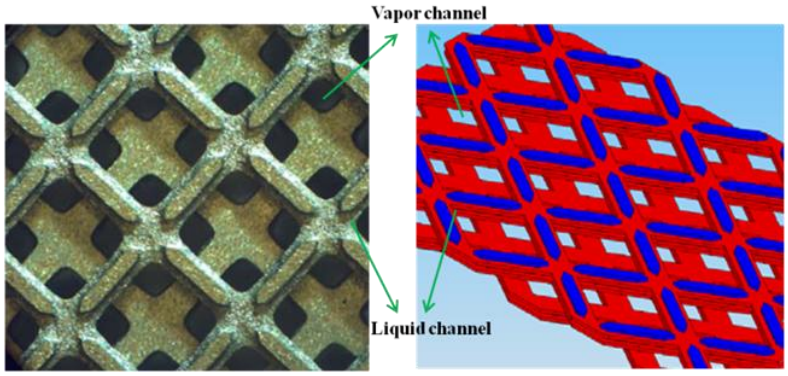

Figure 5.1. Scheme of dual-mode microwick structure.

Wettability of these microwick structures plays an important role in terms of optimizing the performance of the microwick structure. In our prior work, a 3X enhancement in critical heat flux (CHF) and 10X in boiling heat transfer coefficient was observed in pool boiling experiments with superhydrophillic surfaces [23]. We have developed unique superhydrophillic surfaces by coating ZnO nanostructures with dual-scale surface roughness on various plain substrates.

Contact angles of less than 20^{o} were achieved on aluminum substrates coated with nanostructures (versus 104° on bare aluminum substrates).

In this study, the microwick structures (3.8cm X 10.2cm) were coated with flower ZnO nanostructures by using a continuous flow microreactor stystem with a flow cell to enhance the capillarity of the microwick structure. Two types of measurements based on penetration distance method and liquid mass gain method were conducted to analyze the wicking rise of the plain microwick structure and the coated microwick structures using water and ethanol as the working liquids. A number of analytical models were used to calaulte the capillaty rise and compared with the experimental capillary rise data.

5.2. Experimental

5.2.1. Deposition of flower ZnO nanostructure on the microwick structure

Flower ZnO nanostructures were deposited on the microwick structure by using a continuous flow microreactor system along with a flow cell. The microwick structure that consists of liquid and vapor channel is shown in Figure 5.1. The dimension of the microwick structure is also given in Table 5.1.

Table 5.1. Geometrical factors of the microwick structure

Width (cm)	Length (cm)	Thickness (μm)	Hydraulic diameter of liquid channel (μm)	Ratio of vapor to liquid volume
3.81	10.2	102	63	2.5-3

ZnO is a versatile material with many potential applications including light emitting diodes, field effect transistors, ultraviolet lasers, chemical sensors, and solar cells [24-27]. Since size and morphology of ZnO nanostructures play an

important role in determining physical properties, numerous efforts have been made to control its size and morphology. In solution-based synthetic technique, solution conditions such as pH, temperature, and concentration of precursor lead to various ZnO morphologies including rod-like, prism, and flower like structures [28-30]. These structures were generally obtained by the hydrothermal and solvothermal technique with at least several hours of reaction time. The modification of the structures is a result of the dissolution-crystallization mechanism during the aging process. In the continuous flow microreactor system, on the other hand, the growth mechanism is very distinct from the conventional growth mechanism. The unique characteristics of the continuous flow microreactor system were already discussed in the previous chapter. The schematic diagram of the continuous flow microreactor system for the flower structure deposition on the microwick structure is shown in Figure 5.2. The system consists of a microprocessor controlled dispensing pump (Ismatec), Tygon ST tubing (1.2 mm ID, Upchurch Scientific), and a micro T-mixer (Upchurch scientific). A flow cell made of an aluminum block was specifically designed to accommodate the microwick structure for the deposition. Three cartridge heaters were embedded in the flow cell to provide uniform heat distribution, and heat flux was controlled by a variac. Reaction temperature during the deposition was monitored by three thermocouples placed nearby the deposition area. The temperature variation was monitored and controlled via the LABVIEW software. The cover was made of a transparent polycarbonate material that allows for the observation of the deposition process. The flow cell was tightly sealed with a rubber gasket to prevent any

possible leaking of solution. Three holes on the cover provided two inlet streams and one outlet stream for the solution flux.

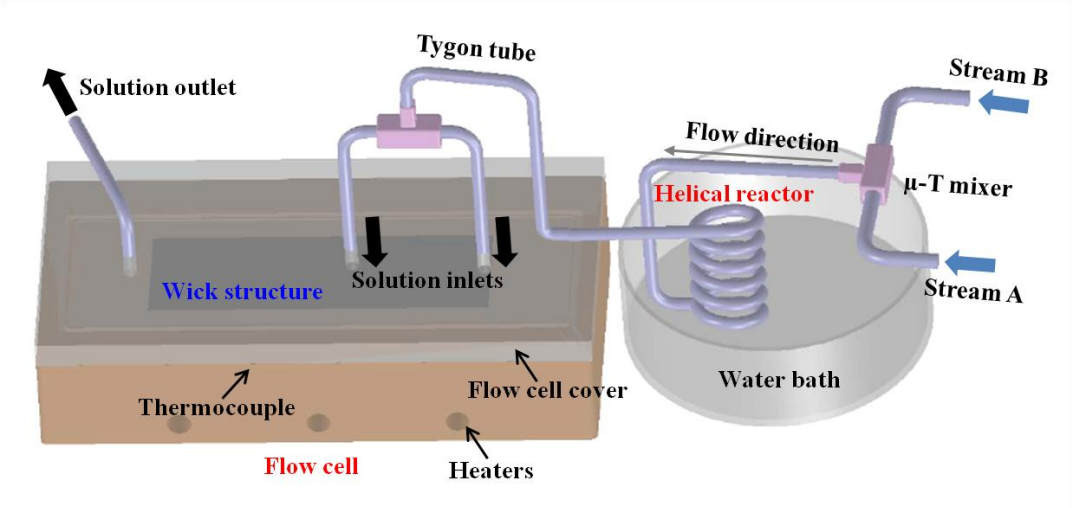

Figure 5.2. Scheme of the continuous flow microreactor system with flow cell.

The reactants, zinc acetate ($Zn(CH_3COO)_2 \cdot 2H_2O$, Sigma Aldrich), ammonium acetate (CH_3COONH_4, Mallinckrodt Chemicals), and sodium hydroxide (NaOH, Mallinckrodt Chemicals), were used as received without further purification. Stream A composed of 0.005 M zinc acetate and 0.25 M ammonium acetate solution and stream B (0.05 M NaOH) were initially pumped into the Tygon tubing and allowed to mix homogeneously in a micro-T-mixer. The solution mixture of A and B then passed through a 5 ft long helical structured reactor. By immersing the reactor in the water bath, the reaction temperature (70 ℃) was maintained throughout the growth process. The solution then entered the flow cell maintained at constant temperature (70 ℃). ZnO nanostructures were deposited onto the microwick structures as the solution flowed over the microwick structure. The solution flowed out through the outlet port. Deionized water (DI) water was

used throughout the experiment and vigorously degassed to remove dissolved air prior to the deposition. The vigorous degassing process was necessary to prevent bubble creation during the deposition, which would increase the pressure drop inside the flow cell and cause irregular deposition. Flow rate of the solution adopted for the nanostructure deposition was 14.7 mL/min.

5.2.2. Capillary rise measurement-height measurement & mass gain approach

The capillary rise measurement was performed at room temperature (19 ℃). The coated wick structure was cleaned with acetone, ethanol and DI water in a ultrasonic bath to remove contaminants prior to the wicking measurement. Then the wick structure was completely dried using nitrogen gas.

Capillary rise was characterized by the height variation with respect to time. This capillary rise measurement involved placing one end of the wick structure into a liquid that is wetting the material. The wick structure was lowered until one end of the structure was wet by the liquid. At time t = 0, the wicking sample made contact with the liquid. The liquid front was visually observed by the naked eye. The liquid penetration into the structures was recorded by a high resolution HD camcorder (Canon HG10, 6.1megafixel resolution) until it reached a steady state. Recording was performed at a rate of 30 frames per second, and the liquid front was analyzed using the video-editing software, Final Cut Pro. Because the wicking front was not even due to the irregular pore size of the coated wick structure, average height of wicking front over the width of the structure was estimated and used to construct the plot of the experimental capillary rise.

Capillary rise was also characterized by measuring the mass variation of the microwick structures as a function of time. The wick structure was directly connected to a programmable scale (OHAUS, EP114C). Working liquid was slowly lifted up by using a height controller until the liquid wetted the wick structure. The mass variation was monitored by the fine scale and saved usingthe LABVIEW software every 0.3 seconds. Similar to the height measurement method, time t=0 was taken as the microwick structures were brought into the contact with the liquid. Weight of working liquid was recorded from the initial wetting of the wick structure to the complete evaporation of working liquid after detachment of the wick structure from the liquid.

5.3. Results and Discussion

5.3.1. Synthesis of flower ZnO nanostructure in the continuous flow microreactor system

For the deposition of the flower structure on the microwick structure, a continuous flow microreactor system was used. The chemical components and process conditions are exactly the same as those used for the growth of flower structure on the SiO_2 substrate (Chapter 3). Figure 5.3 shows SEM images of flower ZnO nanostructure and a photograph of the coated wick structure. Size and shape of ZnO nanostructures varied depending on the position of the wick structure. This could be attributed to the fact that ZnO nanostructures near the solution outlet have more the assembled ZnO structure for the growth of flower structure than those near the solution inlet. For the growth of the nanostructure near the solution outlet area, ZnO assembly from solution inlet 2 and the remnant

of ZnO assembly from solution inlet 1 both participate inthe formation of ZnO flower like structure. The deposition of the flower like structures creates nano- or micro porous structure. These pores provide the channel for working liquid to penetrate upward by capillary force.

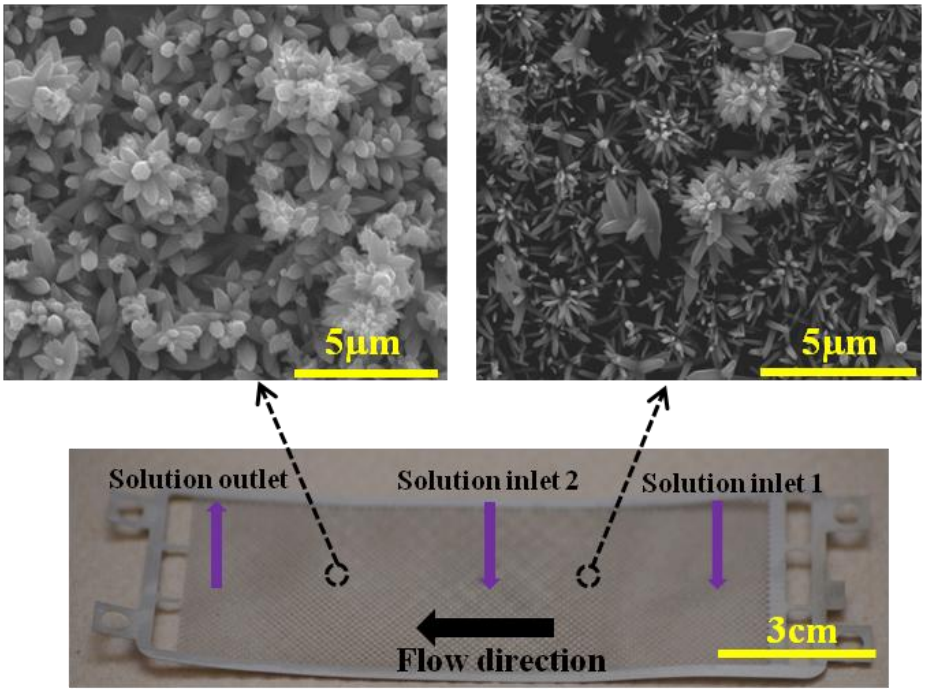

Figure 5.3. SEM images of flower ZnO nanostructure and photograph of the coated wick structure.

5.3.2. Capillary rise of the coated wick structure

Figure 5.4 shows temporal evolution of the capillary rise height of EtOH for nanocoated microwick structures. The capillary rise height reaches a steady state about ~ 500 seconds. The equilibrium height at steady state is 80mm. In order to investigate the parameters that affect the capillrary rise of the coated wick structure, a number of analytical models are compared with the experimental results as shown in Figure 5.4.

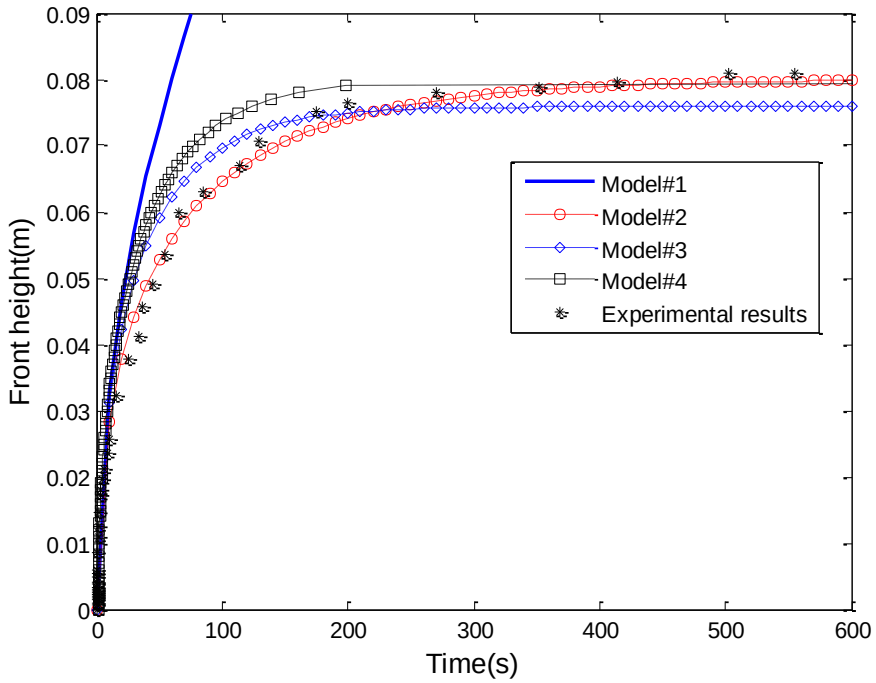

Figure 5.4. Comparison of experimental wicking results with calculation results from analytical models.

Several analytical models have been proposed to predict the capillary rise and widely used to investigate the wicking process of regular or irregular porous systems.

(1) The Lucas-Washburn (L-W) equation is the simplest formation by taking negligible gravitational and evaporation effects [9]. Capillary force is balanced with viscous force.

$$\frac{2\sigma\cos\theta_s}{R_s} = \frac{\phi}{K}\mu h\dot{h}$$

$$h^2 = \frac{4\sigma\cos\Theta}{\phi\mu}\frac{K}{R_s}$$

Equation (1) is the L-W equation expressed with permeability (K) and porosity by correlating with the Darcy's law.

(2) Fries *et al.* recently reported a model accounting for the gravitational effects only with negligible evaporation effects [31]. Capillary force is balanced with gravity and viscous force.

$$\frac{2\sigma\cos\theta_s}{R_s} = \rho g h + \frac{\phi}{K}\mu h\dot{h}$$

$$h(t) = -\frac{a}{b}\left[1 + W\left(-e^{-1-\frac{b^2 t}{a}}\right)\right]$$

$$a = \frac{2\sigma\cos\Theta}{\phi\mu}\frac{K}{R} \qquad b = -\frac{\rho K g}{\phi\mu}$$

The Lambert W function was used to extract the wicking rise as a function of wicking time.

(3) The model accounting for evaporation effects only was also proposed recently by Rogacs *et al.* [32]. Capillary rise level out viscous force and evaporation effect.

$$\frac{2\sigma\cos\theta_s}{R_s} = \frac{\phi}{K}\mu h\dot{h} + \frac{\mu\dot{m}_e}{2d\rho K}h^2$$

$$h(t) = \sqrt{\frac{a}{c}(e^{2ct} - 1)}$$

$$c = \frac{-\dot{m}_e}{2d\rho\phi}$$

(4) The full and implicit model was reported by Fries *et al.* to depict all effects such as capillary rise, gravity force, viscous pressure loss, and evaporation effects [33].

$$\frac{2\sigma\cos\theta_s}{R_s} = \rho g h + \frac{\phi}{K}\mu h\dot{h} + \frac{\mu\dot{m}_e}{2d\rho K}h^2$$

$$t = \frac{1}{2c}\left(\ln\left|\frac{ch^2+bh+a}{a}\right|\right) - \frac{b}{2c\sqrt{b^2-4ac}}\left(\ln\left|\frac{(2ch+b-\sqrt{b^2-4ac})(b-\sqrt{b^2-4ac})}{(2ch+b+\sqrt{b^2-4ac})(b+\sqrt{b^2-4ac})}\right|\right)$$

In Figure 5.4, the model 1 (the L-W equation) is much deviated from the experimental capillary rise. Such a deviation is anticipated due to the fact that both evaporation and gravity effects are expected to influence the capillary rise of the wick structure. It is generally known that gravity effect is only negligible at the initial rise of working liquid. Nevertheless, the L-W equation is very useful in determining the pore parameter (K/R_s) of the coated wick structure. Because evaporation and gravity effects are negligible at initial capillary rise, the pore parameter can be extracted by analyzing initial capillary rise regime with known physical variables in the L-W equation (model 1). In addition, it was reported that the L-W equation is valid for the wicking rise up to 10% of equilibrium wicking height [31]. The obtained value of the pore parameter (K/R_s) can then be applied to plot the other analytical models. Porosity (ϕ) was estimated by calculating the ratio of actual mass of the wick structure and mass calculated from dimension of the wick structure with free of pores and density of the wick structure. Contact angle was determined to be 0° based on the static contact angle measurement made on planar area of the coated wick structure ($\cos \theta=1$).

The model 2 accounts for the capillary rise with gravitiy effect with negligible evaporation. The Lambert W function was solved with given and calculated variables by using the MATLAB software. The plot of the model 2 agree very well with the experimental capillary rise data.

Rogacs *et al*. proposed an analytical model that includes evaporation effect with negligible gravity influence (model 3). The model 3 requires the evaporation rate (m_e) which can be estimated by analyzing results of the mass gain approach. Figure 5.5 shows the wetting and de-wetting dynamics of EtOH in the coated wick

structure measured by the mass gain approach. Four distinct regimes are evident in Figure 5.5. As the wick structure was brought into the liquid, the liquid wetted the wick structure (1). Initially, due to capillary pressure the wicking rise accelerated (gravity has negligible influence in this regime). Liquid-uptake continued to increase with time and eventually attained a steady state when the capillary pressure, hydrostatic pressure, and evaporation effect reached an equilibrium state (2). Once the mass uptake reaches a steady state, the wick structure was lifted up, referred as the de-wetting regime (3). Then, the wetted wick structure was left in an open chamber (i.e. unsaturated environment) until the evaporation process was completed (mass = 0) (4).

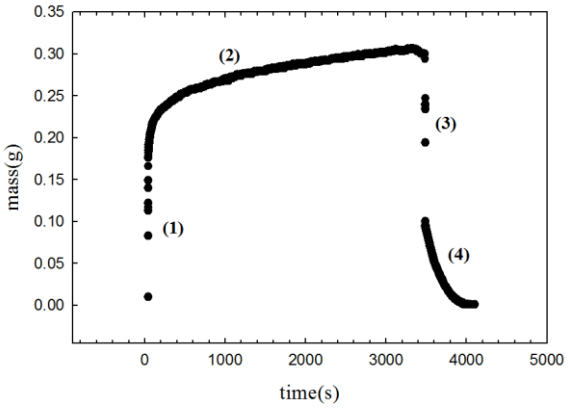

Figure 5.5. Mass gain approach of the coated wick structure in EtOH; (1) wetting regime, (2) wicking regime, (3) de-wetting regime, and (4) evaporation regime.

The evaporation regime provides an important key to determine the mass flow due to the evaporation effects. The mass of evaporated liquid per area and time ($\dot{m}_e$) was calculated by analyzing the evaporation regime, and this mass value was used to obtain the mass flow rate due to evaporation ($\dot{M}_e$) [33]. The calculated mass flow rate due to the evaporation is about 2.62×10^{-7} kg/s while the mass flow rate

for the capillary rise is about 1.60×10^{-6} kg/s, which means that evaporation affects the capillary rise of EtOH in the nanocoated wick structure (about 16.3 % of mass is evaporated). With the estimated evaporation rate ($\dot{m}_e$), the analytical model 3 is plotted in Figure 5.4. It is revealed that the model 3 is deviated from the experimental results especially when the liquid becomes the equilibrium state. This confirms the role of the gravity effects in the wicking rise of the coated wick structure. Rogacs *et al*. developed the model 3 to characterize the wettability of nanostructured porous thin film (~10µm film thickness) made by hydrophilic silicon nanowire arrays [32]. They reported a simple criterion to determine whether evaporation or gravity effects can be ignored, which depended on sample sizes and experimental conditions. The valid film dimension for the negligible gravity effects was reported to be less than 10 µm film thickness and less than 4cm wicking height. In our wick structure, the film thickness is less than 10 µm because the typical height of the flower petal is around 1µm. However, as shown in Figure 5.3, the maximum height is around 8 cm, which is about 2× larger than a typical thin film suitable for negligible gravity effects. Therefore, in our wicking rise of the coated wick structure, the gravity effects should be considered. A comprehensive model 4 is also compared with the experimental results in Figure 5.4. The model 4 is somewhat deviated from the experimental capillary rise. Fries *et al.* reported an average deviation between the model 4 and their experimental results to be around 20%. The factors causing such as deviation were also reported [33]. The ambiguity of the model 4 was also observed during the extraction of certain wicking parameters under typical experimental conditions [32].

Based on the comparison of the experimental wicking rise with the analytical models, we can determine the relative importance of evaporation and gravity effects on the wicking rise of the coated wick structure. Gravity force is more influential than evaporation effect for our wicking measurement although evaporation is practically observed, which leads to better agreement between the model calculations and experimental data using model 2 than model 3. The descripancy between model 3 and experimental data may be attributed to the inaccuracy of height analysis and evaporation effect as well. The variables used to solve the analytical models are listed in Table 5.2.

Table 5.2. Physical properties of EtOH used for the capillary rise study

Characteristics of EtOH at 19°C	
σ_{lv} [N/m]	0.0239
cosθ	1
ρ [kg/m^3]	789
g [m/s^2]	9.8
μ [N·S/m^2]	0.0012

Figure 5.6 shows the capillary rise obtained by the mass gain measurement. Figure 5.6a shows the effect of employing different liquids on the dynamics of capillary rise of coated and bare wicks. It should be noted that mass uptake plotted on the vertical axis is normalized with dry weight of the wick. It is observed that the capillary rise of the coated wick structure is enhanced for both working liquids, as compared to that of the bare wick structure. The nanostructure coating enhancement on the capillary rise is more pronounced when EtOH is used as the

working liquid compared to water. Thus, the most efficient capillary rise can be obtained using the coated wick structure with EtOH. The capillary rise at the initial contact regime is shown in Figure 5.6 b. Wicking rate of the coated wick structure is about 7× larger than that of the bare wick structure. Wicking rate is an important characteristic in filling the liquid into porous media particularly for absorbing technology [34]. A unique feature of the capillary rise with water is displayed in Figure 5.6c. The capillary front of water penetrates into the liquid channel of the microwick structure showing a step-rise increment. This may be due to the presence of periodically varying pores as discussed in the literature [35].

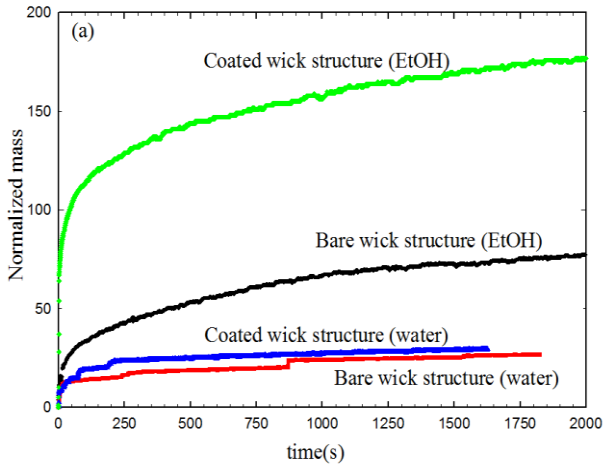

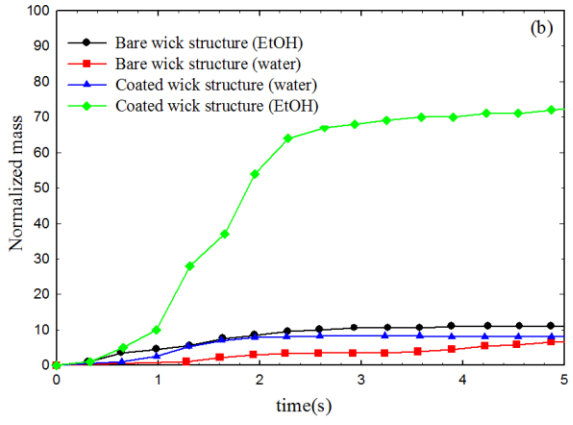

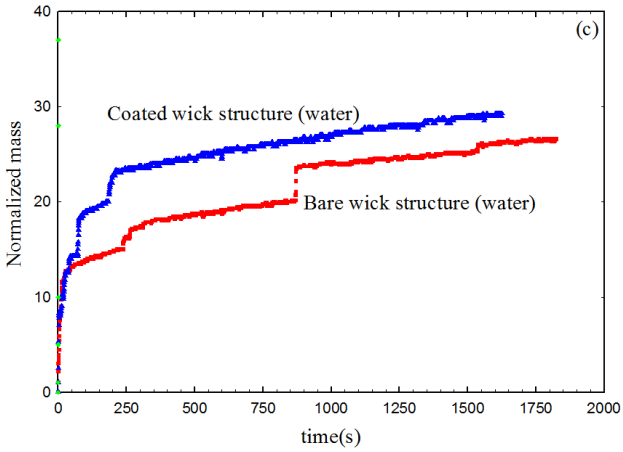

Figure 5.6. Capillary rise curves measured by the mass gain approach: (a) comparison of all tested single-mode wick structure, (b) capillary rate at initial wicking, (b) closer look of step-rise wicking rise.

5.4. Conclusions

Flower ZnO nanostructures were deposited onto the microwick structure using a continuous flow microreactor system along with a flow cell. Colloidal ZnO nanocrystals synthesized in the system were used as the building blocks for the growth of flower-like ZnO nanostructured films. Height measurement and mass gain approaches were performed to study the capillary phenomena of the coated microwick structure. The results of the EtOH wicking rise was compared with a number of analytical models and found that gravity effect is most influential in the capillary rise of the coated wick structure. It was also found from the results of mass gain approaches that EtOH is the most efficient wicking liquid for the coated wick structure. Wiggles of capillary rise were observed in the capillary rise data of water obtained from the mass gain measurement. This was attributed to the irregular pore of the flower ZnO nanostructure.

5.5. References

[1] V. H. Hammond and A. C. Loos, Journal of Reinforced Plastics and Composites, 16, 50 (1997)

[2] C. E. Hendriks, P. J. Smith, J. Perelaer, A. M. J. Van den Berg, and U. S. Schubert, Advanced Functional Materials, 18, 1031 (2008)

[3] B. Y. Jamaloei, R. Kharrat, K. Asghari, and F. Torabi, Journal of Petroleum Science and Engineering, 77, 121 (2011)

[4] R. Ohigashi, K. Tsuchiya, Y. Mita, and H. Fujita, Journal of Microelectromechanical Systems, 17, 272 (2008)

[5] K. A. Culligan, D. Wildenschild, B. S. B. Christensen, W. G. Gray, and M. L. Rivers, Advances in Water Resources, 29, 227 (2006)

[6] T. Dang-Vu and J. HUPKA, in Physicochemical problems of mineral processing, Physicochemical problems of mineral processing, 47 (2005)

[7] D. Quere, E. Raphael and J. Y. Ollitrault, Langmuir, 15, 3679 (1999)

[8] B. V. Zhmud, F. Tiberg, and K. Hallstensson, Journal of Colloid and Interface Science, 228, 263 (2000)

[9] E. W. Washburn, in The Physical Review, The Physical Review, 273 (1921)

[10] J.SZEKELY, A. W. NEUMANN, and Y. K. CHUANG, Journal of Colloid and Interface Science, 35, 273 (1971)

[11] H. T. Xue, Z. N. Fang, Y. Yang, J. P. Huang, and L. W. Zhou, Chemical Physics Letters, 432, 326 (2006)

[12] D. Patro, S. Bhattacharyya, and V. Jayaram, Journal of the American Ceramic Society, 90, 3040 (2007)

[13] R. Chebbi, Journal of Colloid and Interface Science, 315, 255 (2007)

[14] T. S. Lundstrom, L. H. Gustavsson, N. Jekabsons, and A. Jakovics, Aiche Journal, 54, 372 (2008)

[15] S. Amico and C. Lekakou, Transport in Porous Media, 54, 35 (2004)

[16] S. Benltoufa, F. Fayala, and S. BenNasrallah, Journal of Engineered Fibers and Fabrics, 3, 47 (2008)

[17] W. E. TeGrotenhuis and V. S. Stenkamp, in *ACS Symposium Series 914*, Washington, DC, pp. 360-377 (2005)

[18] W. E. TeGrotenhuis and V. S. Stenkamp, in 1st International Conference on Microchannels and Minichannels, ICMM2003-1089, 699 (2003)

[19] X. Huang, D. A. King, F. Zheng, V. S. Stenkamp, W. E. TeGrotenhuis, B. Q. Roberts, and D. L. King, Catalysis Today, 136, 291 (2008)

[20] W. E. TeGrotenhuis, R. S. Wegeng, G. A. Whyatt, V. S. Stenkamp and P. A. Gauglitz Microsystem Capillary separations, US Patent Number 6,666909B

[21] W. E. TeGrotenhuis, P. H. Humble, L. C.A. and D. D. Caldwell, Enhanced Two Phase Flow in Heat Transfer System, US2009/0321053 A1. 2008

[22] S. Krishnan and W. E. TeGrotenhuis, in International Refrigeration and Air Conditioning Conference, Perdue, Vol. 2548 (2012)

[23] T. J. Hendricks, S. Krishnan, C. Choi, C.-H. Chang, and B. Paul, International Journal of Heat and Mass Transfer, 53, 3357 (2010)

[24] J. Bao, M. A. Zimmler, F. Capasso, X. Wang, and Z. F. Ren, Nano Letters, 6, 1719 (2006)

[25] B. Sun and H. Sirringhaus, Nano Letters, 5, 2408 (2005)

[26] S. Hirano, N. Takeuchi, S. Shimada, K. Masuya, K. Ibe, H. Tsunakawa, and M. Kuwabara, Journal of Applied Physics, 98, 094305 (2005)

[27] J. H. Xiang, P. X. Zhu, Y. Masuda, M. Okuya, S. Kaneko, and K. Koumoto, Journal of Nanoscience and Nanotechnology, 6, 1797 (2006)

[28] B. Weintraub, Z. Zhou, Y. Li and Y. Deng, Nanoscale, 2, 1573 (2010)

[29] J. Zhang, L. D. Sun, J. L. Yin, H. L. Su, C. S. Liao and C. H. Yan, Chemistry of Materials, 14, 4172 (2002)

[30] Y. Zhang and J. Mu, Nanotechnology, 18, 075606 (2007)

[31] N. Fries and M. Dreyer, Journal of Colloid and Interface Science, 320, 259 (2008)

[32] A. Rogacs, J. E. Steinbrenner, J. A. Rowlette, J. M. Weisse, X. L. Zheng, and K. E. Goodson, Journal of Colloid and Interface Science, 349, 354 (2010)

[33] N. Fries, K. Odic, M. Conrath, and M. Dreyer, Journal of Colloid and Interface Science , 321, 118 (2008)

[34] P. K. Chatterjee and B. S. Gupta, Absorbent Technology Elsevier, 2002

[35] T. L. Staples and D. G. Shaffer, Colloids and Surfaces a-Physicochemical and Engineering Aspects, 204, 239 (2002)

Chapter 6. Two-phase Boiling Heat Exchanger Using Metal Oxide Nanostructured Surfaces

Changho Choi, Shankar Krishnan, and Chih-hung Chang

Processed manuscript

The continuous flow microreactor system is capable of producing ZnO nanostructured surfaces with various morphologies including the flower structure, pyramidal structure, and ZnO NW arrays. One potential application of the ZnO nanostructured surfaces is to enhance two-phase boiling heat exchanger performance. These nanostructured surfaces are very attractive as nucleate boiling surfaces since they have a number of bubble nucleation sites and protrusions to increase the active boiling area. In this study, the pool boiling heat transfer measurements were performed using the ZnO nanostructured surfaces prepared by the continuous flow microreactor system. The pool boiling curves corresponding to each ZnO nanostructured surface were obtained and analyzed based on the characterizations of the boiling surfaces including surface roughness and wettability. It was found that the pyramidal structure has the best boiling performance in terms of low super heat and high critical heat flux (CHF). The least effective boiling surface is the aligned nanowire arrays due to its nanosized pore generated between nanowires and the limited nucleation boiling sites which is caused by the high density of nanowire arrays.

6.1. Introduction

Electronic system energy management and cooling for future advanced lasers, radars, and power electronics are getting more chanllenging, resulting in a search for technologies and design techniques to dissipate ultra-high heat fluxes. One of the promising approaches to meet efficient heat dissipation is utilizing the large latent heat of vaporization in two phase system, and thereby boiling heat transfer has been widely investigated. Associated with the latent heat of vaporization, the number of bubble nucleation sites plays a significant role in enhancing heat transfer performance. The surface modification techniques to increase the number of bubble nucleation sites has been developed, arising from mechanical surface treatments such as polishing technique and micro pinning technique. These enhancement techniques now extend to the nano-scaled surface modification resulting from the recent advancement of nanotechnology. A critical review associated with the nano-scaled surface modification techniques has been published recently [1]. In this review, the effect of nanostructures on the pool boiling performance was presented, and the extensive review regarding the nanostructure manufacturing techniques was exhibited. Among these techniques, nanofluids, suspensions of nanosized particles in the fluid, have been intensively studied in terms of synthetic method, characterization, thermal conductivity, and two phase heat transfer performance [2, 3]. Researchers demonstrated that the nanostructured surfaces generated by nanoparticles in fluids are attributed to the enhanced heat transfer performance increasing critical heat flux (CHF) and heat transfer coefficient (HTC). A state of art review related to nanofluids technique for boiling heat transfer is also available in literature [4]. In spite of the enhanced heat

transfer rate with nanofluids, there are several challenges in applying nanofluids to boiling performance. The aggregation of nanoparticles suspended in the fluid may occur during the boiling, which would reduce the nanoparticle dispersion. In addition, adding nanoparticles in the fluid makes the pool boiling system much more complicated and more difficult to understand the boiling mechanism.

Recently new approaches that prepare nanostructures directly on the boiling surface have been adopted. For instance, Yao *et al.* fabricated Cu and Si nanowires with different height using electro chemical deposition method [5]. They demonstrated that the height of nanowires is the key parameter to significantly influence the boiling heat transfer, and the most enhanced boiling performance could be obtained with the tallest nanowire structure. Nano-porous surface was also fabricated using anodizing technique [6]. It was reported that the Al_2O_3 nano-porous surface is capable of lowering the incipient wall superheat, improving the boiling heat transfer coefficient. However, the deterioration of the nano-porous surface was observed, which causes the elimination of the nano-porous effect on the boiling performance over the long period time. The effect of carbon nanotube (CNT) arrays on pool boiling was investigated by some researchers [7, 8]. The CNT was found to be very effective in enhancing the pool boiling performance. Pool boiling with Cu micro-porous surfaces prepared by electrochemical deposition technique was performed, and CHF was improved with the reduction of boiling incipient superheat [9].

The enhancement of pool boiling performance with nanostructured surfaces can be explained with several important characteristics. Surface roughness generated by nanostructured surface creates the potential micro cavity sites for

bubble nucleation. The surface wettability could be increased with an increase of the surface roughness according to Wenzel's model [10], which is a very significant effect to enhance the boiling heat transfer performance. In addition, capillarity of a fluid toward the bubble nucleation sites was emerged as a critical characteristic for enhanced boiling heat transfer. The capability of replenishing fluids to the boiling site by the capillary force enables the delay of dry out on the boiling surface [11]. This capillary effect is more remarkable as 1D nanostructured surfaces such as nanowires and nanotubes are applied as boiling surfaces [6, 7, 12].

In our previous work, ZnO nanostructured surfaces with different wettability were fabricated using a continuous flow microreactor system [13]. It was observed that flower ZnO nanostructure enhanced both CHF about 3 times higher and HTC about one order of magnitude compared to a bare aluminum surface. As an extension of the previous works, in this study, four different types of ZnO nanostructures (irregular flower structure, pyramidal structure, irregular nanorod (NR) structure, and aligned NW arrays) were prepared on a plain stainless steel (306) for the nucleate boiling heat transfer. We employed the continuous flow microreactor system to prepare irregular flower structure, pyramidal structure, and aligned NW arrays. Irregular NR structure was prepared by a bath hydrothermal technique.

6.2. Experimental

6.2.1. Preparation of nanostructured boiling surfaces

ZnO nanostructured surfaces with various morphologies were fabricated by using the continuous flow microreactor system. The schematic diagram of the

continuous flow microreactor system was already shown in Figure 3.1. The manufacturing methodologies for the flower structure and NW arrays were already discussed in the previous chapters. To prepare the pyramidal structure, ZnO assembly formed in 14.7ml/min flow rate was deposited directly on the ZnO seed layer in the presence of angular momentum. The rotation speed is an important parameter that determines between the pyramidal structure and aligned NW arrays. Note that the aligned NW arrays can be fabricated in the absence of the substrate rotation (Chapter 4). The experimental parameters used for the preparation of various ZnO nanostructured surfaces by the continuous flow microreactor system are summarized in Table 6.1. To fabricate irregular NR structure, a typical hydrothermal technique was used. Irregular ZnO NRs were grown in a sealed Teflon bath containing 0.1M zinc nitrate ($Zn(NO_3)_2 \cdot 6H_2O$) and 0.1M hexamethylenetetraamine (HMT) at 120℃ for 2hrs.

Table 6.1. Summary of the system parameters for fabrication of nanostructured surfaces.

	Flow rate (ml/min)	Reaction temperature (°C)	RPM of rotating disk	Deposition time
Irregular flower	14.7	70	2000	5 min.
Seed layer	28	70	2000	20 sec.
Aligned flower	14.7	70	2000	5 min.
Aligned NRs	6.8	70	0	1 min. and 20 min.

6.2.2. Pool boiling facility

The schematic illustration for the pool boiling experiment is shown in Figure 6.1. The boiling test facility consists of a copper heating block, electrical resistive heaters, and boiling chamber which is made from polycarbonate material. Heat was supplied through four 50Ω resistors soldered under the copper heating block to

provide the uniform heat distribution on the copper block. Nanostructured boiling surface was mounted on the copper heating block by soldering. Six K-type thermocouples were implemented to measure temperature. Two thermocouples were immersed in the boiling chamber to evaluate water temperature. In order to measure boiling surface temperature, two thermocouples were bonded on the surface using thermal epoxy. Temperature of the heater was read by thermocouples attached to the heaters. The boiling test facility was completely insulated by fiber glass material to assure as close as possible to one- dimensional heat flux toward the boiling surface, and the boiling chamber is also insulated by the same insulator to minimize the heat loss. The uncertainty of the measurement was estimated to be less than ± 10.2%. Data acquisition system incorporated with LABVIEW program continuously monitored and recorded all of the electrical input values as well as temperature readings. The experiment was performed at atmospheric pressure. Prior to performing the boiling test, a degassing process of DI water was rigorously carried out to assure the removal of dissolved gas for one hour using two cartridge heaters immersed in the boiling chamber. DI water was used throughout the whole experiment. Once the DI water in the boiling chamber reached saturation temperature (100℃), the cartridge heaters were gradually turned off ensuring it continuously stayed at 100℃ during the boiling test. After maintaining saturation temperature, the power on the copper heating block assembly was turned on. At the beginning of the boiling test, the increment of heat flux was kept about $5W/cm^2$. However, as CHF was approaching, the increment of heat flux was reduced to $2W/cm^2$ in order to obtain more accurate CHF value. At the incipience of CHF, the heater temperature rapidly jumped up, which could cause the electrical heater to

burn out, so the power was removed immediately to avoid the damage to the heater. The boiling performance was repeated with selected surfaces to assure the credibility of the test result.

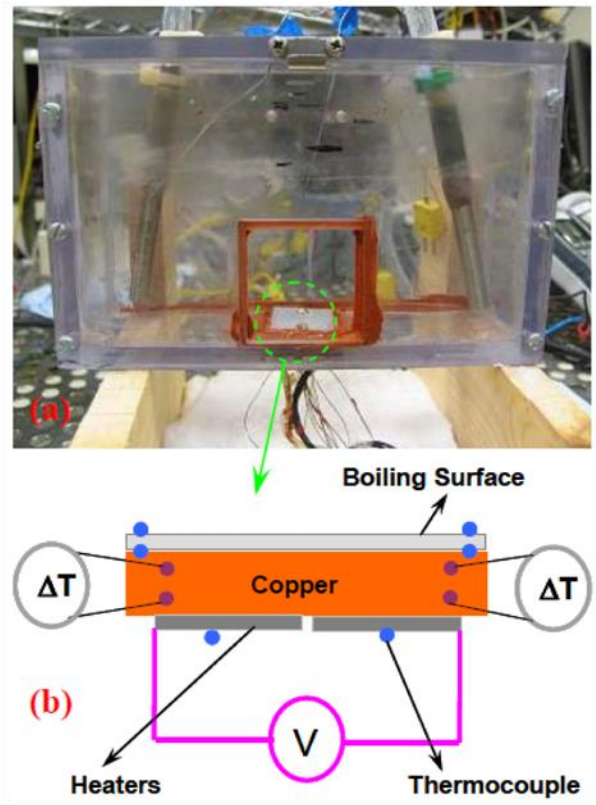

Figure 6.1. Pool boiling facility: (a) photograph of the boiling facility and (b) illustration of the instrumented test heater assembly.

6.2.3 Characterization of boiling surfaces

Boiling surfaces including the bare stainless steel substrate and nanostructured surfaces were characterized by using Scanning Electron Microscopy (SEM), contact angle measurement, Atomic Force Microscopy (AFM), and X ray Diffraction (XRD). Morphology of boiling surfaces was examined by SEM images (Quata^{TM} 3D FEG600). Wettability of working fluid was analyzed by using static contact angle measurement. For the static contact angle

measurement, 2µl DI water was dropped on boiling surfaces. A video analysis program was used to measure the static contact angle. Contact angle was averaged by measuring on four different spots. The AFM instrument (Veeco Innova SPM) was used to examine the average surface roughness of boiling surfaces. XRD data was obtained using Bruker D8 diffractometer with Cu Kα radiation (acceleration voltage: 40kv, flux: 40mA). The XRD data were used to determine crystallinity and growth orientation of ZnO nanostructure.

6.3. Results and Discussion

6.3.1. Characteristic resutls of boiling surfaces

Figure 6.2 shows the characterization of the bare stainless steel substrate. The bare substrate seems to be plane without irregular protrusion according to the SEM image. The surface roughness of the bare substrate measured by the AFM is about 0.32µm. The static contact angle was measured to be 60°.

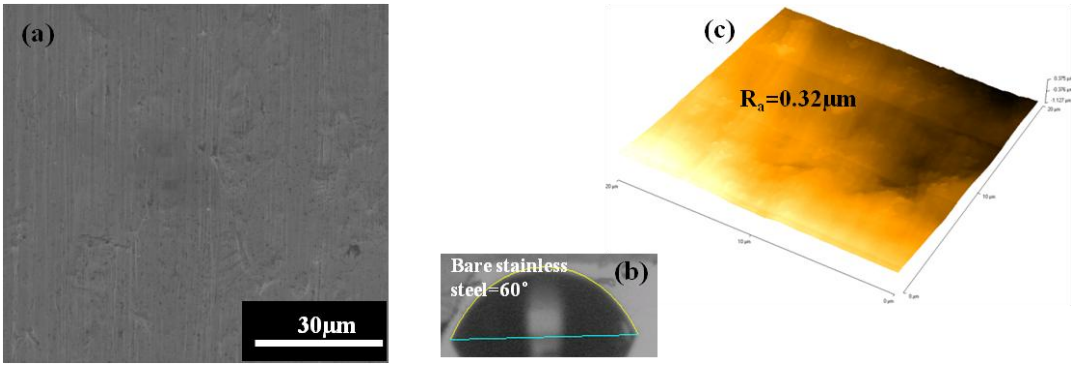

Figure 6.2. Characterization of bare stainless steel substrate: (a) SEM image, (b) contact angle measurement, and (c) average surface roughness.

The characterization of the flower structure is exhibited in Figure 6.3. Flower structure with 1µm size was irregularly deposited on the bare substrate. A number

of pores were created between the flower structures. The surface roughness was measured to be around 0.24µm, which indicates that flower structure creates nanostructured surface with high density on the bare substrate. The measured roughness is less than one of the bare substrate because the bare substrate has some micro-pores that are inevitable during the substrate treatment. Wettability was also examined although it is not shown. The average contact angle was measured to be 34°. The contact angle was significantly dependent on spots where the contact angle were measured, showing high variation. It may result from the irregularity of flower structure. The XRD data reveals typical ZnO crystal pattern confirming flower structure are irregularly grown on the substrate.

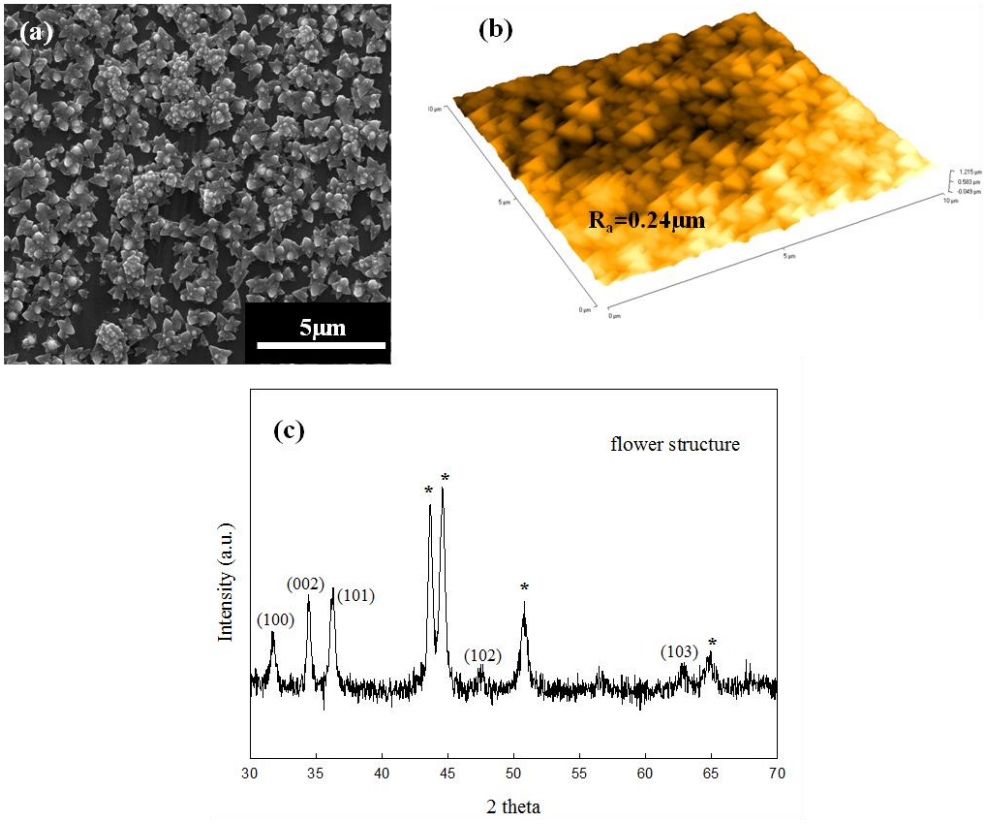

Figure 6.3. Characterization of the flower structure: (a) SEM image, (b) average surface roughness, and (c) XRD pattern (* presents stainless steel substrate).

The pyramidal structure was characterized and the results were shown in Figure 6.4. Compared to the flower structure, the SEM image reveals that the structure was vertically aligned, making very smooth plane (R_a=75nm). This is confirmed by the XRD data indicating ZnO is vertically grown with the [002] direction. The pyramidal structure has hydrophilic property, and the contact angle is relatively consistent independent upon measured spots.

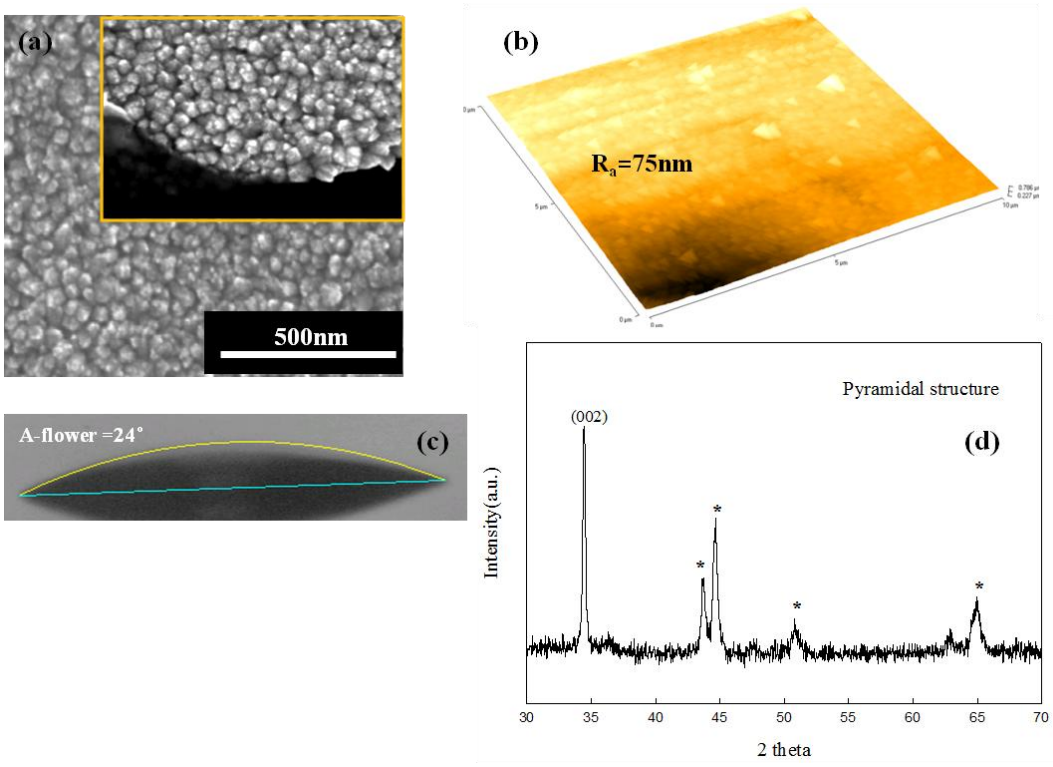

Figure 6.4. Characterization of the pyramidal structure: (a) SEM image, (b) average surface roughness, (c) contact angle measurement, and (d) XRD pattern (* presents stainless steel substrate).

In the hydrothermal reacion, ZnO NRs were irregularly grown on the bare substrate according to the SEM image (Figure 6.5). The high irregularity causes significant roughness as measured by the AFM. The irregularity also affects the

high variance of the contact angle. The average contact angle was measured to 85°. The XRD data exhibit a typical ZnO crystal pattern.

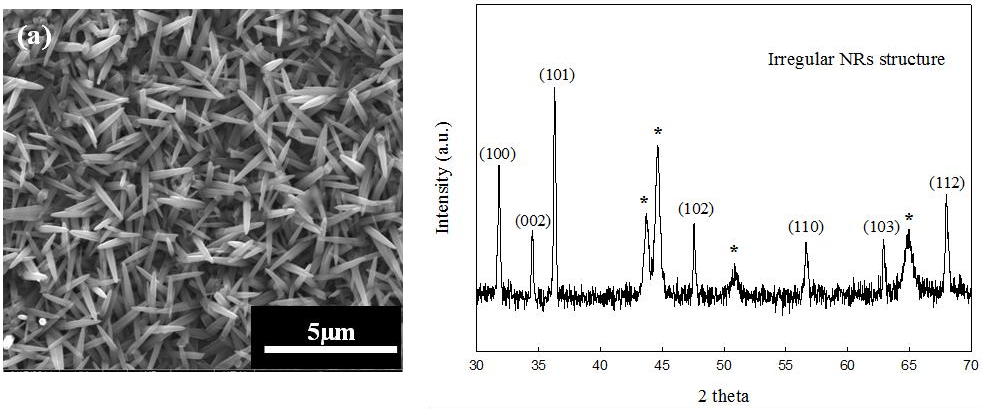

Figure 6.5. Characterization of irregular NRs structure: (a) SEM image and (b) XRD pattern (* presents stainless steel substrate).

The aligned NW arrays having low aspect ratio (L/D=5/1) was characterized as shown in Figure 6.6. The diameter and height of NWs is about 50nm and 240nm respectively. The cross-sectional image reveals that ZnO NWs were vertically grown with uniform height on the bare substrate. The average contact angle was 53° with low variation. As confirmed by the XRD data, ZnO NWs were vertically aligned with [002] growth orientation. The characterizations of the boiling surfaces are summarized in Table 6.2.

Table 6.2. Summary of characterization of the boiling surfaces

	Surface roughness (μm)	Contact angle (°)
Bare surface	0.32	60
Flower structure	0.24	34
Irregular NRs	·	85
Pyramidal structure	0.075	24
Aligned NW arrays	·	53

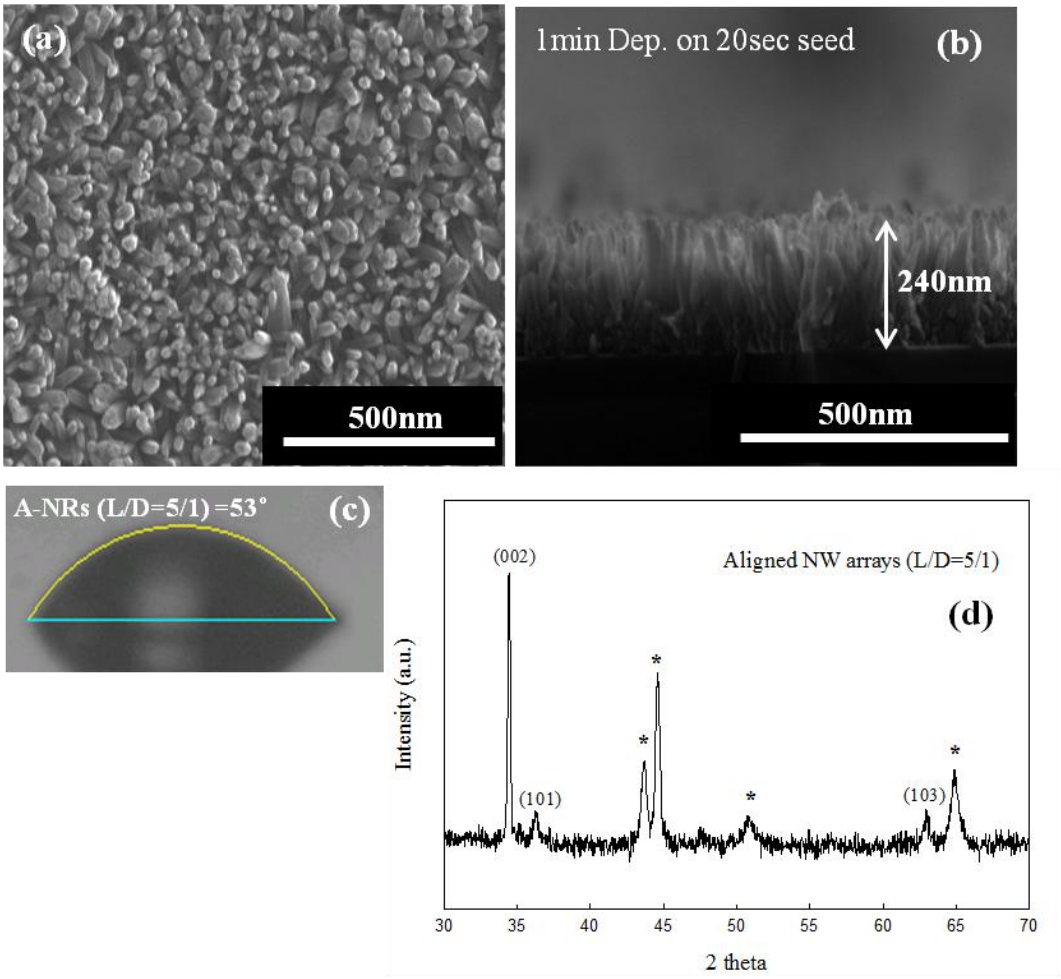

Figure 6.6. Characterization of aligned NRs structure (low aspect ratio): (a) SEM image, (b) cross-sectional image, (c) contact angle measurement, and (d) XRD pattern (* presents stainless steel substrate).

6.3.2. Nucleate boiling heat transfer

The various boiling surfaces were tested for the pool boiling heat transfer. In order to validate the boiling test facility, the common empirical models exploiting the nucleate boiling heat transfer were compared with the experimental boiling curve. The bare surface was only chosen for the comparison because the models were proposed based on nucleate boiling heat transfer results using a plain boiling surface. Figure 6.7a displays the comparison of the experimental nucleate boiling heat transfer results with Rohsenow and Stephan-Abdel models. The experimental

nucleate boiling heat transfer lies between the two models, indicating the validity of the boiling test apparatus. The empirical CHF models were also compared with the experimental CHF value of the bare surface (Figure 6.7b). Kandikar's model was shown to better depict the CHF phenomena of the nanostructured surfaces as compared to the Zuber's model, exhibiting approximate 10 % discrepancy from the experimental results.

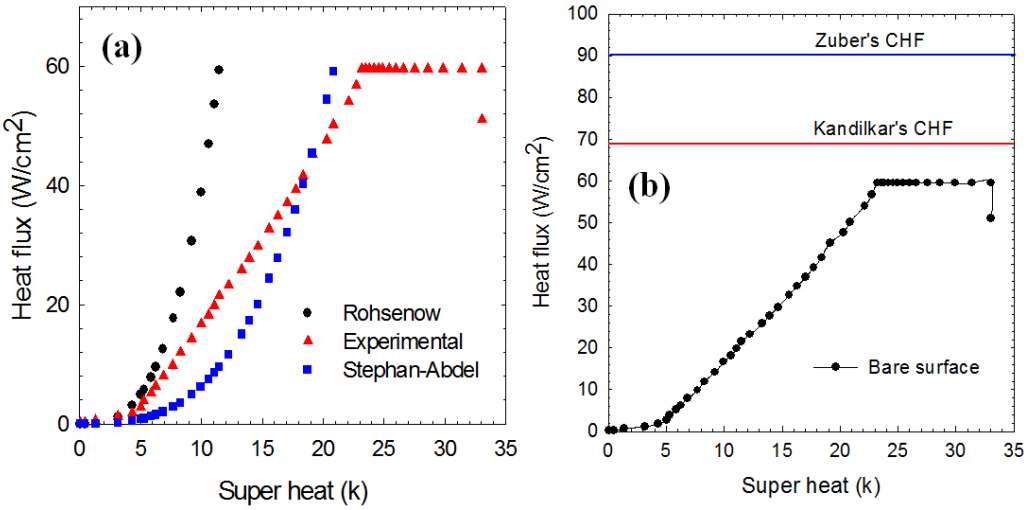

Figure 6.7. Comparisons of the experimental boiling results with empirical correlations.

Figure 6.8 exhibits the boiling curves of each boiling surface along with corresponding HTC plot as a function of heat flux. HTC values were calculated by Newton's law of cooling.

$$h = \frac{q''}{\Delta T_{heater}}$$

The bare stainless steel (304) surface was also tested as a reference to compare the heat transfer performance of the nanostructured surfaces with the bare surface.

For the examination of the nucleate boiling heat transfer regime, low heat flux (<30 W/cm^2) regime was highlighted in Figure 6.9.

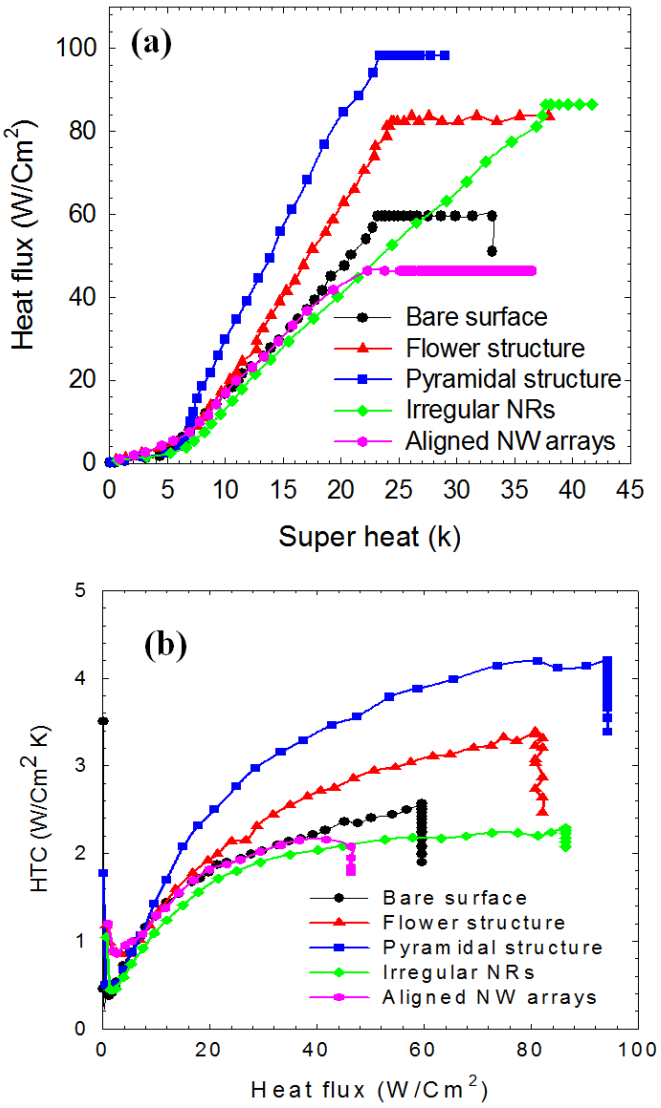

Figure 6.8. Pool boiling performances of the nanostructured boiling surfaces: (a) boiling curves and (b) HTC.

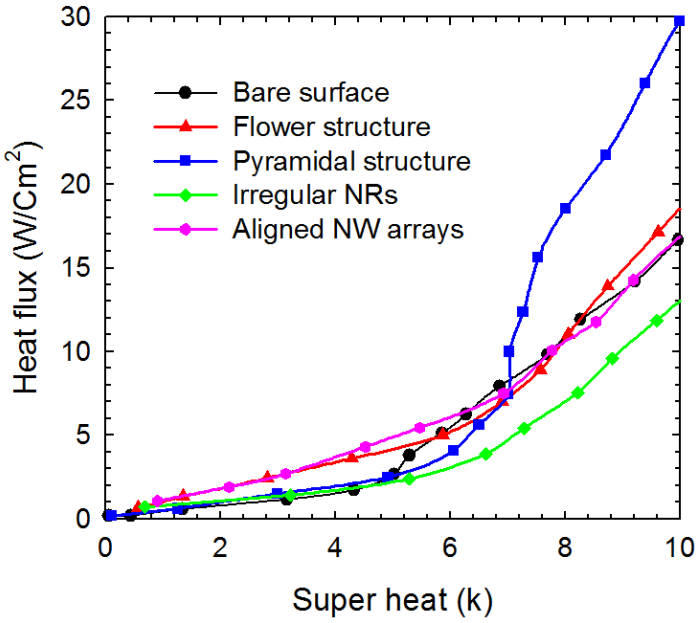

Figure 6.9. Onset of bubble nucleation.

It seems that the super heat at onset of nucleate boiling is similar irrespective of whether the boiling surface is coated with nanostructure. The shape and size of cavities play an important role in activating the bubble nucleation at lower super heat [14]. In addition, cavities should contain the trapped air or vapor to initiate the bubble nucleation at low super heat. In our nanostructured boiling surfaces, however, nano-scaled cavities created by the irregular nanostructure are too small to sustain the bubble nucleation at lower super heat. It has been known that nano-scaled cavities are not stable in nucleating bubbles due to their small cavity mouth [15]. Furthermore, the bare surface with the average roughness of 0.32 μm may have micro-scaled activated cavities which are not evitable in processing the surface.

CHF values of the nanostructured surface generally increased as compared to one of the bare surface except for the aligned NW arrays. The general tendency

of the boiling heat transfer phenomena can be well explained in terms of wettability. The wettability, the ability of the working fluid to wet the boiling surface, is a major parameter in evaluating the boiling heat transfer performance. The wettability can be represented by the contact angle measurement. The approaches to measure the contact angle are varied including a static contact angle measurement and dynamic contact angle measurement. The wettability of the nanostructured surfaces can be interpreted by two different states: Wenzel or Cassie-Baxter state [16, 17]. The Wenzel state describes the case when the drop wets the groove on the surface completely (Figure 6.10a) and is formulated as

$$\cos\theta_w = r\cos\theta_1$$

where θ_w, r, and θ_1 denotes the apparent contact angle, the ratio of the total rough surface area to the projected surface area, and contact angle of the fluid on the plain surface respectively. The value of r is always larger than one in rough structure. Thus if the contact angle of nanostructured surfaces decreased with the coating of nanostructure, the nanostructured surface is represented by the Wenzel's state. For the Cassie-Baxter state, on the other hand, the drop is sitting on the peak of the rough surface as exhibited in Figure 6.10b. The state is formulated as

$$\cos\theta_{CB} = 1 - \phi_s\,(\cos\theta_1 - 1)$$

where θ_{CB}, ϕ_s, and θ_1 denotes the apparent contact angle, the ratio of the total rough surface area to the projected surface area, and contact angle of the fluid on the plain surface respectively. In this state, the boiling surface becomes more hydrophobic after the nanostructure coating. These two states demonstrate the importance of surface modification in controlling the wettabilty. The nanostructured boiling surfaces fabricated by the continuous flow microreactor

system follow the Wenzel's state except for the irregular NRs which were prepared by the hydrothermal reaction. Recently the role of wettabiliy in affecting the nucleate boiling heat transfer was thoroughly investigated [18]. Phan et al. prepared boiling surfaces having the wide static contact angle range from 22 ° to 112 ° by using a variety of coating techniques while maintaining the same magnitude of surface roughness. Employing the visualization apparatus to examine the bubble dynamic during the nucleate boiling, they developed a new mechanism of bubble formation which is based on the dynamic contact angle approach.

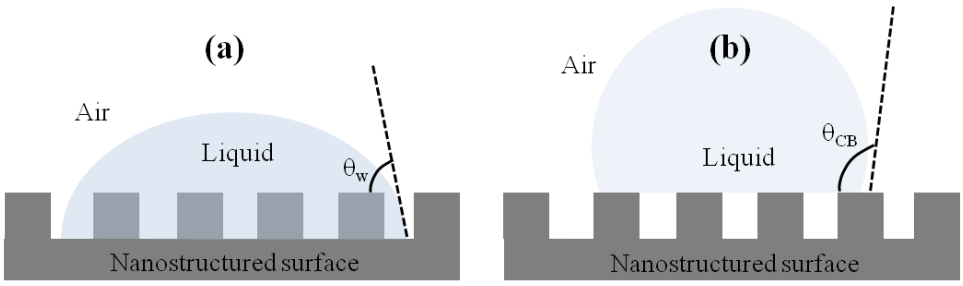

Figure 6.10. Wettability state of liquid drop: (a) Wenzel's state and (b) Cassie-Baxter state.

Scheme of the bubble dynamic is presented in Figure 6.11 and 6.12. In hydrophilic surface ($\theta < 90°$), at the onset of nucleate bubble, a convex vapor shape is generated, and the contact angle is the equilibrium angle at saturated fluid temperature (Figure 6.11a). As more heat is supplied to the boiling surface, bubble grows by continuous evaporation (Figure 6.11b). The liquid microlayer underneath the bubble also begins to evaporate, making the triple contact line expand. In this condition, the contact angle is referred as the receding contact angle (Figure 6.11c). Due to the high buoyancy force of the fully grown bubble, the bubble stretch

toward the vertical direction, and as the buoyancy force is dominant, the bubble detach from the cavity (Figure 6.11d). Bubble growing on hydrophobic surface (θ > 90°) was also reported. A concave shaped embryo is created from the cavity on the hydrophobic surface at lower heat flux. Likewise the contact angle is determined by the equilibrium angle at saturated temperature (Figure 6.12a). The concave shaped embryo is transformed into a convex shaped vapor as it appears from the cavity mouth (Figure 6.12b). As bubble grows by the continuous evaporation the contact angle decreases to the receding contact angle. In the hydrophobic surface, the receding contact angle is larger than 90 °. Due to the high surface tension, the bubble cannot detach from the cavity (Figure 6.12c). The bubble moves toward in lateral direction, coalescences to neighboring bubble, and form the vapor blanket. Due to the low thermal conductivity of the vapor blanket, the CHF state quickly reached in low heat flux (Figure 6.12d).

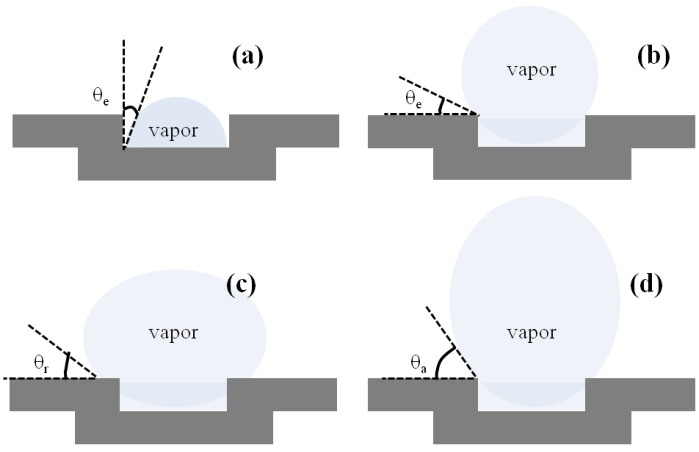

Figure 6.11. Bubble growing on hydrophilic surface.

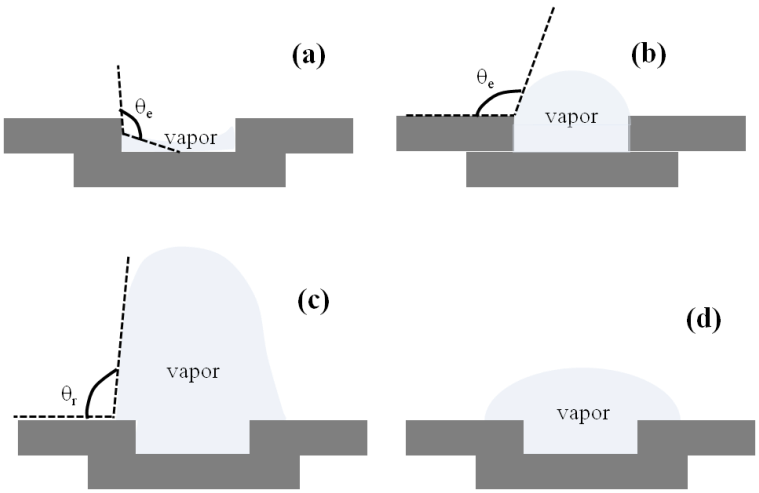

Figure 6.12. Bubble growing on hydrophobic surface.

In hydrophilic surface, bubble grows with a larger diameter, and frequency of the bubble departure become lower. High bubble departure frequency is favorable to the effective heat dissipation of the boiling surface. However, during the bubble growth on hydrophilic surface, a liquid microlayer underneath the bubble is expanded, and heat from the boiling surface is dissipated through the thin microlayer (Figure 6.11). In the nanostructured boiling surface, HTC values of the boiling surface with low static contact angle (flower structure and pyramidal structure) significantly enhanced as compared to the bare surface. We conjecture that the HTC enhancement is attributed to the bubble growth with larger diameter and continuous bubble departure even with low departure frequency.

The surface wettability also plays an important role in improving CHF values of nanostructured surfaces [7, 11]. As the contact angle decreased by the nanostructre coating on the bare surface, the CHF values increased as shown in the cases of the flower structure and pyramidal structure (Table 6.2). The pyramidal structure is more wettable than the flower structure, which contributes the

pyramidal structure to achieve the highest CHF value. These hydrophilic surfaces can be refreshed by prompt inflow of the liquid into the cavity after the bubble departure, interfering with the formation of the vapor blanket and delaying the CHF. In addition, the nanostructure coating may increase the number of activated bubble nucleation sites, making the boiling surface more efficient.

Irregular NRs was found to follow the Cassie-Baxter state where the contact angle increased with the nanostructure coating. The poor wettability led the nucleate boiling heat transfer to be less efficient, revealing the low HTC value.

Aligned NW arrays having contact angle of 53 ° showed the similar nucleate boiling heat transfer to the bare surface. However, the CHF reached at lower heat flux than the bare surface. This may be related to the aging of nanostructure. The aging of the flower structure was observed after repeating the boiling heat transfer performance (Figure 6.13). Flower structure was eliminated completely after reaching CHF, which deteriorated the boiling performance [13].

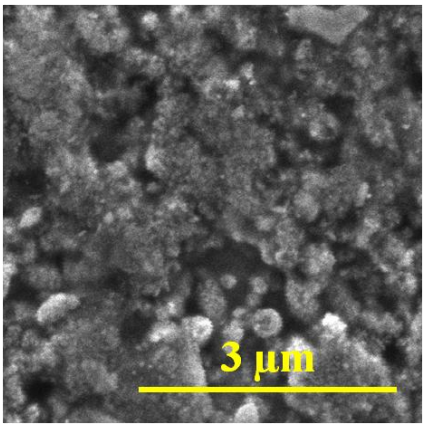

Figure 6.13. SEM image of the flower structure after boiling performance.

Although the surface wettability is a major parameter in characterizing the boiling heat transfer performance, it cannot solve some questionable results obtained during the boiling performance of the nanostructured surfaces: (1) irregular NRs improved the CHF value although it has the hydrophobic nature. (2) Although the aging effect was proposed for the CHF attenuation, this reasoning is still doubtful. For the indisputable understanding of the boiling heat transfer using the nanostructured boiling surfaces, the visualization apparatus would be required to examine the bubble dynamic including bubble departure frequency and the progress of the bubble growth.

6.3.3. Promising nanostructured boiling surfaces

The continuous flow microreactor system is capable of producing other colloidal metal oxide nanocrystals and nanostructured surfaces as well. In this section, NiO and SnO nanostructured surfaces are introduced as the promising nanostructured boiling surfaces. The principle of synthesizing colloidal SnO nanocrystals is presumed to be same as one for the colloidal ZnO nanocrystals. The speciation diagram of Sn precursors as a function of solution pH was constructed by using the Visual Minteq software (Figure 6.14). PZC of the tin oxide was reported to be around pH=7.3. In order to avoid the agglomeration of SnO nanocrystals, the solution acidity was maintained to be around pH=5 where $Sn(OH)_2$ (aq) is the dominant precursors for the nucleation and growth of SnO nanocrystals according to the speciation diagram.

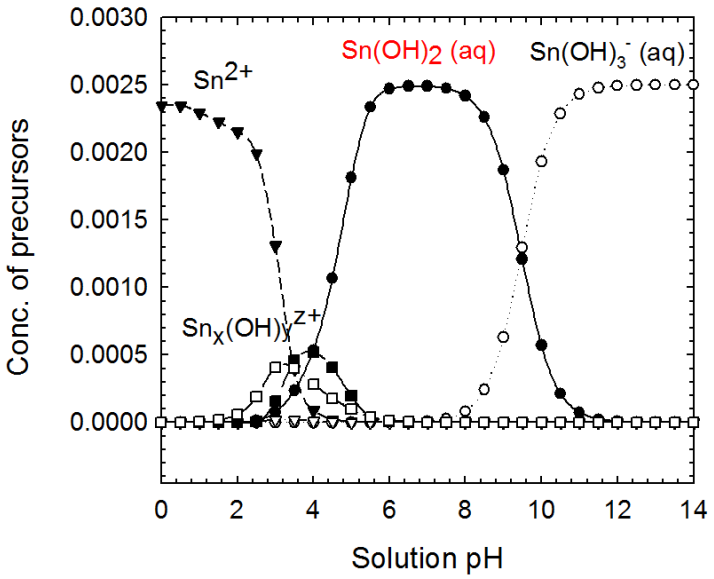

Figure 6.14. Speciation diagram of Sn precursors as a function of solution pH.

For the fabrication of SnO nanostructured surface, ZnO seed layer was necessary. Colloidal SnO nanocrystals can be deposited onto the ZnO seed layer that is etched off during the deposition process. Morphology of the SnO nanostructured surface deposited on the stainless steel substrate is shown in Figure 6.15. Approximate 1μm octahedral structure was formed with high density on the substrate. The size and shape of the structure is uniform while growth orientation is random. This structure is promising as the boiling surface in terms of high structure density and irregularity. The characterization of surface wettability and roughness will be conducted in the future to better illuminate the potential of the surface for the boiling heat transfer performance.

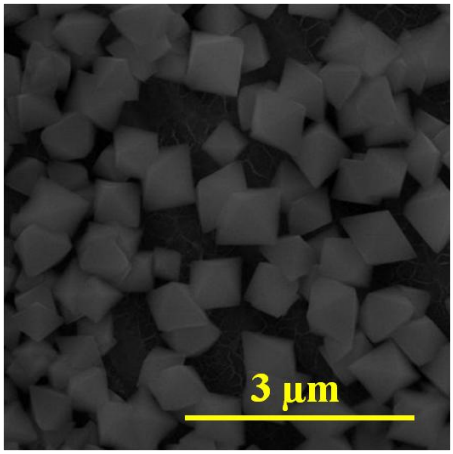

Figure 6.15. SEM image of SnO nanostructured surface.

Porous NiO nanostructured was also prepared by the continuous flow microreactor system. Stream A containing solution of 0.01M nickel sulfate hexahydrate and a solution of 0.0025M potassium persulfate were mixed with stream B, ammonium hydroxide, in the micromixer. The mixture then flew toward the helical reactor in which presumably NiO nanocrystals formed. The reaction took place at room temperature with a residence time of 7.5 sec and immediately was spin-coated onto a 100°C stainless steel substrate that was spinning at 1500 rpm. The deposition time was 45 seconds for optimal thickness, but could be varied to increase or decrease film thickness. Higher reaction temperature and higher solution concentrations resulted in a higher rate of nanocrystal precipitation or agglomeration. Decreased flow rate (increased residence time) also allowed for more nanocrystal growth and agglomeration. Thus the concentration of precursors associated with the hydrolysis reaction rate is important key to control the uniform film formation and thickness of the film. Figure 6.16 shows the porous NiO film having various nanopore size. The pore density is very high, and if the nanopores

can serve as the activated bubble nucleation sites, we may expect the promising boiling surface.

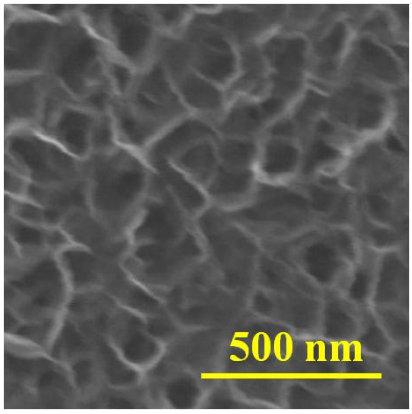

Figure 6.16. SEM image of porous NiO film.

6.4. Conclusions

ZnO nanostructured surfaces with various morphologies were prepared by using the continuous flow microreactor system. Changing the flow rate of the solution allowed for the fabrication of various morphologies of the nanostructured surfaces such as flower, pyramidal, aligned NW arrays. Irregular ZnO NRs were also synthesized by the hydrothermal reaction. These nanostructured surfaces were applied for two-phase pool boiling experiments. Hydrophilic nature of the nanostructured surface enhanced the nucleate boiling heat transfer and CHF as compared to the bare surface. More characterization including visualization of bubble dynamic will help better understand the bubble growth and departure mechanism, which is now a key question and required to elucidate the enhancement of boiling heat transfer performance. Octahedral SnO nanostructure and porous NiO film were prepared by the continuous flow microreactor system

and considered to be potential candidates as the boiling surfaces. The multi-scale nano and micro geometry and high density of the nanostructure are expected to improve the boiling heat transfer performance.

6.5. References

[1] Y.-W. Lu and S. G. Kandlikar, Heat Transfer Engineering, 32, 827 (2011)

[2] J. A. Eastman, S. R. Phillpot, S. U. S. Choi, and P. Keblinski, Annual Review of Materials Research, 34, 219 (2004)

[3] V. I. Terekhov, S. V. Kalinina, and V. V. Lemanov, Thermophysics, and Aeromechanics, 17, 1 (2010)

[4] H. Kim, Nanoscale Research Letters, 6, 415 (2011)

[5] Z. Yao, Y. W. Lu, and S. G. Kandlikar, International Journal of Thermal Sciences, 50, 2084 (2011)

[6] C. Y. Lee, M. M. H. Bhuiya, and K. J. Kim, International Journal of Heat and Mass Transfer, 53, 4274 (2010)

[7] S. Kim, H. D. Kim, H. Kim, H. S. Ahn, H. Jo, J. Kim, and M. H. Kim, Experimental Thermal and Fluid Science, 34, 487 (2010)

[8] S. Ujereh, T. Fisher, and I. Mudawar, International Journal of Heat and Mass Transfer, 50, 4023 (2007)

[9] M. S. El-Genk and A. F. Ali, International Journal of Multiphase Flow, 36, 780 (2010)

[10] N. A. Patankar, Langmuir, 26, 8941 (2010)

[11] C. H. Li, T. Li, P. Hodgins, C. N. Hunter, A. A. Voevodin, J. G. Jones, and G. P. Peterson, International Journal of Heat and Mass Transfer, 54, 3146 (2011)

[12] R. Chen, M.-C. Lu, V. Srinivasan, Z. Wang, H. H. Cho, and A. Majumdar, Nano Letters, 9, 548 (2009)

[13] T. J. Hendricks, S. Krishnan, C. Choi, C.-H. Chang, and B. Paul, International Journal of Heat and Mass Transfer, 53, 3357 (2010)

[14] V. P. Carey, Liquid-Vapor Phase-Change Phenomena, Taylor & Francis, London, 1992

[15] L. S. Tong, Y. S. Tang, Boiling Heat Transfer and Two Phase Flow, Taylor & Francis, London 1997

[16] R. N. Wenzel, Industrial and Engineering Chemistry, 988 (1936)

[17] A. B. D. Cassie and S. Baxter, Trans. Faraday Soc., 40, 546 (1944)

[18] H. T. Phan, N. Caney, P. Marty, S. Colasson, and J. Gavillet, Internationl Journal of Heat and Mass Transfer, 52, 5459 (2009)

Chapter 7. Conclusions and Future Directions

7.1. Conclusions

Colloidal ZnO nanocrystals and assembly were synthesized by using the continuous flow microreactor system. Directly depositing these colloidal nanocrsytals and assembly onto the substrate, ZnO nanostructureds surface with various morphologies were fabricated. The application of these nanostructured surfaces was focused on the two-phase pool boiling heat transfer performance. The main results of this study are summarized below.

(1) Stable colloidal ZnO nanocrsytals were synthesized by using the continuous flow microreactor system in an aqueous medium.

(3) Solution pH determined the dispersion behaviors of colloidal ZnO nanocrystals.

(2) Flow rate of the solution was a key parameter in generating the assembly and controlling the assembly structure.

(4) Using colloidal ZnO nanocrystals and assembly, ZnO nanostructured surfaces were fabricated, including the flower structure and amorphous thin film. The growth study of the flower structure was performed by changing the system parameters.

(5) Vertical ZnO NW arrays were also prepared by using the continuous flow microreactor system. Colloidal ZnO nanocrsytals, building blocks for the growth of ZnO NW, were directly deposited onto the amorphous ZnO thin film which led to the vertical formation of ZnO NW arrays.

(6) The aspect ratio of nanowire can be controlled by simply adjusting the process parameters such as deposition period and thickness of the seed layer.

(7) ZnO flower structure was coated onto the microwick structure and used for enhancing the capillary force of liquid. The coated microwick structure improved the capillary force when both water and EtOH were used as working liquids.

(8) The experimental wicking rise was compared with some analytical models to find out the most influential force on the capillary rise of the coated wick structure.

(9) Two-phase boiling heat transfer was performed using the ZnO nanostructured surfaces prepared by the continuous flow microreactor system. The nanostructured surface was characterized in terms of surface wettability and surface roughness.

(10) Pool boiling curves corresponding to each nanostructured surfaces were obtained. The nanostructured surfaces resulted in the enhanced boiling heat transfer performance in terms of high HTC and CHF as well.

(11) Porous NiO film and octahedral SnO structure, prepared by the continuous flow microreactor system, were proposed as potential boiling surfaces for the boiling heat transfer experiment.

7.2. Future Directions

7.2.1. Continuous flow microreactor system

The continuous flow microreactor system was demonstrated to produce the monodispersed colloidal metal oxide nanocrystals in an aqueous medium. The system can be categorized into three zones including (1) precursor mixing zone, (2) nanocrystal growth zone, and (3) nanocrystal deposition zone. In this section, the methodological suggestions are made to develop the system, which will help

expand the applications of the system for industrial or commercial level. In the mixing zone, only two streams containing precursors have been mixed inside the micro-T- mixier. In order to develop the system for producing the ternary or composite nanocrystals, the micro-T- mixer should be replaced to accommodate as many precursor streams as needed. The selection of the micro-mixer is very important because, for instance, monodispersed nanocrystals can only be achieved by the homogeneous hydrolysis reaction of metal ions. The helical reactor zone has been employed to exert the Dean vortices to nanocrystals, resulting in various assembly structures. Adjusting geometry of the reactor is deserved to be attempted since it may give rise to different hydrodynamics, affecting the behaviors of nanocrystals. It was found that the angular momentum significantly affect the structure of nanostructure coating. Deposition temperature was also revealed to affect the size and density of nanostructure. However, in the current system, the method to measure the precise deposition temperature is not installed. Knowing the temperature variation during the deposition process will help better understand the growth mechanism of nanostructured surfaces. In addition, the empirical study of the nanostructure coating is need to incorporate with the computational study, elucidating the effect of angular momentum and deposition temperature on the formation of nanostructured surface.

7.2.2. Two-phase boiling heat exchanger

Based on the boiling experimental results of the nanostructured surfaces and published outcome, an engineering boiling surface is suggested. This boiling surface is designed to optimize all the characteristics known to enhance the boiling

heat transfer performance. The surface characteristics favorable in enhancing the boiling performance are summarized below.

(1) High density of the bubble nucleation sites: nanocoating creates nano and micro sized pores. Defects of nanostructure can give rise to micro sized pores which serve as the activated bubble nucleation sites.

(2) Hydrophilic surface: hydrophilic surface can delay the formation of vapor blanket and dry pot of the boiling surface by continuously supplying the fresh liquid into the cavity.

(3) Stable cavity: In order to keep the bubble nucleated and growing, the shape and size of the cavity is very important. Trapped air or vapor is also required to initiate bubble embryo at low heat flux. Reentrant cavity was reported to ensure the trapped air or vapor inside the cavity.

(4) Liquid spreadability: this parameter was recently introduced as one of critical parameters in enhancing the boiling heat transfer performance. This parameter somewhat differs from the wettability in that the liquid spreads in the lateral direction while wettability presents the wetting of the cavity.

Considering all of parameters described above, we can design the optimal boiling surface. Micro-sized pores formed by the nanocoating can be manufactured by using the photolithography technique. This technique enables to control the spacing between nanostructures, which significantly affects the CHF phenomena. In order to hold the trapped air inside the cavity, the complete wetting of the cavity should be avoid. However, hydrophobic surface result in deteriorated boiling heat transfer due to the formation of vapor blanket even at low heat flux. Therefore, heterogeneous boiling surface possessing both hydrophilic and hydrophobic

characteristics is strongly recommended to not only reduce the super heat at onset of nucleate bubble but improve the CHF value. Lastly for the improvement of liquid spreadability, nanostructures exhibiting high capillary force can be applied, including one dimensional nanowire arrays. Combining all these favorable parameters to the enhanced boiling heat transfer, one example of the optimal boiling surfaces is illustrated in Figure 7.1.

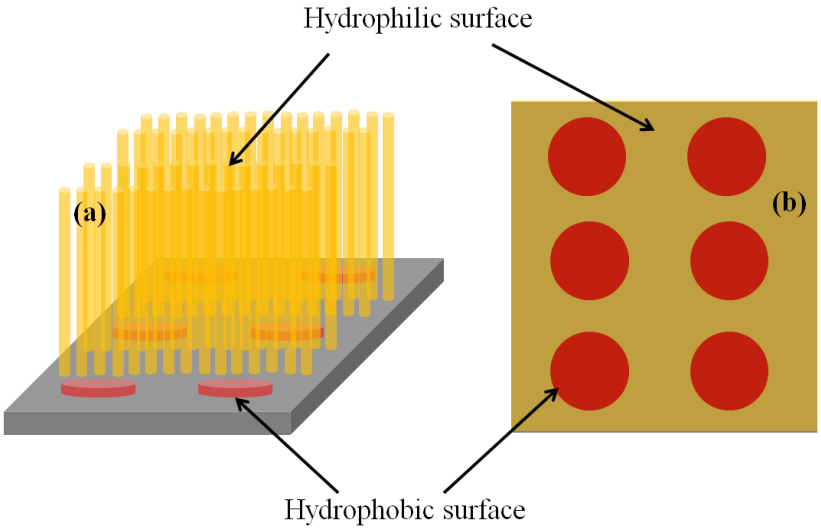

Figure 7.1. Scheme of the proposed optimal boiling surface: (a) side view and (b) plain view.